# Use Deuterium Solid State NMR Simulations to Study Dynamics of Peptides Adsorbed onto Inorganic Surfaces

Kun Li

A dissertation
Submitted in partial fulfillment of the
Requirements for the degree of

Doctor of Philosophy

University of Washington
2012

Reading Committee:
Gary Drobny, Chair
David Cobden
Xiaosong Li

Program Authorized to Offer Degree:
Physics

University of Washington

Abstract

# Use Deuterium Solid State NMR Simulations to Study Dynamics of Peptides Adsorbed onto Inorganic Surfaces

Kun Li

Chair of the Supervisory Committee:
Professor Gary Drobny
Department of Chemistry

This work is directed towards building an understanding of the dynamics of protein/peptide adsorbed on inorganic surfaces. Deuterium solid state NMR(SSNMR) is a very special tool for probing molecule dynamics in solid state. The probing of dynamic information is realized by simulation of the Deuterium line shape and relaxation data in the experiment. Two different SSNMR experiments are used: the quadrupole echo experiment and MAS experiment. The simulation of quadrupole echo experiment adopted the public simulation program MXET1, while the simulation of MAS experiment adopted the house made program KLDMAS. The theory and part of the KLDMAS code are described in detail in Chapter II. Then the codes were used to simulate the dynamics of peptide side chain on different inorganic surfaces.

In this thesis, two peptides adsorbed on surfaces were studied, LKα14 and SN15. LKα14 is a 14 amino acid peptide with a periodic sequence of leucine and lysine residues consistent with an amphipathic α-helix. By using both quadrupole echo and MAS experiments, together with SFG method, it is found that the dynamics of the leucine side chains in LKα14 is quantifiable, and is strongly upon the orientation of the polymer on the surface, which in turn depends on whether the LKα14 peptide adsorbs onto a polar or non-polar surface.

Another peptide-surface system is SN-15 peptide binding on hydroxyapatite surface. The dynamics of phenylalanine side chains in SN-15 are studied using deuterium MAS line shape and relaxation. The spectra are interpreted using a model in which the phenylalanine side chain exchanges between rotameric states. Although rotameric exchange motions of phenylalanine have been observed for small peptides in solutions, this is the first time such exchange has been observed in solid state samples. Moreover, when the dynamics of two different phenylalanine side chains within the SN-15 peptide are compared, both rotameric populations and rotameric angles differ as functions of orientation and surface proximity. These results show that the side chain dynamics of surface-adsorbed peptides are very different with the same peptides in solid, but actually resemble to the dynamics of side chains in solution state.

# TABLE OF CONTENTS

# List of Figures

Figure Number Page

# List of Tables

Table Number Page

# Acknowledgements

First of all, I want to show my best respect to my advisor, Prof. Gary Drobny, for so many years' guiding and encouragement. His great insight on my research directions and rigorous attitude toward my research details have and will continue to benefit me in my life. And I want to thank Prof. David Cobden and Prof. Xiaosong Li for the kindness and help as my reading committee. I also feel lucky to have been directed or worked with my past or current group members: Greg Olsen, Prashant Emani, Jason Ash, Nicholas Breen, Wei Huang, Michael Groves, Paul Miller, Zara Shajani, Moise Ndao, Dorothy Echodu, Kari Pederson, Ariel Zane, Adrienne Roehrich and Matt Powers.

And I want to thank my whole family, especially my wife, Xiaoli li, for so many supports and inspirations during all these years. Also I want to thank my dearest son, Wenhan Li, for giving his dad so many loves. And I want to thank my best parents in the world, for giving me life, for bringing me up in a wonderful atmosphere and for always supporting me in all my life.

# Chapter I

# Basics of Deuterium Solid State NMR

Ever since the birth of nuclear magnetic resonance, NMR has become an incredible tool in diverse fields, e.x, physics, chemistry, biology, engineering, medical, etc[1]. Among all these uses, deuterium solid state NMR(SSNMR) is a very special tool for probing molecule dynamics in solid state. To have a clear picture of deuterium SSNMR and its application to molecular dynamics, we need to review the basic background of NMR and quadrupole spin manipulations.

## 1.1 Nuclear Spin Interactions for Deuterium SSNMR

### 1.1.1 Introduction

One of the reasons for using nuclear magnetic resonance is its ability to give information about processes at the atomic level[2]. Nuclear magnetism and nuclear spin are very important properties of materials, yet they are so weak that they have little consequence for atomic or molecular structure. By probing nuclear magnetism and nuclear spin properties, NMR can tell the structures of objects without disturbing them, so it has been widely used as a wonderful noninvasive tool in many fields. In these fields, different NMR probes are used to adapt to the state of the matter, either solution state or solid state, and different isotopes are used to label and investigate the areas in the matter that people are most interested in. This work is focused on protein/peptide motion on/off inorganic surfaces in the solid state, and Deuterium is the isotope that played the key role in this study.

Deuterium($^2$H) is one of two stable isotopes of hydrogen. It has quadrupole moment with spin number I=1. The relatively small electric quadrupole moment of $^2$H gives rise to quadrupole coupling interaction in the range of 140-220kHz[3], much smaller than the Zeeman interaction. This width in the spectrum makes this nucleus relatively easy to deal with. Also the line shape and relaxation of $^2$H patterns are very sensitive to molecular motions, so it has been extensively used in motional studies.

### 1.1.2 Zeeman Interaction

The electric and magnetic fields exerted on a nuclear spin may originate from the external source, e.x, Zeeman interaction is between the external static field and the spin; or it may originate from the sample itself, which are internal spin interactions, like chemical shift interaction, dipolar coupling interaction, quadrupolar coupling interaction, etc. Depending on the species of the spin, and the type of the experiment, the counting interactions are also different. In motional studies by using Deuterium SSNMR, the most important interactions are Zeeman interaction and quadrupole coupling interaction, so in this work I only briefly introduce these two interactions.

The Hamiltonian for Zeeman interaction for an isolated spin in a static field is

$$H_z = -\vec{\mu} \cdot \overrightarrow{B_0} = -\hbar I_z \gamma B_0 = -\hbar I_z \omega_0 \tag{1.1}$$

The main effect of this Hamiltonian will be making the spin rotate at Zeeman frequency $\omega_0$. Here, $\vec{\mu}$ is the magnetic moment of the nuclei, $\overrightarrow{B_0}$ is the external static magnetic field. The magnetic moment operator $\vec{\mu}$ can be written in terms of the nuclear spin operator I and gyromagnetic ratio $\gamma$, and the dot product gives the value in the z direction. The gyromagnetic ratio is different for different isotopes, e.x, $\gamma$ is $2.68\times 10^8$rad/second/Tesla for proton, while it is $4.11\times 10^8$rad/second/Tesla for deuterium. Usually the magnetic field strength is conveniently represented by the Zeeman frequency of proton instead of using the actual field strength in Tesla.

For Deuterium, spin number is 1, so $I_z$ can be +1, 0 or -1. If there are no other interactions, then under this Hamiltonian, the initial single energy level of deuterium will be splitted into three energy levels, as in figure 1.1(b), and the energy difference between adjacent two is

$$\Delta\mathrm{E} = -\hbar\gamma B_0 \tag{1.2}$$

Because of the minus sign, the highest energy level corresponds to the case when the spin is antiparallel to the magnetic field, and the lowest energy level corresponds to the case when the spin is parallel to the magnetic field. There are numerous spins in a sample. In equilibrium at a certain temperature, there is a Boltzmann distribution of nuclear spins over these three states, and the population $P_i$ on any energy level $i$ is given by

$$P_i = \exp\left(-\frac{E_i}{k_B T}\right) / \sum_i \exp\left(-\frac{E_i}{k_B T}\right) \tag{1.3}$$

Here $E_i$ is the energy of spin $i$, $k_B$ is Boltzmann constant, and this equation shows that if there's no disturbance, the spins at highest energy level will have smallest population.

### 1.1.3 Quadrupole Coupling Interaction

Besides Zeeman interaction, quadrupole coupling is the most important interaction for quadrupole spin that has $I > \frac{1}{2}$. This interaction is between the electric quadrupole moment and the electric field gradient. Since the electric field gradient depends on the environment of the nucleus through the chemical bonds, the quadrupole interaction also has a dependence on orientation of the chemical bonds with respect the applied field. Thus, the molecule motion can be detected indirectly by observing the change of the quadrupole coupling interaction.

For deuterium in a strong magnetic field, while the Zeeman interaction term is usually on the order of tens of MHz, the quadrupole coupling term is on the order of several hundred kHz, so the quantization direction of the nuclear spin is still along the applied field, and the quadrupole Hamiltonian can be treated by using perturbation theory. The effect of quadrupole coupling interaction is shifting all the deuterium spin energy levels, as shown in figure 1.1(c). The exact mathematical treatment of quadrupole Hamiltonian is derived in Abragam's book[4] and in slitcher's book[2] , which have used Taylor's series expansion of electrical multiple moment and Wigner-Eckart Theorem. Here we only use their conclusion of the quadrupole Hamiltonian form.

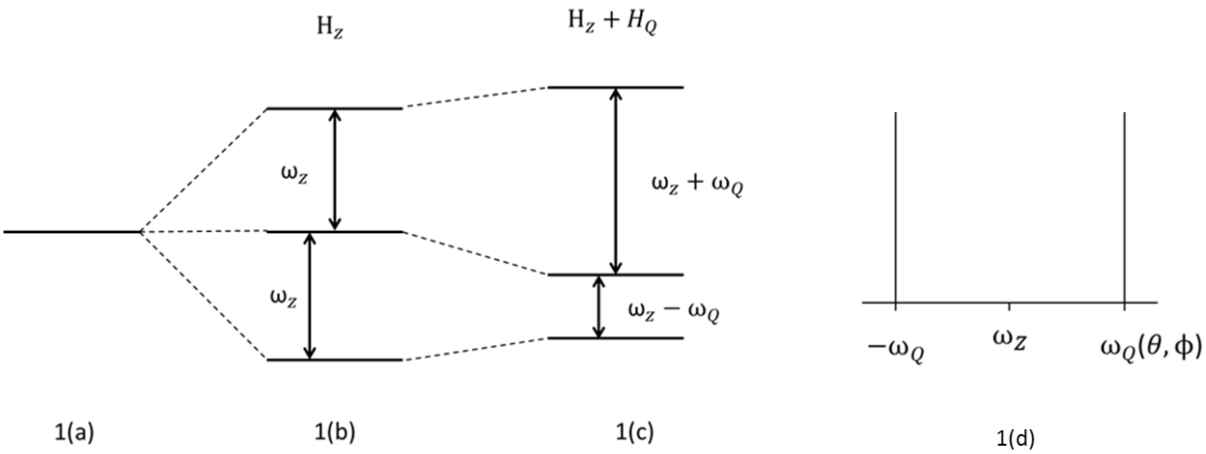

Figure1.1. Deuterium energy level split under the effect of Zeeman Interaction and Quadrupole Coupling Interaction. (a) Single Deuterium energy level without any interaction; (b) three split energy levels when only Zeeman Interaction exists, with |-1> spin energy level on the top, and the spectrum of such a transition shows a single line at $\omega_Z$; (c) when both Zeeman Interaction and Quadrupole Coupling Interaction exist, |-1> energy level is shifted by $\frac{1}{3}\omega_Q$, |0> energy level is shifted by $-\frac{2}{3}\omega_Q$, and |+1> energy level is shifted by $\frac{1}{3}\omega_Q$. (d)the spectrum of such a transition shows two lines symmetry about $\omega_Z$, and are separated by $2\omega_Q$.(Note: the ratio of $\omega_Q$and $\omega_Z$shown in the figure is not the real ratio since $\omega_Q$is much smaller than $\omega_Z$)

The basic form of the quadrupole Hamiltonian form is

$$H_Q = \frac{eQ}{2I(2I-1)\hbar}\hat{I} \cdot V \cdot \hat{I} \tag{1.4}$$

Here, $\hat{I}$ is the nuclear spin vector, e is the electron charge, Q is the nuclear quadrupole moment, and V is electric field gradient tensor. V is traceless, so it does not have isotropic component.

It is conventional to write

$$eq = V_{zz}^{PAS} \tag{1.5}$$

and

$$\eta = \frac{V_{xx}^{PAS} - V_{yy}^{PAS}}{V_{zz}^{PAS}} \tag{1.6}$$

η is asymmetry parameter, for deuterium, this is usually a number less than 0.1. PAS means Principal Axis Frame, or a frame in which the interaction tensor V is diagonal. In molecules, this

PAS frame is usually chosen as fixed on C-D or N-D bond, and the z direction is along the bond direction. Thus the basic form can be rewritten as:

$$H_Q = \frac{e^2qQ}{4I(2I-1)\hbar}[3\hat{I}^2{}_{Z,PAS} - \hat{I}^2 + \frac{1}{2}\eta(\hat{I}^2{}_{X,PAS} - \hat{I}^2{}_{Y,PAS})] \tag{1.7}$$

The constant $\frac{e^2qQ}{\hbar}$ is called quadrupole coupling constant, and is usually written as QCC.

Equation (1.7) is written in PAS frame. However, in NMR experiment, the quadrupole Hamiltonian needs to be expressed in laboratory frame(LAB). The transformation of spin vector from PAS to LAB is

$$\hat{I} = R(\theta, \phi)\hat{I}_{PAS} \tag{1.8}$$

where $R(\theta, \phi)$ is angular rotation matrix which is shown in Appendix. $\theta$ and $\phi$ are spherical polar angles describing the orientation of z axis of LAB frame in PAS frame. Put equation (1.8) into (1.7), and we can get the final form of the quadrupole Hamiltonian in the LAB frame:

$$H_Q = \frac{e^2qQ}{4I(2I-1)\hbar}\left\{\frac{1}{2}(3cos^2\theta - 1)\left(3\hat{I}_z^2 - \hat{I}^2\right) + \frac{3}{2}sin\theta cos\theta\left[\hat{I}_z\left(\hat{I}_+ + \hat{I}_-\right) + \left(\hat{I}_+ + \hat{I}_-\right)\hat{I}_z\right]\right.$$
$$\left. + \frac{3}{4}sin^2\theta\left(\hat{I}_+^2 + \hat{I}_-^2\right)\right\}$$
$$+\eta\frac{e^2qQ}{4I(2I-1)\hbar}\{\frac{1}{2}cos2\phi\left[sin^2\theta\left(3\hat{I}_z^2 - \hat{I}^2\right) + (1 + cos^2\theta)\left(\hat{I}_+^2 + \hat{I}_-^2\right)\right] + \frac{1}{2}sin\theta\left[(cos\theta cos2\phi -\right.$$
$$\left. isin2\phi)\left(\hat{I}_+\hat{I}_z + \hat{I}_z\hat{I}_+\right) + (cos\theta cos2\phi + isin2\phi)\left(\hat{I}_-\hat{I}_z + \hat{I}_z\hat{I}_-\right)\right] + \frac{i}{4}sin2\phi cos\theta(\hat{I}_+^2 - \hat{I}_-^2)\}$$
$$\tag{1.9}$$

Here $\hat{I}_+ = \hat{I}_X + i\hat{I}_Y, \hat{I}_- = \hat{I}_X - i\hat{I}_Y$.

From equation (1.9) we can see that the quadrupole Hamiltonian has both diagonal terms and off-diagonal terms, and the diagonal terms make it hard to find the eigenstates in Zeeman basis. Luckily, as stated above, the deuterium quadrupole coupling interaction is much smaller than the Zeeman interaction, so in the total Hamiltonian the latter can be safely ignored and only use the secular part. This is called secular approximation. By doing so, we can use perturbation theory and find the first order energy shift to the Zeeman levels:

$$\Delta E = \frac{e^2qQ}{4I(2I-1)}\left(3m^2 - I(I+1)\right)\frac{1}{2}[(3cos^2\theta - 1) + \eta cos2\phi sin^2\theta \qquad (1.20)$$

If we define a term quadrupole splitting:

$$\omega_Q = \frac{3e^2qQ}{4I(2I-1)}\frac{1}{2}[(3cos^2\theta - 1) + \eta cos2\phi sin^2\theta] \qquad (1.21)$$

then it's easy to see that, the energy shift of spin state |+1> or |-1> is $\frac{1}{3}\omega_Q$, and the energy shift of spin state |0> is $-\frac{2}{3}\omega_Q$ .Therefore, the energy difference between adjacent energy levels is $\omega_Z \pm \omega_Q$, and the spectrum shows two lines symmetric about $\omega_Z$, as shown in figure 1.1(d).

### 1.1.4 Powder Pattern Pake Doublet

From Equation (1.21), the quadrupole frequency is dependent on spin orientations. In a powder sample, the spin orientation is evenly distributed in all directions(figure 1.2(a)), so the powder pattern line shape is made up of infinite number of sharp lines, one from each molecular orientation. The broad pattern line shape that these lines formed is called pake doublet, which was first described by George pake[5]. The "horns" of the pake doublet correspond to the situation when the principal axis of the quadrupole coupling is perpendicular to the magnetic field(θ=90°). This situation is the most probable situation, and its intensity is the highest. The "shoulder" of the line shape corresponds to the situation when the principal axis is parallel to the magnetic field(θ=0), which is the least probable situation and its intensity is much less. Since the spectrum has both |-1> to |0> and |0> to |+1> transitions, the total line shape is then composed of two powder line shapes while one is the mirror image of another.

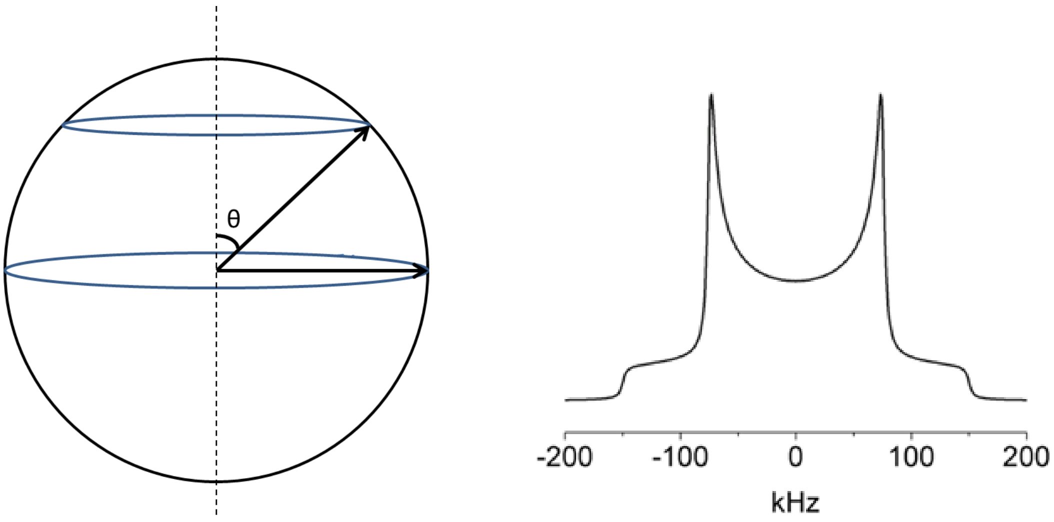

(a) (b)

Figure 1.2 Spin orientations in a powder sample and characteristic powder pattern line shape.

(a) Spin orientation in a powder sample is evenly distributed in all direction. θ=90° corresponds to the spin orientation perpendicular to the static magnetic field, θ=0 corresponds to the spin orientation parallel to the static magnetic field;

(b) Characteristic powder pattern line shape: Pake Doublet. “Horns” corresponds to θ=90°, “shoulders” corresponds to θ=0.

## 1.2 Quadrupole Hamiltonian in terms of spherical tensors and operators

The equation of (1.9) is the complete format of quadrupole Hamiltonian, however, it’s not convenient to use the spherical polar angles and Cartesian spin operators. For example, when simulating multiple frame motions, there are often several transformations needed between PAS frame and LAB frame. As shown in Figure 1.3, DMSO2 is a model compound whose motion style is well known: the deuterated methyl group is having fast rotation around S-C bond, and the two methyl groups are exchanging slowly around the symmetry axis of the molecule, so it is having multi-axis motion. To simulate this motion, we have two ways to transform: we can transform the spin vector from PAS frame to LAB frame, or we can transform the axis frame on the reverse order. In our simulation, we used the latter, i.e, first transform LAB frame to crystal frame($X_c, Y_c, Z_c$), which is the frame fixed on the main axis of the molecule; then transform crystal frame to some intermediate frame($X_i, Y_i, Z_i$), which is fixed on the S-C bond; and finally transform the intermediate frame to PAS frame, which is fixed on the C-D bond. Apparently, these transformations are not easy to deal with in the Cartesian space. The better way to treat this is to use spherical tensors and operators because they have good transformation properties and easy to manipulate.

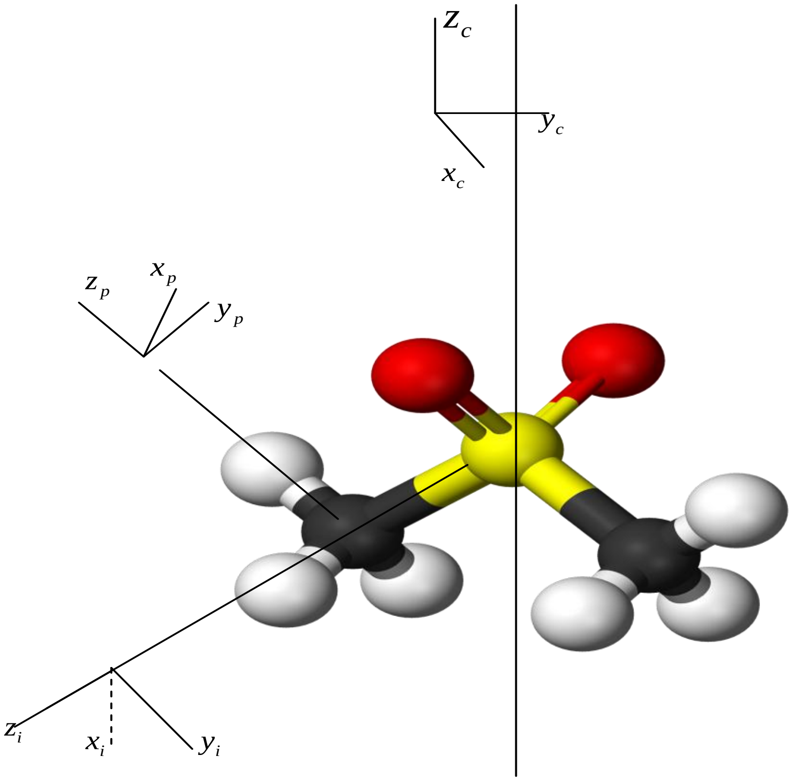

Figure 1.3 Dimethylsulfone(DMSO2) motional model shows multi-axis transformation is needed to perform the simulation. Totally there are four axis frames: LAB frame(not shown in the figure), crystal frame, intermediate frame and PAS frame.

In the PAS frame, the quadrupole Hamiltonian in terms of spherical tensor operators is

$$H_Q^{PAS} = \sum_{q=-2}^{2} (-1)^q \hat{T}_{2q}^Q \lambda_{2-q}^Q \tag{1.22}$$

Here $\hat{T}_{2q}^Q$ is spherical tensor operator of rank 2 and order q, and $\lambda_{2-q}^Q$ is spherical tensor which shows the quadrupole coupling strength and orientation. The exact form of $\hat{T}_{2q}^Q$ and $\lambda_{2-q}^Q$ is shown below:

$$\hat{T}_{20}^{Q} = \sqrt{\frac{1}{6}}(3\hat{I}_z^2 - \hat{I}^2)$$

$$\hat{T}_{2\pm1}^{Q} = \mp(\hat{I}_{\pm}\hat{I}_z + \hat{I}_z\hat{I}_{\pm})$$

$$\hat{T}_{2\pm2}^{Q} = \frac{1}{2}\hat{I}_{\pm}^2$$

$$\lambda_{20}^{Q} = \sqrt{6}\frac{e^2qQ}{4I(2I-1)}$$

$$\lambda_{2\pm1}^{Q} = 0$$

$$\lambda_{2\pm2}^{Q} = \frac{e^2qQ}{4I(2I-1)}\,\eta \tag{1.23}$$

The transformation property of spherical tensor $\lambda_{2q}^{Q}$ is

$$\lambda_{2q}^{Q} = \sum_{q'=-2}^{+2} D_{q'q}^{2}(\alpha,\beta,\gamma)\,\lambda_{2q'}^{Q} \tag{1.24}$$

here $D_{q'q}^{2}$ is element of Wigner rotation matrix of rank 2 which is shown in Appendix 2, and $\alpha,\beta,\gamma$ are Euler angles which rotate the LAB frame to the PAS frame. If there are intermediate frames, then one or more Wigner rotation matrices are needed to be inserted into equation (1.24). Examples of these transformations are shown in Chapter II.

By using the above equations and average Hamiltonian theory in the rotating frame, we can get the first order average Hamiltonian:

$$\bar{H}^{(0)} = \hat{T}_{20}^{Q}\lambda_{20}^{Q} = \sqrt{6}\frac{e^2qQ}{4I(2I-1)\hbar}\frac{1}{2}[(3cos^2\beta - 1) + \eta cos2\alpha sin^2\beta]\hat{T}_{20}^{Q} \tag{1.25}$$

Equation (1.25) is the same as equation (1.20), which proves the effectiveness of using spherical tensor operators.

## 1.3 Experimental Techniques

### 1.3.1 Quadrupole Echo Experiment

In a typical NMR experiment, we use pulse sequences to generate the transverse magnetization. Theoretically a single $\frac{\pi}{2}$ pulse can rotate the spin system from Z direction to X-Y plane; however, in real experiments, this simple pulse sequence is limited by "dead time" effects due to pulse length, recovery times, electronic system ringing, etc. In order to circumvent this dead time problems, Powles and Strange[6] have proposed a Quadrupole Echo(or Solid Echo) pulse sequence where two $\frac{\pi}{2}$ pulses separated by a time distance $\tau$ and shifted in phase by $\frac{\pi}{2}$ are applied(figure 1.4). Because of the nature of powder pattern, the transverse magnetization will evolve at different phase just after the first $\frac{\pi}{2}$ pulse, and the use of second $\frac{\pi}{2}$ pulse is to refocus the magnetization and form an echo at $t = 2\tau$. The free induction decay(FID) at time $t \geq 2\tau$ is then recorded which is identical to the FID for solid I=1 systems experiencing a time-independent coupling. The Quadrupole Echo line shape is obtained after Fourier Transform of the FID. The Quadrupole Echo Experiment is most often used technique in motional studies in Deuterium SSNMR.

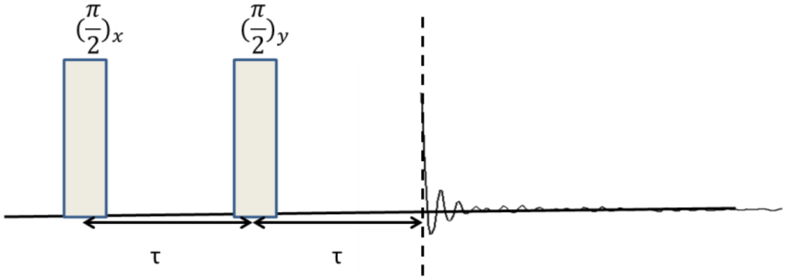

Figure 1.4 Quadrupole echo Experiment Pulse Sequence and FID

### 1.3.2 Magic Angle Spinning(MAS) Experiment

In solution NMR spectra, quadrupole coupling anisotropy as seen in powder pattern, is not observed because the fast overall tumbling of the molecule in solution averages out the orientation dependence of the frequency. As shown in equation (1.20) and (1.21), the frequency dependence is of the form $3cos^2\theta - 1$, where θ is the angle between quadrupole coupling tensor and the external magnetic field. Magic Angle Spinning(MAS) can also realize the solution result by mechanically rotating the sample around an axis inclined at an angle $\theta_m$ to the external magnetic field(Figure 1.5(a)), where $\theta_m$=54.74°. To average all the powder pattern to a single peak at frequency $\omega = \omega_Z$, as in solution NMR, the spinning rate must be fast in comparison to quadrupole coupling anisotropy, which is around 200 kHz. In the real MAS experiment, the spinning speed is much slower, which produces a set of sharp peaks called "spinning sidebands". The difference in frequency of adjacent spinning sidebands is the spinning rate. Compared to static experiment, MAS experiment greatly increases the resolution. Figure 1.5(b) shows MAS spectra of Pake Doublet at different spinning rate.

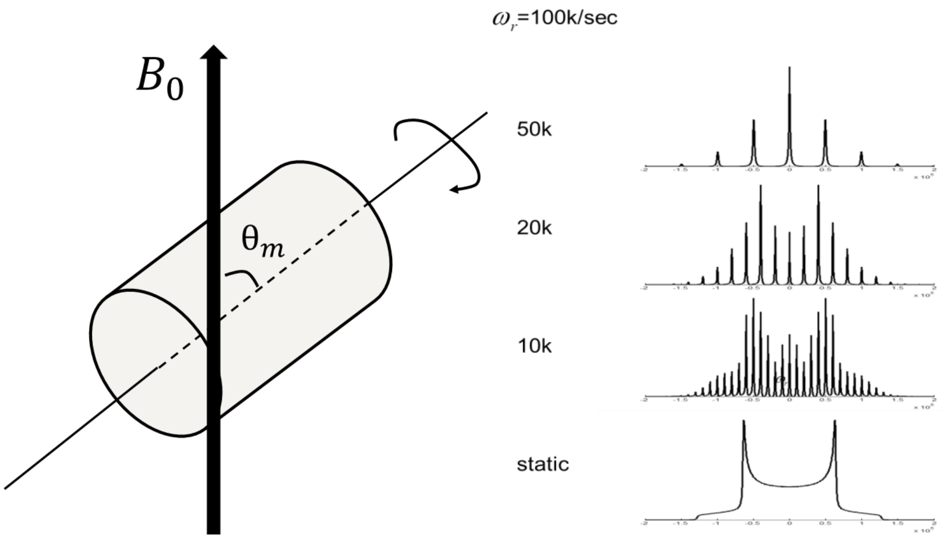

(a) (b)

Figure 1.5 Magic Angle Spinning Experiment Sketch and Pake Doublet MAS line shape

a) Magic Angle Spinning Experiment: the sample is spun rapidly around an axis tilted to $\theta_m$ relative to the external magnetic field;

b) Pake Doublet MAS line shape at different spinning rate. The bottom is powder pattern line shape, from bottom to top, the spinning rate is increased, the spinning sidebands are decreased, and the signal resolution is intensified.

### 1.3.3 Longitudinal Relaxation Experiment

Except line shape experiment, relaxation experiment is also an important technique. The simple pulse sequence of Longitudinal Relaxation experiment is shown in figure 1.6. The first π pulse inverts the spin system from +Z direction to –Z direction, then because of the environmental disturbance or motional process, the spin system goes back to equilibrium gradually. Before it goes back to equilibrium, by applying a second $\frac{\pi}{2}$ pulse, the transverse magnetization is recorded at time $t_2$to get the line shape, and different line shapes at different $t_2$ are collected. The intensity of these line shapes are usually on an exponential curve. In this way, we can track the spin system return to equilibrium, and the most general equation that describes this process is

$$\frac{dM_Z}{dt} = -\frac{(M_Z - M_0)}{T_1} \tag{1.26}$$

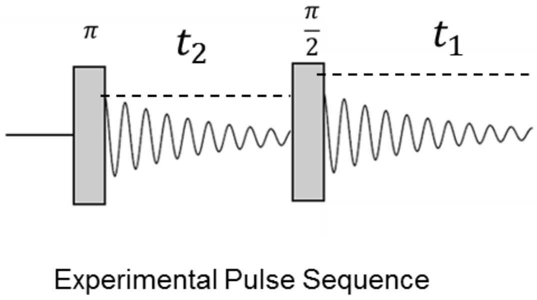

Figure 1.6 Pulse sequence of $T_1$ experiment.

The motional studies in this thesis have been done completely by using the above techniques. These studies include building motional models, developing simulation tools, and applying on biomolecular systems. The following chapters give a detailed description of these applications.

# Chapter II

# Molecular Motional Studies by using Deuterium Solid State NMR

## 2.1 Introduction

There is an increasing interest in studies of molecular motions in recent years, and various methods are employed in these studies, e.x, NMR, EPR, Molecular Dynamics, etc. Among these, Deuterium Solid State NMR is especially useful in elucidating the dynamic structures of proteins in membranes, polymers and on surfaces, and these intramolecular motions are important to their physical, chemical, and biological properties[7]. In Deuterium Solid State NMR, the amplitudes and directions of rapid motions can be deduced from the analysis of powder pattern line shapes, MAS line shapes, and relaxation studies[8-13] .

As stated in Chapter I, the quadrupole interaction anisotropy in solid state samples is caused by the molecular orientations relative to the external magnetic field, which gives out the Pake Doublet spectrum. Thus, the change of molecular orientation can create a change to the quadrupole interaction, and then the spectrum. In a liquid, fast molecular tumbling causes only the isotropic interaction to be observed; in solids, since the motions are more restricted, the effect of motions can only reduce but not to eliminate the anisotropy. The powder line shapes can be analyzed to access the details of the molecular motion. Usually, the motion rate is on the order of $10^3$ -$10^7$, which is comparable to the quadrupole interaction anisotropy. For faster motion rate($10^7$-$10^{12}$), spin-lattice relaxation experiment is used to reveal the motion details.

## 2.2 Powder Pattern Motional Line Shape and Simulations

### 2.2.1 Powder Pattern Motional Line Shape

As stated in Chapter I, the powder pattern can be regarded as being made up of an infinite number of sharp lines, one from each different molecular orientation. Any molecular motion that changes the orientation can cause the change of the powder pattern line shape. The powder pattern line shapes can be simulated by using possible models. To simulate the line shape, first we need to build the likely motional model, thereafter we need to calculate the time evolution of the transverse magnetization under the model.

Most investigations of molecular motion, including ours, have used a discrete Markov model(site jump model), which includes transitions between a finite number of chemical sites. For example, consider the molecule DMSO2 in Figure 1.3, the two $CH_3$ groups have different electronic surroundings, which give them different resonant frequencies in the external magnetic field. As explained in the figure caption, the molecule's motion is well known: besides the fast rotation of the methyl group, the molecule is planar and rigid at low temperature, but the two methyl groups can switch sites if given enough thermal energy to overcome the potential barrier between the two sites. This is the simplest 2 site jump. Here to simplify the explanation of the motional change to the spectrum, we first consider a single molecule in the external magnetic field, and only shows the line shape from transitions between |0> spin state and |-1> spin state, then the potential map of the 2 site jump and line shapes of this type are shown in figure 2.1.

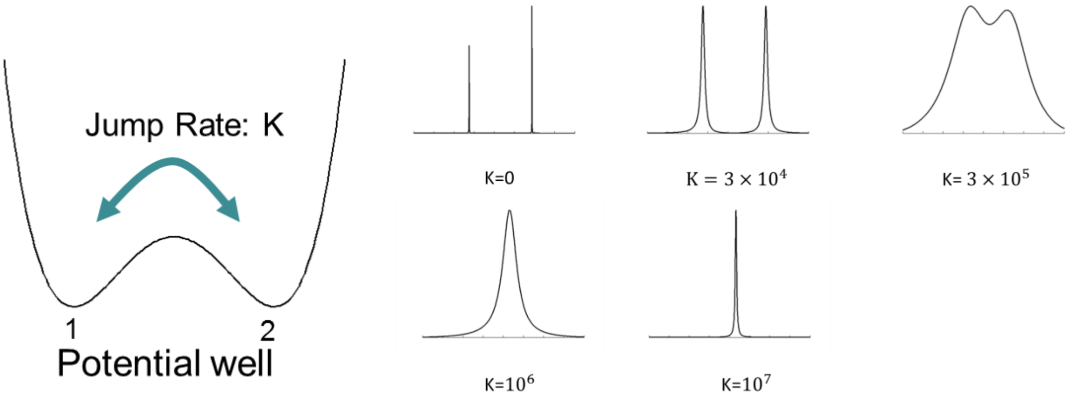

(a) (b)

Figure 2.1 Potential well for the two methyl groups in DMSO2 and line shape of a single DMSO2 molecule at different jump rate.

(a) Potential well for the two methyl groups in DMSO2. The 2 site jump model assumes that the methyl group can overcome the potential barrier by jumping between site 1 and site2, with the time taken to jump being infinitesimally small compared with the residence time in each site. The jump rate is K.

(b) Line Shape of a single DMSO2 molecule at different jump rate. At low temperature, the molecule is rigid, the two peaks represent different orientation of the two methyl groups; as rate increases, distinction between the two positions in the molecule is getting lost until an averaged single resonance is seen. Here, only transition between |0> spin state and |-1> spin state is considered.

The powder pattern line shape is thus also changed with the rate increasing, as shown in figure 2.2

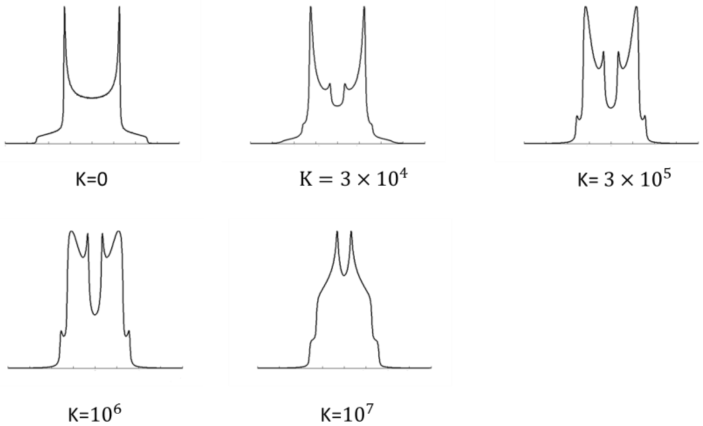

Figure 2.2 The powder pattern line shape of DMSO2 at different jump rate.

### 2.2.2 Quadrupole Echo Line Shape Simulations by using MXET1

2 site jump model in the above example is the simplest motional model to describe the molecular dynamics. In most cases, more complex motional models are needed. The complexity

includes multi frames, complex geometries, unequal site populations, appropriate quadrupole coupling amplitude, composite rates, etc. All these factors can greatly change the powder pattern line shape. The experimental conditions, like pulse width, distance between two $\frac{\pi}{2}$ pulses, and appropriate quadrupole echo selection are also minor factors. These are all variables that can be changed in the simulation software developed by Vold group, MXET1[14]. Here we describe briefly the theoretical approach used by MXET1. Simulation of the static $^2$H quadrupolar line shape is accomplished by Fourier transformation of the calculated response of a system of deuterium spins to a $\frac{\pi}{2}$ pulse. Calculation of the spin system response, in turn, requires integration of the Liouville equation:

$$\frac{dM_{\pm}}{dt} = \Gamma M_{\pm}(t) = (i\omega_{\pm} + \pi) M_{\pm}(t) \tag{2.1}$$

where M(t) is the transverse magnetization, the subscript ± refers to the m=1 to m=0 or the m=0 to m=−1 transition, π is the matrix that describes the process of exchange between n discrete conformational sites, and $\omega_{\pm}$ is a diagonal matrix with non-zero diagonal elements corresponding to the resonance frequencies of the deuterium spin at the various sites:

$$\omega_{\pm}^{j} = \pm \frac{3e^2qQ}{4\hbar}\left[\sum_{a=-2}^{+2} D_{0a}^{(2)}\left(\Omega_j^{PC}\right) D_{a0}^{(2)}\left(\Omega^{CL}\right)\right] \tag{2.2}$$

In equation (2.2) all symbols have their usual meanings[10,15,16]. $\Omega_j^{PC} = (\phi_j, \theta_j, 0)$ is the solid angle that relates the principal axis system (P) of the (axial) EFG tensor at the jth site relative to the C frame, wherein is fixed the dynamic axis. $\Omega^{CL}$ similarly relates the C frame to the laboratory frame (L). Equation 1 can be easily integrated to obtain:

$$M_{\pm}(t) = I \cdot T \cdot e^{\lambda t} \cdot T^{-1} \cdot M_{\pm}(0) \tag{2.3}$$

where I is the vector composed of ones, $\lambda$ is a diagonal matrix whose non-zero elements are the complex eigenvalues of $i\omega_{\pm} + \pi$, T is the matrix whose columns are the eigenvectors of $i\omega_{\pm} + \pi$, and $M_{\pm}(0)$ is the vector describing the initial state of the spin system. The NMR line shape is obtained as a "powder average" of the Fourier transform of equation (2.3) over all possible orientations of the C frame relative to the L frame.

A similar analysis applies to the response of the spin system to a quadrupolar echo pulse sequence. For a spin 1 system to which two 90° pulses are applied with mutual phase difference of $\pi/2$ and separated by a time $\tau_1$, the response after a time $\tau_2$ following the second 90° pulse is:

$$M_{\pm}(t) = 1 \cdot T \cdot e^{\lambda(t+\tau_2)} \cdot T^{-1} \cdot S \cdot e^{\kappa\tau_1} \cdot S^{-1} \cdot M_{\pm}(0) \tag{2.4}$$

All symbols in equation (2.4) are defined as in equation (2.3), in addition to which $\kappa$ is the matrix of eigenvalues of $-i\omega_{\pm} + \pi$ and $S$ is the corresponding matrix of eigenvectors.

The simulation by using MXET1 to find a good Markov model is a time consuming work because of the many variables. Here we need to point out that, there may be several simulation models that can fit data. So sometimes it is necessary to acquire other data type, like $T_1$, to rule out some fits. Also the Makov model has its limitations since the process assumes the motion is a hopping between very sharp and deep potential wells. If the potential well is shallow and wide, then there will be some diffusion process in each site, and the Makov model is no longer applicable.

## 2.3 Magic Angle Spinning Motional Line Shape and Simulations

### 2.3.1 Magic Angle Spinning Line Shape

Since MAS spectrum is actually orientation-averaged powder pattern line shape, existence of motion also causes the change of the MAS line shape. The DMSO2 molecule's MAS line shape at different rate is shown as following:

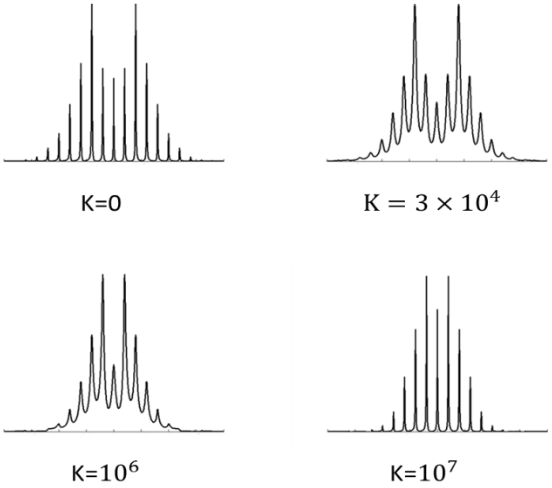
K=0

$K = 3 \times 10^4$

$K=10^6$

$K=10^7$

Figure 2.3 The MAS line shape of DMSO2 at different jump rate.

In fast motion regime(k>10^7) or in slow motion regime(k<10^4), the spinning side bands' intensity is much greater than static experiment, because the which brings much higher S/N or much less experimental time. However, in the intermediate motion regime(10^4<k<10^7), the intensity has reduced amplitude. It is well known that in the QE line shape experiment, exchange-induced dephasing can interrupt the refocusing of the second pulse[17,18], and produce an absolute intensity loss of the spectrum[14]. This effect is especially pronounced when the correlation time of the motion is on the order of the time interval between the 90 degree pulses of the QE sequence. In a $^2$H MAS experiment, reorientation-induced frequency jumps during a rotor period interfere with the formation of the echo at the end of the rotor period causing it to have lower amplitude than the echo that commenced the rotor period [19].

To better display this property, we adopt a simple 2 site jump model which assumes that the C-D bond can only switch at rate k between two sites, with their Euler angles are (0, π/3, 0) and (0, π /3, π). The MAS spinning rate is 8 kHz and 16 kHz individually. Figure 2.4a shows how the intensity of the $^2$H MAS line shape varies with the rate, Figure 2.4b shows $^2$H MAS line shapes obtained for selected jump rates. Note the low amplitude of a jump rate of $10^5$ Hz. In the case of a 8 kHz spinning rate, the attenuation is most severe for the range $k = 5 \times 10^4 - 10^6$ Hz, while in the case of 16 kHz spinning rate, the attenuation is most severe for the range $k = 10^4 - 5 \times 10^6$.

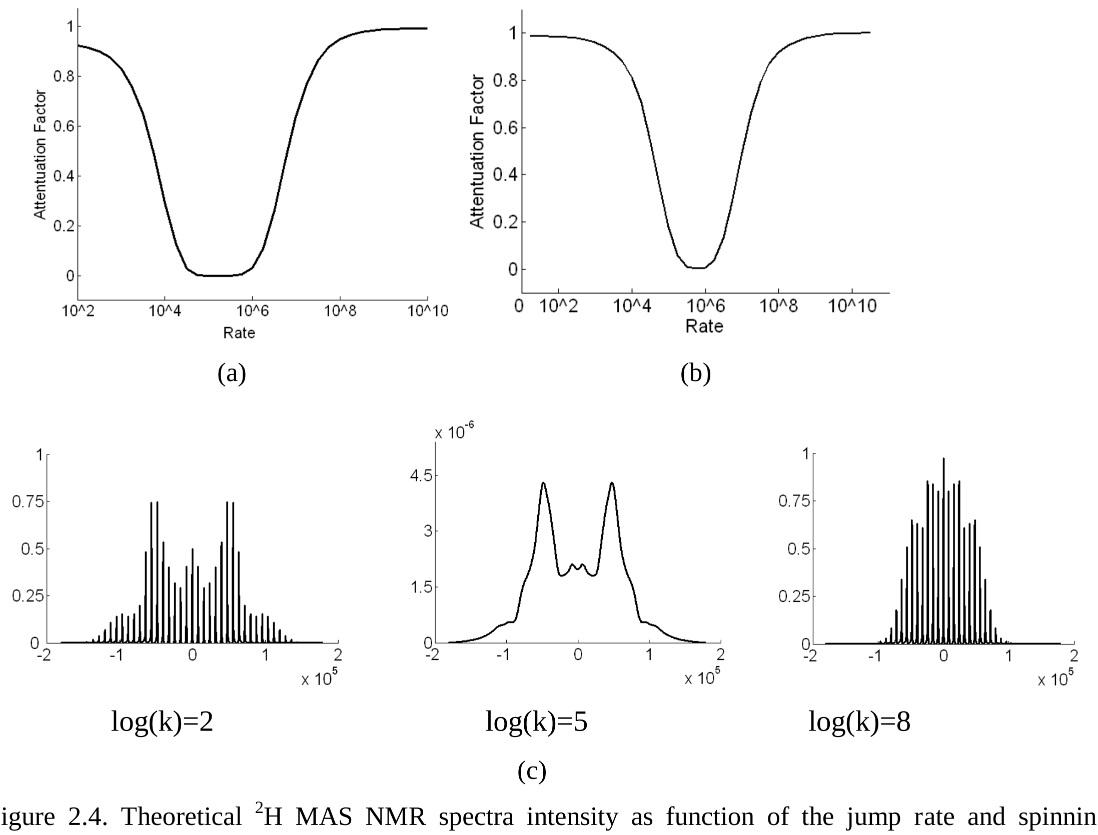

(a) (b)

log(k)=2 log(k)=5 log(k)=8

(c)

Figure 2.4. Theoretical $^2$H MAS NMR spectra intensity as function of the jump rate and spinning speed and calculated spectra at 3 specific jump rate constants.

(a) Theoretical $^2$H MAS NMR spectra intensity as function of the rate constant $k=k_{12}=k_{21}$ for a quadrupole coupling tensor whose principal axis system can assume two equally probable orientations relative to the crystallite fixed axis system. The orientations were given by $\Omega(\alpha,\beta,\gamma)=\{0,\pi/3,0\}$ and $\{0,\pi/3,\pi\}$. The calculations employed QCC=170 kHz, asymmetry parameter $\eta$=0, spin frequency $\upsilon_r$=8 kHz, and Lorentzian line broadening of 1 kHz. (b)spin frequency $\upsilon_r$=16 kHz. (c) Theoretical $^2$H MAS NMR spectra at 3 jump rate constants. The intensity of each spectrum is normalized by dividing the spectrum intensity at fast limit rate.

The MAS attenuation is not only affected by rate, but also affected by site population and geometry. Here we still use the previous example as in Figure 2.4, but assume a fixed rate at $5\times 10^6$, and that one site population p1 is changed within 0-1, and theta angle is varied from 20° to 70°, 10 degree a step. Then a plot of attenuation factor vs p1 and angle is shown below:

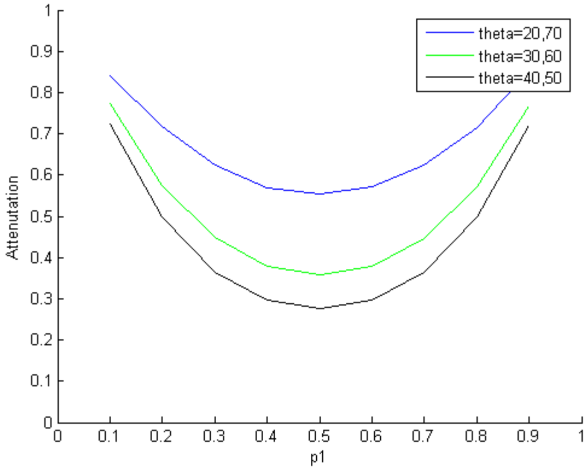

Figure 2.5 Theoretical $^2$H MAS NMR spectra intensity attenuation as function of site population and geometry at the rate constant $k=5\times 10^6$ for a quadrupole coupling tensor whose principal axis system can assume two orientations relative to the crystallite fixed axis system. The orientations were given by $\Omega(\alpha,\beta,\gamma)=\{0,\text{theta},0\}$ and $\{0,\text{theta},\pi\}$. Angle theta was varied from 20° to 70°, 10 degree a step. The calculations employed QCC=170 kHz, asymmetry parameter $\eta=0$, spin frequency $\upsilon_r=8$ kHz, and Lorentzian line broadening of 1 kHz.

From Figure 2.4, depending on the spinning frequency, the intensity of MAS signal is most severely attenuated for rates in the range $10^5$-$10^6$ Hz which is in intermediate motion regime, but the signal intensity recovers as the transition rate increases to greater than $10^6$ Hz or decreases to less than $10^5$ Hz. So within the intermediate motion regime, temperature dependent experiment is convenient to use, because the rate can be greatly affected by changing the temperature which causes the change of line shape. Besides the rate, from Figure 2.5, the intensity attenuation is more severe when the site population is more evenly distributed, and jump angle amplitude is bigger.

### 2.3.2 MAS line shape simulations

As discussed above, the spinning sideband patterns monitor motional regimes, so the simulation of MAS line shape pattern is a direct way to figure out the dynamics within the molecule. The simulation algorism of MAS line shape is like the static line shape except that a rotating frame is added during the calculation, which is spun at a frequency $\nu_R$ around a goniometer whose axis is tilted at 54.74 degrees relative to the direction of the static magnetic field. This rotation imparts a time dependence to the elements of the matrix $\omega_\pm$ , shown in equation (2.2) for the non-rotating case. For the MAS experiment equation (2.1) becomes:

$$\frac{dM_\pm}{dt} = \Gamma(t) M_\pm(t) = \left(i\omega_\pm(t) + \pi\right) M_\pm(t) \tag{2.5}$$

and $\omega_\pm$ is:

$$\omega_\pm(t) = \pm \frac{3e^2qQ}{4\hbar} [\textstyle\sum_{a,b=-2}^{2} D_{0a}^{(2)}(\Omega_{PC})\, D_{ab}^{(2)}(\Omega_{CM}) D_{b0}^{(2)}(\Omega_{ML}(t)) \tag{2.6}$$

Here $\Omega_{CM}$ relates the C frame to the rotating Magic Angle Spinning axis frame which is tilted at 54.74 degree($\theta_m$) relative to the static magnetic field, and the time dependent Euler Angle $\Omega_{ML}(t) = (\omega_r t,\ \theta_m, 0)$ relates the rotating Magic Angle Spinning axis frame to the LAB frame.

Because of the time dependence of $\omega_\pm$ , equation (2.5) cannot be integrated to the form of equation (2.3) by the simple process described above. There are two approaches for accomplishing such an integration. As equation (2.5) has the form of an ordinary differential equation with periodic coefficients, in the sense that $\omega_\pm(t + \tau_R) = \omega_\pm(t)$ where $\tau_R$ is the rotor period, Floquet's theorem is applicable[20]. This means that a coordinate change can be found which converts equation (2.5) to a differential equation with constant coefficients. Floquet's theorem has been used to analyze various periodic motion problems in NMR including dynamic

MAS line shapes,[21] homonuclear and heteronuclear dipolar recoupling experiments, and it is the basis for the dynamic line shape simulation program EXPRESS by Vold and Hoatson.[22]

Another approach, developed by Duer and Levitt,[23] is to numerically integrate equation (2.5) by dividing the rotor period into N intervals each of length $\Delta t = \tau_R / N$ , where N is sufficiently large that during $\Delta t$, $\omega_\pm$ and thus $\Gamma$ are approximately constant. Therefore, at any time m$\Delta$t (i.e. $1 \le m \le N$ ), the MAS propagator can be obtained iteratively:

$$\exp\left(\Gamma\left(m\Delta t\right)\right) \approx \exp\left(\left(i\omega_\pm\left(t_m\right)+\pi\right)\Delta t\right) \times \exp\left(\Gamma\left(\left(m-1\right)\Delta t\right)\right) \tag{2.7}$$

where $t_m=(m-1)\Delta t/2$ and we assume $\Gamma(0)=1$. The propagator for any time $t+M\tau_R$ is then given by:

$$\exp\left(\Gamma\left(t+M\tau_R\right)\right) \approx \left(\exp\left(\Gamma\left(\tau_R\right)\right)\right)^M \times \exp\left(\Gamma\left(t\right)\right) \tag{2.8}$$

Equations (2.7) and (2.8) are the basis for our $^2$H MAS line shape simulation program KLDMAS, which was used to generate all MAS line shape simulations shown in this thesis.

### 2.3.3 Inversion Recovery MAS Simulations

KLDMAS is also used to simulate inversion-recovery MAS experiments. The response of the deuterium spin system to an inversion-recovery pulse sequence is obtained by multiplying the iterated propagator by $(1-2e^{-\tau/\langle T_1\rangle})$ where $\tau$ is the variable time delay between the inversion pulse and the ninety degree pulse, and the spin lattice relaxation rate $R_1 = 1/T_1$ is given by

$$R_1 = 1/T_1 = \frac{3}{16}(\frac{e^2qQ}{\hbar})^2 \cdot [J_1(\omega) + 4J_2(2\omega)] \tag{2.9}$$

In the limit that the rate of spinning exceeds the static spin lattice relaxation rate, and for the case of exchange between N discrete sites, the spectral density has the form[24]:

$$J_m(\omega) = 2\int_0^{\infty} \bar{C}_m(t) Cos(\omega t) dt = \sum_{b=-2}^{2} [d_{mb}^{(2)}(\theta_{lm})]^2 \sum_{a,a'=-2}^{2} D_{ba}^{(2)*}(0,\theta_{mc},\psi_{mc}) D_{ba'}^{(2)}(0,\theta_{mc},\psi_{mc})$$
$$\sum_{nlj=0}^{N-1} X_l^{(0)} X_l^{(n)} X_j^{(0)} X_j^{(n)} D_{a0}^{(2)*}(\phi_l,\theta_l,0) D_{a'0}^{(2)}(\phi_j,\theta_j,0) \frac{-2\lambda_n}{\lambda_n{}^2 + \omega_0{}^2} \qquad (2.10)$$

In equation (2.10) the solid angle $\Omega_{LM} = \left(0, \theta_{lm}, \psi_{lm}(t)\right)$ relates the spinning axis frame M to the laboratory frame L. The angle between the magnetic field direction and the goniometer axis is $\theta_{lm}$ and the angle $\psi_{lm}(t)=\omega_r t$ is time dependent as a result of the sample rotation at a frequency $\omega_r$. The spectral density in equation (2.10) is therefore the cosine Fourier transform of a correlation function $\bar{C}_m(t)$ that has been averaged over the motion of the spinner. Also in equation (2.10), $X$ and $\lambda$ indicate the eigenvector and (diagonal) eigenvalue matrices, respectively of the symmetrized jump matrix.

From Equation (2.10), it's easy to see that $J_m(\omega)$ has a maximum value, hence T1 has a minimum value, when the motion rate is comparable to Larmor frequency $\omega_0$. A double log relationship between the relaxation time and the motion rate is plotted as in figure (2.6). Here we have again used the simple 2 site jump model as described previously. By using this property, temperature dependent study is a straightforward method to judge what motion range the dynamics is in.

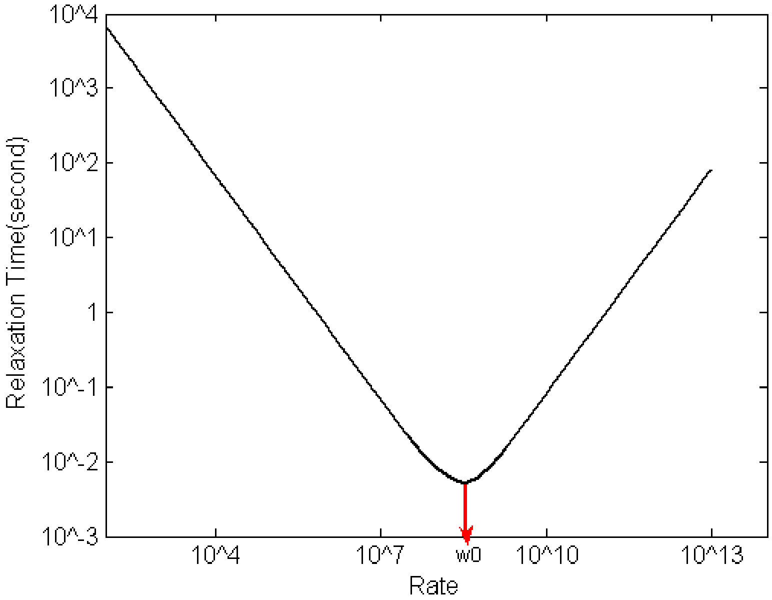

Figure 2.6 Theoretical $^2$H MAS Relaxation Time as function of the rate constant $k=k_{12}=k_{21}$ for a quadrupole coupling tensor whose principal axis system can assume two equally probable orientations relative to the crystallite fixed axis system. The orientations were given by $\Omega(\alpha,\beta,\gamma)=\{0,\pi/3,0\}$ and $\{0,\pi/3,\pi\}$. The calculations employed QCC=170 kHz, asymmetry parameter $\eta=0$, spin frequency $\upsilon_r=8$ kHz, and Lorentzian line broadening of 1 kHz. The calculation employs ideal inversion efficiency. The red arrow represents Larmor frequency, which is close to the minimum point of the curve.

## 2.4 MAS Simulation Program: KLDMAS

As mentioned above, the quadrupole echo line shape can be simulated by using MXET1. However, there were no public mature programs that can simulate Deuterium MAS line shape perfectly until EXPRESS was developed by Vold and hoatson.[22] Although both are coded in MATLAB, unlike EXPRESS which can simulate several different experiments besides Deuterium MAS, our KLDMAS is a small program designed specifically for simulations of Deuterium MAS experiment. Another difference is that EXPRESS is using Floquet's theorem, while our program is using Duer's method[23]. A direct comparison was made to show that the CPU time that these two programs need are approximately on the same level. Although a single MAS line shape simulation time is much bigger than quadrupole echo simulation, KLDMAS adopted annealing algorithm to automate the simulation process, which greatly decreased the simulation time.

### 2.4.1 KLDMAS Overview

In current version of KLDMAS, a MATLAB graphical interface is used to facilitate the user. The interface mainly asks the user to input a set of experimental parameters or simulation model descriptions, based on these parameters, the inner program calculate the line shape or $T_1$, and display in a new window. The experimental parameters include loading of experimental data, so that the comparison between experiment and simulation can happen. The simulation model interface asks a series of questions to specify the model, including the number of frames, site populations, site angles, quadrupole coupling constant, asymmetry parameters, etc. Most of these parameters are just initial values that will change during the simulations.

Like MXET1, KLDMAS uses the frame transformation order from LAB frame all the way to PAS frame. Usually it's difficult to directly figure out the Euler angles between these two frames, and it's much easier to visualize the site within the molecule if the crystal frame is inserted, so a multiple transformation is needed during the simulations. The axis frame transformation from LAB frame to magic angle spinning axis frame(MAS), and from MAS to the crystal frame(CRY) is encoded in the program, and the user needs to figure out the frame transformation angles from CRY to PAS. Usually multiple transformations are needed when it's necessary to insert another intermediate frames between them. KLDMAS let user choose if it's single axis frame transformation or double axis frame transformation, within each choice, the user need to specify the site information in each axis frame.

### 2.4.2. Site Connectivity in PAS Frame

Within PAS frame, the program assumes that the rotational jumps from one site can only goes to the neighboring site, and a single rate constant is sufficient to describe the jump frequency between the two sites. In MXET1 and EXPRESS, the site "connectivity" includes all sites(jumps with equal probability from each site to any other), jumps along a chain, or jumps along a ring(neighboring site). Since in our work in the thesis, the neighboring site jump is sufficient to use, other types of site "connectivity" may be considered in the next version of KLDMAS.

### 2.4.3. Unequal site populations

The site populations are used to form the jump matrix π as in equation (2.1). In the case of neighboring site jump, the jump matrix element $\pi_{ij}$ is the rate for the jump from site j to site i, and $\pi_{ii}$ is the negative sum off all rates which deplete site i. $\pi$ satisfies microscopic reversibility:

$$\pi_{ij}P_j = \pi_{ji}P_i \tag{2.11}$$

And $P_i$ is site population at equilibrium.

In the case of neighboring site jump , the jump matrix π can be written as following:

$$\begin{aligned} &\pi_{ij} = C\left(\frac{P_i}{P_j}\right)^{\frac{1}{2}} \qquad (j = i \pm 1) \\ &\pi_{ii} = -\left(\pi_{i,i-1} + \pi_{i,i+1}\right) \\ &\pi_{ij} = 0 \quad \text{other case} \end{aligned} \tag{2.12}$$

Here C is the jump rate constant, which is approximately inverse of correlation time.

However, in the case of unequal site populations, the matrix needs to be symmetrized to satisfy the microscopic reversibility (2.11). The transformation uses a symmetrization matrix T, where T is a diagonal matrix with its i th diagonal element being $\sqrt{P_i}$ . Then the new jump matrix $\pi'$ is becoming

$$\pi' = T^{-1}\pi T \tag{2.13}$$

In the internal calculation of the program, KLDMAS automatically converts the unsymmetrized matrix into symmetrized matrix, and calculates the complex eigenvalues of the propagator matrix.

### 2.4.4 Powder averaging and dividing of one rotor period

The computation of MAS spectra is demanding for two reasons. One is the number of crystal orientations, the other is number of dividing of one rotor period.

In both MAS and quadrupole echo line shape simulations, the number of crystal orientations is a big factor for the computation time, since the simulation for a single site needs to be repeated for many different powder orientations. In MAS simulations, this is even more time consuming because dividing the rotor period into many equally small intervals, each powder averaged simulation step has to be repeated for the next interval. If we use more crystal orientations, and use more dividing intervals, the simulation accuracy can be higher, but this also means higher simulation time. So the actual simulation is compromise between accuracy and timing issues.

In KLDMAS, we use the commonly used ZCW angle sets[25,26] for the powder average. Only 3 ZCW sets are used, ZCW100, ZCW1154 and ZCW6044. In the first round of simulations, the fewer orientations are used to speed up the simulation process; when the simulation is close to the data, the biggest number of orientations is used to more accurately simulate the line shape. The same simulation pattern also works for the dividing of the rotor period. In the beginning of the simulation, usually only 64 intervals are divided in one rotor period; while at the end of the simulation, 256 intervals or even 512 intervals are adopted to simulate the line shape accurately. After the first interval, the rest of the fid is just the repetition of the first one, so the calculation of the rest fid is becoming much easier. Note here the number of intervals as integer exponential of 2 is just my preference, users can decide whatever number they want in the dividing of the rotor period, but the total number in the fid has to be integer exponential of 2 as a request by Fast Fourier Transform.

### 2.4.5 Calculation of Least Square and Automation of the program

The simulation of the MAS line shape involves comparison between calculated line shape and experimental line shape. A direct overlapping of the two line shapes in quadrupole echo simulations, and calculating their difference square for each point in the line shape works perfectly, however, this does not work for MAS simulation. This is because the experimental spinning side bands are not always exactly at integer number of spinning frequency as the simulated spinning side bands do, and since the peaks are usually very narrow and high, a mismatch of a single point can create big difference square, which brings the distortion of the simulation. So instead of comparing every point in the line shape, we compare the least square of the peaks' intensity.

Given an initial parameter set, the KLDMAS program automatically vary the parameters within the specified ranges, and compare the resulting line shape simulation with data quantitatively by calculating the $\chi^2$ parameter, the sum of squared differences between experimental and simulated side band intensities. The process of searching for parameter sets that minimize the squared difference between the side bands intensities of the experimental and computed $^2$H MAS spectra was automated using a threshold accepting(TA) algorithm[27] as described in the following paragraph.

A positive value called the threshold T is initially set. An initial parameter set is used to calculate a MAS line shape , which is compared to the experimental MAS lineshape and used as a basis for a $\chi^2$ calculation. The parameter set is then stochastically perturbed and the procedure is repeated to obtain a new $\chi^2$. The two $\chi^2$ are compared. If $\chi^2$(old)- $\chi^2$(new)<T, then the new variable set is accepted, otherwise it is rejected. As simulations proceed, the threshold value T is manually decreased until it goes to zero. The primary difference between the TA method and simulated annealing (SA) is that, instead of using a constant threshold value, the SA method uses

a probability which depends on a time-dependent temperature. We found that both methods can give satisfactory result but the TA method is faster. A flow chart of the simulations by using KLDMAS is shown in figure 2.7. By using this automation method, the simulation time is greatly decreased.

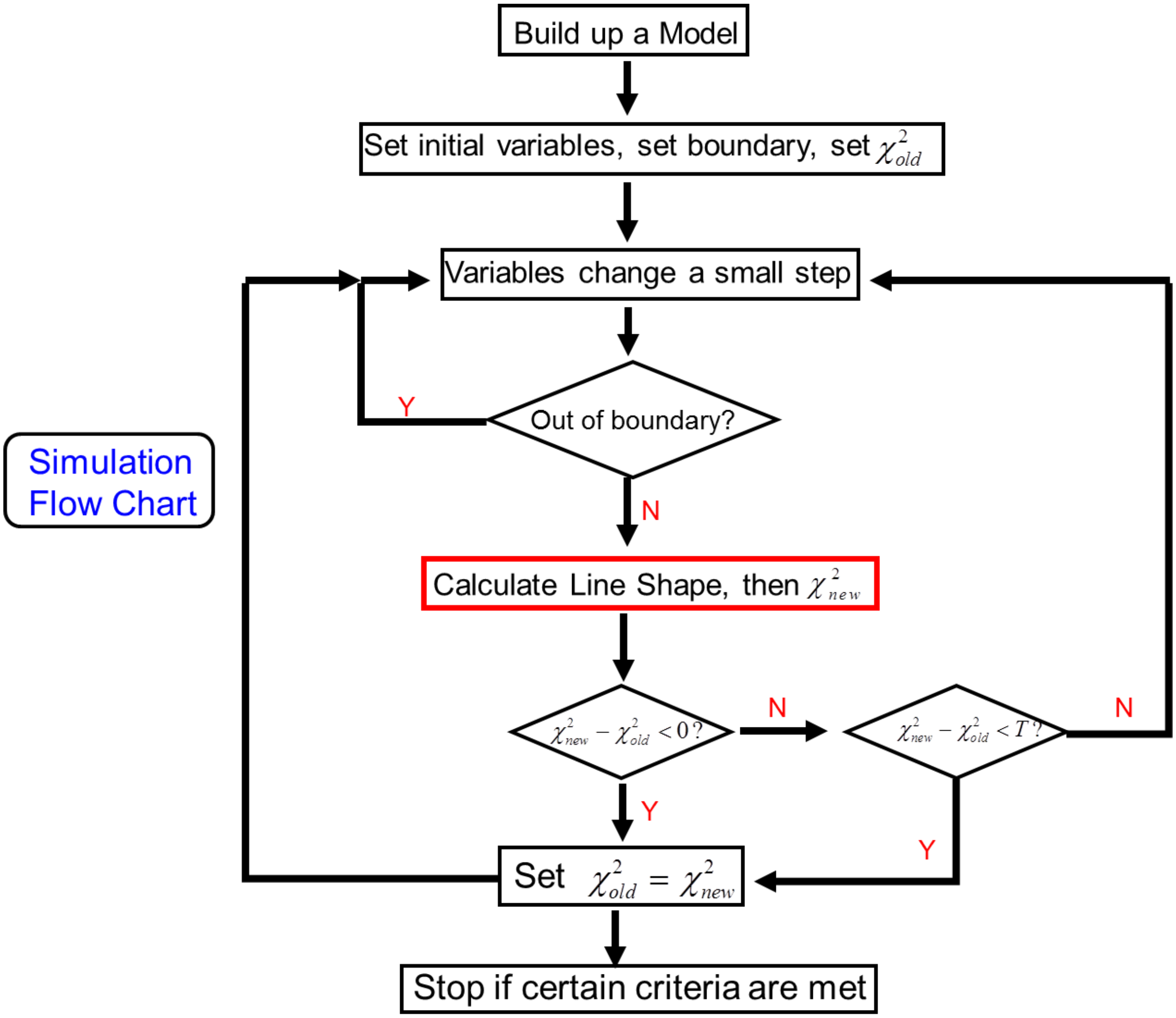

Figure 2.7 Flow chart of MAS simulations by using KLDMAS

## 2.5 KLDMAS Simulations on Model Compounds

To test the code, several model coumpound line shapes were taken and simulated by KLDMAS. The model compounds are deuterated small molecules whose motions are well known.

### 2.5.1 Simulation of Dimethylsulfone(DMSO2) line shape

DMSO2 molecule is mentioned above, and here we use it as an example again. DMSO2 is having 2 axis motion: the deuterated methyl group is having fast rotation around S-C bond, and the two methyl groups are exchanging slowly around the symmetry axis of the molecule. We can simulate its motion by using this 2 axis frame, or we can treat the methyl group as a single bond and only do 1 axis frame simulation because of its fast rotation. Both simulation models give out identical result and the comparison with experimental data is showing below:

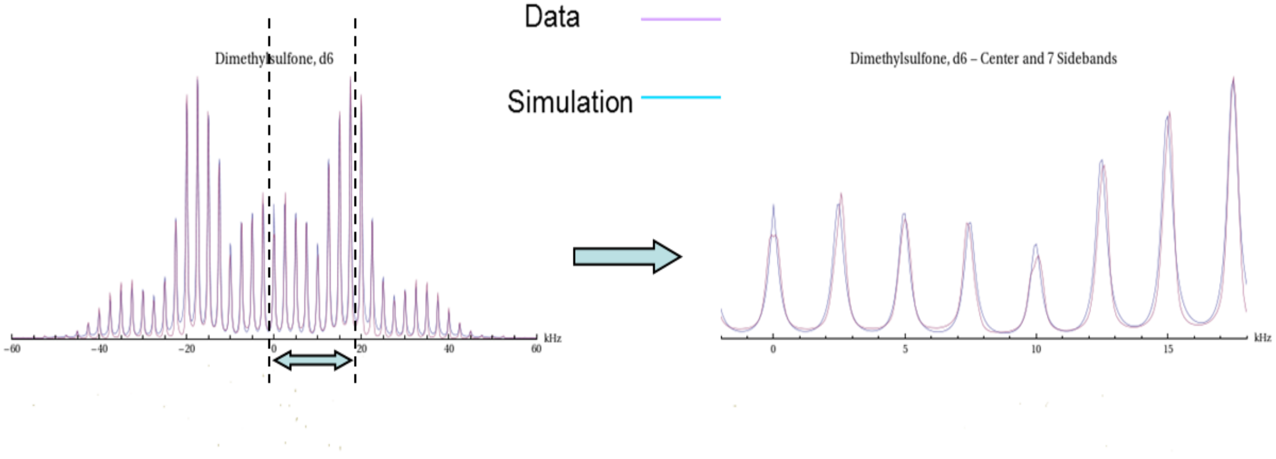

(a) (b)

Figure 2.8 Simulation of DMSO2 line shape vs Data
(a) An overlapping view of DMS experimental line shape and simulation. The simulation can adopt either single axis frame simulation or 2 axis frame simulation, both gives the same result.
(b) The area between the dotted line in (a) is amplified for a better view.

### 2.5.2 Simulation of hexamethylbenzene(HMB) line shape

As another well-understood test compound, the MAS spectrum of hexamethylbenzene-$d_{18}$ (HMB) was simulated and compared to an experimentally collected spectrum at a spinning speed of 1655 Hz and a $^{2}$H Larmor frequency of 61.4 MHz. Good agreement was obtained.

HMB is also having 2 axis motion: besides the fast methyl group rotation, the ring itself is doing fast rotation too. Thus the simulation used a double axis model:

Axis 1, methyl rotation: 3 site jump, $k$=5.0×10$^{10}$ s$^{-1}$;

Axis 2, ring rotation: 6 site (nearest-neighbor) jump, $k$=1.5×10$^{8}$ s$^{-1}$;

Quadrupole constant, QCC$_{\mathrm{eff}}$=47 kHz.

With the exception of the quadrupole constant, all values are identical to those in literature, e.x, the values obtained by Vold[28] et al. The simulation vs line shape data is shown in figure 2.9 below:

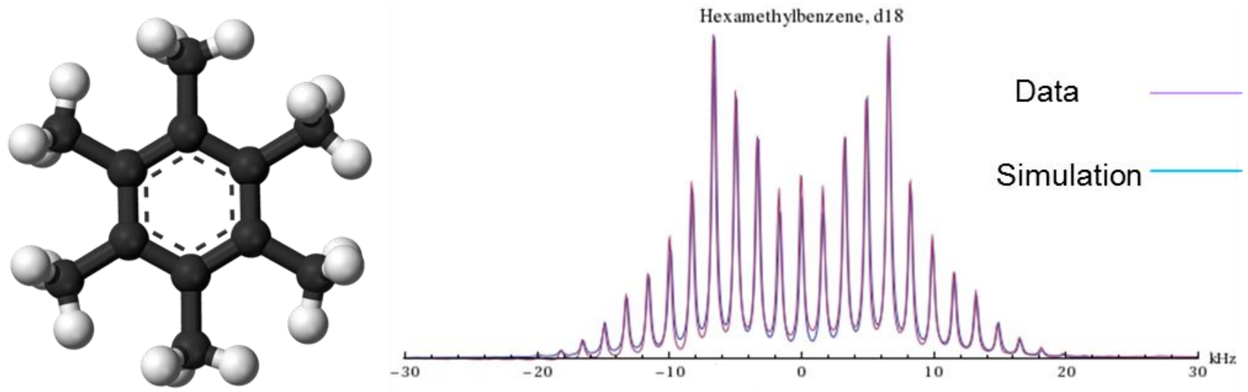

(a) (b)

Figure 2.9 Simulation of HMB line shape vs Data
(a) A model of Hexamethylbenzene molecule;
(b) The overlapping of experiental line shape and simulation. Experimental line shape is given in purple and simulation fit in blue.

Figure 2.8 and 2.9 show that KLDMAS can simulate the motion perfectly for these model compounds. Test simulations were also done on other model compound, like alanine, or simple amino acid, like [5,6]-2'-deoxycytidine. All have given satisfactory match, which gave us confidence that we can apply the code on more complex dynamic systems, like the side chain movement on surfaces.

# Appendix II: Sample MATLAB code in KLDMAS

## 1. User Interface: Specify the model parameters by inputting frame information, site information, and T1 information

```
function varargout = magicanglespinningsimulation(varargin)
gui_Singleton = 1;
gui_State = struct('gui_Name',       mfilename, ...
                   'gui_Singleton',  gui_Singleton, ...
                   'gui_OpeningFcn', @magicanglespinningsimulation_OpeningFcn, ...
                   'gui_OutputFcn',  @magicanglespinningsimulation_OutputFcn, ...
                   'gui_LayoutFcn',  [] , ...
                   'gui_Callback',   []);
if nargin && ischar(varargin{1})
    gui_State.gui_Callback = str2func(varargin{1});
end

if nargout
    [varargout{1:nargout}] = gui_mainfcn(gui_State, varargin{:});
else
    gui_mainfcn(gui_State, varargin{:});
end

function magicanglespinningsimulation_OpeningFcn(hObject, eventdata, handles, varargin)
handles.output = hObject;
guidata(hObject, handles);

function varargout = magicanglespinningsimulation_OutputFcn(hObject, eventdata, handles)
varargout{1} = handles.output;
function popupmenu2_Callback(hObject, eventdata, handles)

val1=get(hObject,'Value');
str1=get(hObject,'String');
global wr nps nptotal naxis nsite1 p1 prosite QCC nsite2 nsite theta1 phi1 p2 theta2 phi2 lb numtau tau invefficiency ntau dfrate1 dfrate2;
switch str1{val1}
    case '1'
      naxis=1;
    case '2'
        naxis=2;
end
if naxis==1
    prompt = {'# exchange sites','site probability(use , to seperate numbers,same as follows)','theta of each site','phi of each site','exchange rate','QCC(kHz)','Lorentzian(kHz)','How many points are calculated in one rotation?','Total points in the simulation spectra','magic angle spinning speed(unit:kHz)'};
    dlg_title = 'Simulation Parameters for Single Axis';
    num_lines = 1;
    exparameter = inputdlg(prompt,dlg_title,num_lines);
    numStr = length(exparameter);
    realInput = [];
    realInput=zeros(numStr,10);
    for j = 1:numStr,
        a=size(convertStr2Num(exparameter{j}));
        b=a(1,2);
        realInput(j,1:b) = convertStr2Num(exparameter{j});
```

```
   end
   nsite=realInput(1);
   p1=zeros(1,nsite);
   for i=1:nsite
      p1(1,i)=realInput(2,i);
      theta1(i)=realInput(3,i)*pi/180;
      phi1(i)=realInput(4,i)*pi/180;
   end

   dfrate1=realInput(5,1);
   QCC=realInput(6,1);
   lb=realInput(7,1)*10^3*pi;
   nps=realInput(8,1);
   nptotal=realInput(9,1);
   wr=realInput(10,1)*10^3;
elseif naxis==2
    prompt = {'# exchange sites for axis 1(principal frame to intermediate frame)','site probability for axis 1(use , to seperate numbers)','theta of each site for axis 1','phi of each site for axis 1','exchange rate for axis 1','# exchange sites for axis 2(intermediate frame to molecular frame)','site probability for axis 2(use , to seperate numbers)','theta of each site for axis 2','phi of each site for axis 2','exchange rate for axis 2','QCC(kHz)','Lorentzian(kHz)','How many points are calculated in one rotation?','Total points in the simulation spectra','magic angle spinning speed(unit:kHz)'};
    dlg_title = 'Simulation Parameters for Double Axis';
    num_lines = 1;
    exparameter = inputdlg(prompt,dlg_title,num_lines);
    numStr = length(exparameter);
    realInput = [];
    realInput=zeros(numStr,10);
    for j = 1:numStr,
       a=size(convertStr2Num(exparameter{j}));
       b=a(1,2);
       realInput(j,1:b) = convertStr2Num(exparameter{j});
    end
    nsite1=realInput(1);
    for i=1:nsite1
       p1(1,i)=realInput(2,i);
       theta1(i)=realInput(3,i)*pi/180;
       phi1(i)=realInput(4,i)*pi/180;
    end
    dfrate1=realInput(5,1);
    nsite2=realInput(6,1);
    nsite=nsite1*nsite2;
    for i=1:nsite2
       p2(1,i)=realInput(7,i);
       theta2(i)=realInput(8,i)*pi/180;
       phi2(i)=realInput(9,i)*pi/180;
    end
    dfrate2=realInput(10,1);
    QCC=realInput(11,1);
    lb=realInput(12,1)*10^3*pi;
    nps=realInput(13,1);
    nptotal=realInput(14,1);
    wr=realInput(15,1)*10^3;
end

function popupmenu2_CreateFcn(hObject, eventdata, handles)
if ispc && isequal(get(hObject,'BackgroundColor'), get(0,'defaultUicontrolBackgroundColor'))
```

```
    set(hObject,'BackgroundColor','white');
end

function popupmenu3_Callback(hObject, eventdata, handles)
val1=get(hObject,'Value');
str1=get(hObject,'String');
global tau numtau invefficiency ntau;
switch str1{val1}
    case 'No'
      ntau=0;
    case 'Yes'
        ntau=1;
end
if ntau==1
    prompt = {'Tau(ms)','Inversion Efficiency'};
    dlg_title = 'Inversion Pulse Separation';
    num_lines = 1;
    exparameter = inputdlg(prompt,dlg_title,num_lines);
    numStr = length(exparameter);
    realInput = [];
    realInput=zeros(numStr,15);

        a=size(convertStr2Num(exparameter{1}));
        numtau=a(1,2);
        realInput(1,1:numtau) = convertStr2Num(exparameter{1});
        tau(1,1:numtau)=realInput(1,1:numtau)*10^-3;
        tau(1,numtau+1)=tau(1,numtau)*10;

         realInput(2) = convertStr2Num(exparameter{2});

    invefficiency=realInput(2);
end
function popupmenu3_CreateFcn(hObject, eventdata, handles)
if ispc && isequal(get(hObject,'BackgroundColor'), get(0,'defaultUicontrolBackgroundColor'))
    set(hObject,'BackgroundColor','white');
end


function pushbutton2_Callback(hObject, eventdata, handles)
st=cputime;
global nptotal wr nps wQ nc naxis nsite nsite1 nsite2 nsite3 QCC naxis p1 theta1 phi1 prosite1 prosite p2 theta2
phi2 dfrate1 dfrate2 lb numtau tau invefficiency ntau;
```

## 2. Construct symmetrized, one frame Jump Matrix

```
if naxis==1
    prosite=p1;
    for ii=1:nsite
        for jj=ii+1:nsite
            if (jj-ii==1) | (jj-ii==nsite-1)
                JM(ii,jj)=sqrt(p1(ii)/p1(jj));
                JM(jj,ii)=1/JM(ii,jj);
            else JM(ii,jj)=0;
            end
        end
```

```
    end
    for ii=1:nsite
        JM(ii,ii)=-sum(JM(:,ii));
    end
    JM=dfrate1*JM;

else
    prosite=kron(p2,p1);
    for ii=1:nsite
        for jj=ii+1:nsite
            Nrowi=floor((ii-1)/nsite1)+1;
            Ncolumni=floor((jj-1)/nsite1)+1;
            subrowi=ii-(Nrowi-1)*nsite1;
            subcolumni=jj-(Ncolumni-1)*nsite1;
            if Nrowi==Ncolumni
                 if subcolumni-subrowi==1 | subcolumni-subrowi==nsite1-1
                   JM(ii,jj)=dfrate1*sqrt(prosite(1,ii)/prosite(1,jj));
                   JM(jj,ii)=dfrate1*sqrt(prosite(1,jj)/prosite(1,ii));
                  else JM(ii,jj)=0;
                  end


              elseif abs(Nrowi-Ncolumni)==1 | abs(Nrowi-Ncolumni)==nsite2-1
                if abs(subrowi-subcolumni)==0
                   JM(ii,jj)=dfrate2*sqrt(prosite(1,ii)/prosite(1,jj));
                   JM(jj,ii)=dfrate2*sqrt(prosite(1,jj)/prosite(1,ii));
                end
            end
        end
    end

        for i=1:nsite
            JM(i,i)=-sum(JM(:,i));
        end
end


T=diag(sqrt(prosite));
Ti=inv(T);
JM1 = Ti*JM*T;
```

## 3. Construct site specific ω matrix

```
D2LM0=D2(0,magicangle,0);
D2LM=D2LM0(3,:);
D2LM1=D2LM0(4,:);
D2LM2=D2LM0(5,:);
D2CP=zeros(5,nsite);
gammastep=[exp(2*sqrt(-1)*2*pi/nps) exp(sqrt(-1)*2*pi/nps) 1 exp(-sqrt(-1)*2*pi/nps) exp(-2*sqrt(-1)*2*pi/nps)];
if naxis==1
    for i=1:nsite
    D2CP0=D2(phi1(i),theta1(i),0);
    D2CP(:,i)=transpose(D2CP0(:,3))+0.41*eta*(transpose(D2CP0(:,1))+transpose(D2CP0(:,5)));
    end
elseif naxis==2
    D2CI=zeros(nsite2,5,5);
```

```
    for i=1:nsite2
    D2CI(i,:,:)=D2(phi2(i),theta2(i),0);
    end

D2IP=zeros(5,nsite1);
   for i=1:nsite1
       D2IP0=D2(phi1(i),theta1(i),0);
       D2IP(:,i)=transpose(D2IP0(:,3))+0.41*eta*(transpose(D2IP0(:,1))+transpose(D2IP0(:,5)));;
    D2IP(:,i)=transpose(D2IP0(:,3));
   end

    for i=1:nsite2
        temp1=reshape(D2CI(i,:,:),5,5);
        for j=1:nsite1
            temp2=D2IP(:,j);
            D2CP(:,(i-1)*nsite1+j)=temp1*temp2;
        end
    end
end

%w=D2LM*D2MC*D2CP
```

## 4. T1 inversion recovery part

```
if ntau==1
R=JM1;
[X,LamdaR]=eig(R);
templamda=0;
for i=1:nsite
    if templamda<abs(LamdaR(i,i))
        templamda=abs(LamdaR(i,i));
    end
end
eps=10^-12;
for i=1:nsite
    if abs(LamdaR(i,i))/templamda<eps
        LamdaR(i,i)=0;
    end
end

J1CPpart=zeros(5,5);
J2CPpart=zeros(5,5);



sqrootsitepop=transpose(sqrt(prosite));
eigenvectormem=zeros(5,nsite);
for a=-2:2
    for n=1:nsite
      eigenvectormem(a+3,n)=sum(X(:,2).*X(:,n).*transpose(conj(D2CP(a+3,:))));
   eigenvectormem(a+3,n)=sum(sqrootsitepop.*X(:,n).*transpose(conj(D2CP(a+3,:))));%
   eigenvectormem(a+3,n)=sum(sqrootsitepop.*X(:,n).*transpose(D2CP(a+3,:)));
    end
end
```

```
 for a=-2:2
  for a1=-2:2

for n=1:nsite

J1cptemp=eigenvectormem(a1+3,n)*conj(eigenvectormem(a+3,n))*2*(-LamdaR(n,n))/(LamdaR(n,n)^2+w0^2);
J2cptemp=eigenvectormem(a1+3,n)*conj(eigenvectormem(a+3,n))*2*(-LamdaR(n,n))/(LamdaR(n,n)^2+(2*w0)^2);
J1CPpart(a+3,a1+3)= J1CPpart(a+3,a1+3)+J1cptemp;
 J2CPpart(a+3,a1+3)= J2CPpart(a+3,a1+3)+J2cptemp;
    end
   end
 end

T1coef=zeros(1,ncrys);
 J1=zeros(1,ncrys);
 J2=zeros(1,ncrys);
for o=1: ncrys
   beta=jk2(o,2);
  gamma=jk2(o,3);
   temp=D2(0,beta,gamma);

 tempJ1=0;
 tempJ2=0;
    for b=-2:2
     for a=-2:2
      for a1=-2:2
  tempJ1=(D2LM1(b+3))^2*conj(temp(b+3,a+3))*temp(b+3,a1+3)*J1CPpart(a+3,a1+3); J1(1,o)=J1(o)+tempJ1;
  tempJ2=(D2LM2(b+3))^2*conj(temp(b+3,a+3))*temp(b+3,a1+3)*J2CPpart(a+3,a1+3); J2(1,o)=J2(o)+tempJ2;
      end
     end
    end
end

for n1=1:numtau+1
    for o=1:ncrys
       T1coef(1,o)=1-2*invefficiency*exp(-tau(1,n1)*0.75*pi^2*(1.7*10^5)^2*(J1(1,o)+4*J2(1,o)));
T1coef(n1,o)=1-2*0.96*exp(-tau(1,n1)*0.75*pi^2*(1.7*10^5)^2*(J1(1,o)+4*J2(1,o)));
    end
end

else
    T1coef=ones(1,ncrys);
    numtau=0;
end
```

## 5. Calculate fid and Plot symmetrized line shape

```
M=zeros(1,nptotal);
Mmemory=zeros(nps+1,ncrys);
damprate=zeros(1,ncrys);
D2MC=zeros(ncrys,5,5);
for o=1:ncrys
    alpha=jk2(o,1);
    beta=jk2(o,2);
```

```
   gamma=jk2(o,3);
   D2MC(o,:,:)=D2(alpha,beta,gamma);
end
   for n=1:nps+1
      D2LM=D2LM.*gammastep;
      for o=1:ncrys
          temp=reshape(D2MC(o,:,:),5,5);
          JM=JM1+sqrt(-1)*wQ*(diag(real(D2LM*temp*D2CP)));
     c0(:,o)=T*expm(JM*delta)*Ti*c0(:,o);
      end
      broading=exp(-n*lb*delta);

     Mmemory(n,:)=ones(1,nsite)*c0*broading;
end
damprate=Mmemory(nps+1,:)./Mmemory(1,:);


 T1data=zeros(1,numtau+1);
 expsw=300000;
deltasw=1/(nptotal*delta);
ndata=floor(expsw/deltasw);
 data2=zeros(ndata,numtau+2);


 gb=0;
  for n1=1:numtau+1
     for n=1:nptotal
      i=floor((n-1)/nps);
   M(n)=T1coef*transpose(Mmemory(n-nps*i,:).*damprate.^(i+1))*exp(-(n*gb*delta)^2);
   end


Spec=fft(real(M));
temp=zeros(1,nptotal-1);
temp(1:(nptotal/2-1))=Spec(nptotal/2+1:nptotal-1);
temp(nptotal/2:nptotal-1)=Spec(1:nptotal/2);
f1(1:nptotal-1)=temp(1:nptotal-1)+temp(nptotal-1:-1:1);
 end



temp1=abs(real(f1(nptotal/2)));
midpoint=floor(ndata/2);
for i=1:ndata
   faxis(i)=deltasw*(i-midpoint-1);
   A(i)=real(f1(nptotal/2-midpoint+i-1)-f1(nptotal/2-midpoint));
  data2(i,1+n1)=A(i);
end
T1data(1,n1)=sum(A(1:ndata)/ndata);

h=figure;plot(faxis,A);
saveas(h,filename,'jpg');
```

## 6. Euler Rotation Matrix

To rotate an object from axis frame (X, Y, Z) to another axis frame (x, y, z), the rotation matrix has to use Euler angles($\alpha$, $\beta$, $\gamma$). The transformation begins with the rotation of $\gamma$ about Z, and the rotation matrix for this process is

$$R_z(\gamma) = \begin{pmatrix} \cos\gamma & -\sin\gamma & 0 \\ \sin\gamma & \cos\gamma & 0 \\ 0 & 0 & 1 \end{pmatrix} \tag{A.1}$$

then a rotation of β around Y:

$$R_Y(\beta) = \begin{pmatrix} \cos\beta & 0 & \sin\beta \\ 0 & 1 & 0 \\ -\sin\beta & 0 & \cos\beta \end{pmatrix} \tag{A.2}$$

and finally a rotation of α around Z:

$$R_z(\alpha) = \begin{pmatrix} \cos\alpha & -\sin\alpha & 0 \\ \sin\alpha & \cos\alpha & 0 \\ 0 & 0 & 1 \end{pmatrix} \tag{A.3}$$

So the total rotation matrix by combining the three is

$$R(\alpha,\beta,\gamma) = R_z(\alpha)R_Y(\beta)R_z(\gamma) = \begin{pmatrix} \cos\alpha\cos\beta\cos\gamma - \sin\alpha\sin\gamma & -\cos\alpha\cos\beta\sin\gamma - \sin\alpha\cos\gamma & \cos\alpha\sin\beta \\ \sin\alpha\cos\beta\cos\gamma + \cos\alpha\sin\gamma & -\sin\alpha\cos\beta\sin\gamma + \cos\alpha\cos\gamma & \sin\alpha\sin\beta \\ -\sin\beta\cos\gamma & \sin\beta\sin\gamma & \cos\beta \end{pmatrix} \tag{A.4}$$

7. Wigner Rotation Matrix

The Wigner rotation matrix D used in KLDMAS is saved as a function named D2, which has the code as the following:

```
function d = D2(x,y,z)
d =
[exp(2*sqrt(-1)*(x+z))*0.25*(1+cos(y))^2    exp(sqrt(-1)*(2*x+z))*0.5*sin(y)*(1+cos(y))  exp(2*sqrt(-
1)*x)*sqrt(0.375)*sin(y)^2  exp(sqrt(-1)*(2*x-z))*0.5*sin(y)*(1-cos(y))  exp(2*sqrt(-1)*(x-z))*0.25*(1-cos(y))^2;

    exp(sqrt(-1)*(x+2*z))*(-0.5)*sin(y)*(1+cos(y))  exp(sqrt(-1)*(x+z))*0.5*(2*cos(y)-1)*(1+cos(y))  exp(sqrt(-
1)*x)*sqrt(1.5)*sin(y)*cos(y)  exp(sqrt(-1)*(x-z))*0.5*(2*cos(y)+1)*(1-cos(y))   exp(sqrt(-1)*(x-
2*z))*(0.5)*sin(y)*(1-cos(y));

    exp(2*sqrt(-1)*z)*sqrt(0.375)*sin(y)^2  exp(sqrt(-1)*z)*(-sqrt(1.5))*sin(y)*cos(y)  0.5*(3*cos(y)^2-1)  exp(-
sqrt(-1)*z)*sqrt(1.5)*sin(y)*cos(y)  exp(-2*sqrt(-1)*z)*sqrt(0.375)*sin(y)^2;

    exp(-sqrt(-1)*(x-2*z))*(-0.5)*sin(y)*(1-cos(y))  exp(-sqrt(-1)*(x-z))*0.5*(2*cos(y)+1)*(1-cos(y))  exp(-sqrt(-
1)*x)*(-sqrt(1.5))*sin(y)*cos(y)  exp(-sqrt(-1)*(x+z))*0.5*(2*cos(y)-1)*(1+cos(y))   exp(-sqrt(-
1)*(x+2*z))*(0.5)*sin(y)*(1+cos(y));

    exp(-2*sqrt(-1)*(x-z))*0.25*(1-cos(y))^2  exp(-sqrt(-1)*(2*x-z))*(-0.5)*sin(y)*(1-cos(y))  exp(-2*sqrt(-
1)*x)*sqrt(0.375)*sin(y)^2  exp(-sqrt(-1)*(2*x+z))*(-0.5)*sin(y)*(1+cos(y))  exp(-2*sqrt(-
1)*(x+z))*0.25*(1+cos(y))^2];
```

# Chapter III

# Use Static Solid-State Deuterium NMR to Study the Side Chain Dynamics of Peptides Adsorbed onto Polystyrene Surface

## Abstract:

The artificial amphiphilic peptide LKα14 adopts a helical structure at interfaces, with opposite orientation of its leucine(L, hydrophobic) and lysine(K, hydrophilic) side chains. When peptides are adsorbed onto surfaces, different residue side chains necessarily have different proximities to the surface, depending on both their position in the helix and the composition of the surface itself. Deuterating the individual leucine residues(isopropyl-$d_7$) permits the use of solid state deuterium NMR spectroscopy as a site-specfic probe of side chain dynamics. In conjunction with sum-frequency generation as a probe of the peptide-binding face, we demonstrate that the mobility of specific leucine side chains at the interface is quantifiable in terms of their surface proximity.

## 3.1 Introduction

Development of biocompatible material surfaces is a major focus of the materials and tissue engineering communities[29-33], particularly for using peptide or protein coatings in recreating a natural extracellular matrix to direct wound repair or tissue development and homeostasis.[34-37] Many of the current materials used in biomedical materials and tissue-engineering scaffolds are hydrophobic.[38-41] However, proteins often lose functionality when adsorbed onto hydrophobic surfaces, so a major concern in these applications is retention of structure and/or dynamics. Deuterium solid-state nuclear magnetic resonance spectroscopy(NMR) is a versatile, nonperturbing probe for those parameters.[42-44]

Degrado and Lear first demonstrated synthetic peptides that adopt a chosen structure and orientation at interfaces using alternating periods of leucine (L) and lysine (K) residues[45]. At hydrophobic surfaces, rather than unfolding, these use a recognition method to stabilize a given secondary structure where the planar environment restricts the conformational degrees of freedom. Previously, we used NMR to explore a structural determination approach using one such 14-residue "LK" peptide, Ac-LKKLLKLLKKLLKL-OH(designated as LK$\alpha$14), wherein dipolar recoupling and double-quantum NMR techniques were used to measure $\phi$ and $\psi$ Ramachandran angles in adjacent carbonyl-carbonyl pairs, thus quantifying the local secondary structure of the peptide adsorbed on a hydrophobic polystyrene(PS) surface[46].

The interactions of multiple amphiphilic peptides with PS and silica surfaces has also been studied by Somorjai and co-workers[47,48] using sum frequency generation (SFG) vibrational spectroscopy. They demonstrated that LK$\alpha$14 adsorbs onto PS surface with the leucine side chains alongside and lysine side chains opposite that surface.

Here we demonstrate how solid state deuterium NMR can be used to site-specifically and quantifiably define the perturbations of amino acid side-chain dynamics induced by peptide adsorption to a hydrophobic surface. In this initial study, we used a series of selectively deuterated LK$\alpha$14 peptides, where [isopropyl-$^2H_7$]L-leucine ($d_7$Leu) (see Figure 3.1a) was incorporated at individual sites in the peptide's primary sequence.

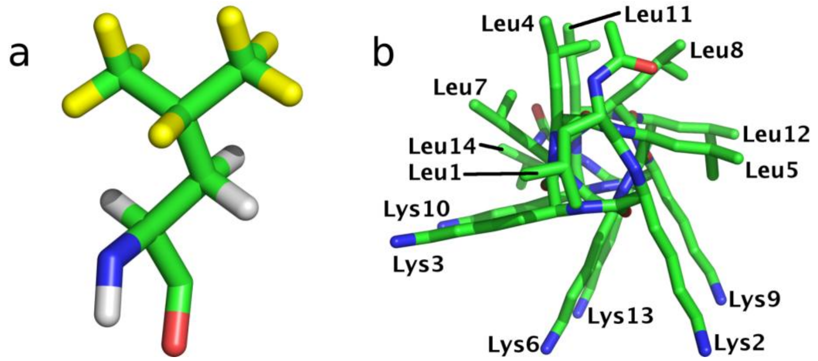

Figure 3.5. Structure of $d_7$Leu and End-on view of LKα14 peptide
(a) Structure of $d_7$Leu, with deuterated sites highlighted in yellow.
(b) End-on view of LKα14 helical structure with residues labeled.

## 3.2 Experimental Spectra and Calculations

Figure 3.2a shows the deuterium NMR spectrum of unbound, lyophilized LKα14 with $d_7$Leu incorporated at position L8. Figures 3.2b-e displays spectra of PS-physisorbed and subsequently lyophilized LKα14 with $d_7$Leu incorporated selectively at L5, L8, L11, and L14. Figure 3.2f shows the spectrum of LKα14 with $d_7$Leu incorporated at L8 but adsorbed onto 14 nm diameter colloidal gold particles coated with a self-assembled monolayer (SAM) of carboxyl-terminated alkane thiolates, $COOH(CH_2)_{16}SH$.

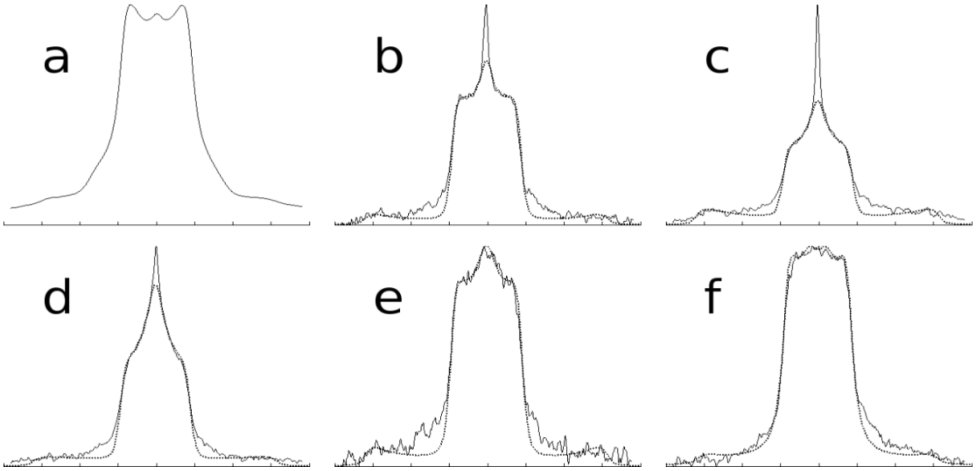

Figure 3.6. $^2$H NMR spectra (solid lines) and simulation (dashed lines, b-f only) of LKα14 labeled at different positions.
(a) free LKα14, $d_7$Leu8;
polystyrene-bound LKα14 samples labeled at (b) L5, (c) L8, (d) L11, (e) L14; (f) L8 bound to carboxyl-functionalized gold nanoparticles. Tick marks represent 20 kHz intervals.

A striking aspect of the spectra in Figure 3.2 is that none resemble the deuterium NMR spectrum of polycrystalline $d_7$Leu(represented by a simulation in Figure 3.3a), which consists primarily of an axially symmetric Pake-type powder pattern with an effective quadrupolar coupling constant(QCC) of ~50 kHz, corresponding to the six deuterons of the rapidly rotating $\delta_1$ and $\delta_2$ $CD_3$ groups. The γ-methine deuteron generates a weaker pattern with a QCC of ~170 kHz having low experimental sensitivity(not shown in Figure 3.3a).

Figure 3.2c represents PS-bound LKα14 deuterated at L8, so any difference between Figure 3.2c and the spectrum of unbound LKα14 in Figure 3.2a is assumed to be due to the influence of the PS surface on the leucyl side chain dynamics. Similarly, the spectral pattern variation observed in Figure 3.2b-e is presumably due to variation in the dynamics as a function of side chain proximity to the PS surface. Finally, as Figure 3.2f represents the spectrum of LKα14 deuterated at L8 and bound to the surface of a carboxyl-terminated SAM on colloidal gold, the spectral pattern variation in Figures 3.2c and 3.2f is likely due to the differential impact on the leucyl side chain of adsorption onto a nonpolar PS surface versus adsorption onto the polar surface of the SAM.

The dynamics of leucyl side chains has been studied and quantified by Torchia and coworkers[49] in a $^2$H NMR study of helical collagen fibrils with uniformly $^2H_{10}$-labeled L-leucine. The temperature variation of the deuterium line shape was modeled as variation in the rate of a two-site exchange between two conformations of the leucine side chain observed in crystallographic studies of leucine monomer and leucyl peptides[50,51]. To simulate the spectral patterns in Figure 3.2, we similarly assumed here an exchange between the two conformers shown in Figure 3.3b. The site exchange corresponds to an angular change of ~ 110° for the Cβ-Cγ bond axis. The rapid rotational motions of the $CD_3$ groups are treated simply with an effective

QCC. The exchange rate and a priori conformer populations were varied in the simulations. In addition, to account for motion of the peptide chain itself, the Cα-Cβ bond was treated as moving on the surface of a cone.

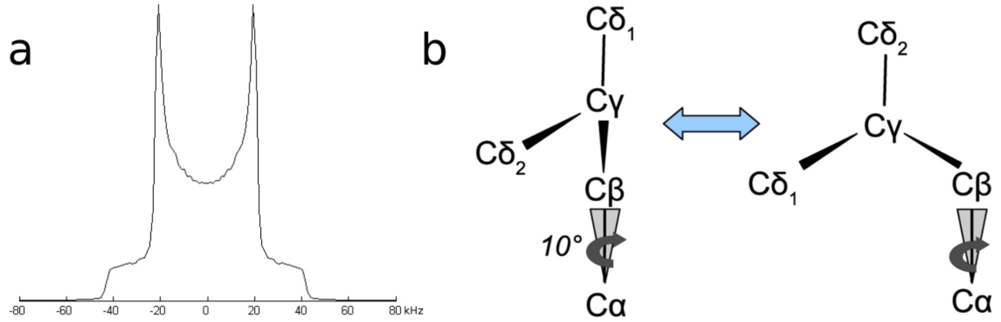

Figure 3.7. Simulation of polycrystalline $d_7$Leu and two-site jump model
(a) Simulation of polycrystalline $d_7$Leu. (b) Two-site jump model with 10° half-angle cone motion used for the simulations.

## 3.3 Simulation Results

Simulation results are shown with superimposed spectral data in Figure 3.2 and in table 3.1. Although Figures 3.2b-e show features of a dynamically induced $\eta=1$ spectral powder pattern, a residual HDO signal limited our ability to exactly simulate the central feature of these spectra.

Table 3.2. Simulation parameters for the spectra shown in Figure 3.2.

| | L5 | L8(PS) | L11 | L14 | L8(SAM) |
|---|---|---|---|---|---|
| $P_1/P_2$ | 4/6 | 4/6 | 4/6 | 3.5/6.5 | 3/7 |
| $k_{ex}$ ($s^{-1}$) | $3x10^5$ | $6\ x10^5$ | $1x10^6$ | $3x10^5$ | $3x10^5$ |
| $k_{cone}$ ($s^{-1}$) | $2x10^3$ | $2x10^3$ | $2x10^3$ | $3x10^3$ | $6x10^3$ |
| $QCC_{eff}$ (kHz) | 49 | 49 | 49 | 51 | 43 |

The simulation results shown in the table indicate that the rate constant for exchange between side chain conformers, $k_{ex}$, is the model parameter that varies most significantly across the series Figure 3.2b-f: $k_{ex}$ is greatest for L8 and L11, whose side chains are located closest to the PS surface, while $k_{ex}$ for L5 and L14 are significantly smaller. There is much less variation in all of the other model parameters for the different leucine sites of LKα14 on PS. Interestingly, $k_{ex}$ for L8 on a carboxyl-terminated SAM surface is identical to those for L5 and L14 and differs from that for L8 on PS by a factor of two.

## 3.4 Combination with SFG Study:

Verification of the peptide orientation on carboxylated surfaces was performed with SFG. Figure 3.4 presents spectra of a monolayer of carboxyl-terminated alkanethiolates (identical to those used in Figure 3.2e) on gold-coated $CaF_2$ windows before and after adsorption of LK peptides.

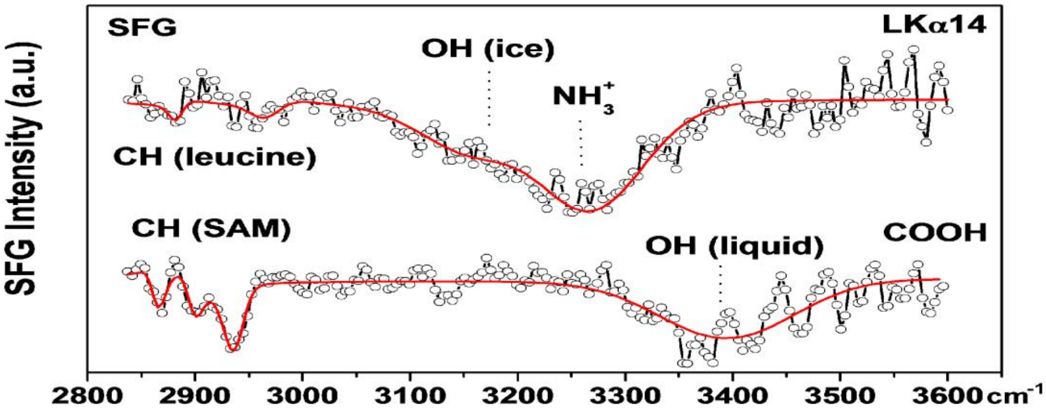

Figure 3.8. SFG spectra of COOH-functionalized gold surfaces alone (lower trace) and after adsorption of LKα14 (upper trace).

The spectrum of the bare SAM surface consists only of the methylene stretching modes at 2866 $cm^{-1}$ and 2933 $cm^{-1}$, with the carboxyl-adjacent methylene unit at 2901 $cm^{-1}$, and loosely bound water near 3400 $cm^{-1}$.[52,53] Upon peptide adsorption, weak $CH_3$ resonances related to leucine side chains appear (2961 $cm^{-1}$ and 2880 $cm^{-1}$). These modes are phase shifted by 180° with respect to the gold background (appearing as a dip in the spectrum), showing that the leucines are pointing away from the surface.[54,55] A band near 3200 $cm^{-1}$ is related to tetrahedrally coordinated water molecules.[52,53] We assign the feature near 3265 cm$^{-1}$ to ordered lysine NH$^{3+}$ groups bound to the SAM substrate.

## 3.5 Conclusion

This study indicates that dynamics of the isopropyl moiety of the leucine side chain is extremely sensitive to surface proximity and surface functionalization. The factor of 2–3 change in $k_{ex}$ observed for the L8/L11 versus L5/L14 sites in LKα14 on PS surfaces is observed in collagen leucine lineshapes only as a result of a 40°C change in temperature. The L8(SAM) data and SFG orientation data mutually demonstrate that a change in surface functionalization in turn changes the peptide orientation and consequently the surface proximities of amino acid side chains. The collagen study found the existence of a mobile interface between individual helical protein components of the fibers[56-58], characterized in part by quantifying the dynamics of leucine side chains as a function of temperature. This study has used multiple, complementary spectroscopies to observe a similarly mobile interface between a peptide structure and bulk surfaces, with mobility quantifiable in terms of NMR exchange dynamics of leucine side chains with varying surface proximities, and suggests that the combination of NMR and SFG on such systems can provide significantly more information than either alone.

# Chapter IV

## Deuterium Magic Angle Spinning NMR Used to Study the Dynamics of Peptides Adsorbed onto Polystyrene and Functionalized Polystyrene Surfaces

### Abstract

LKα14 is a 14 amino acid peptide with a periodic sequence of leucine and lysine residues consistent with an amphipathic α-helix. This "hydrophobic periodicity" has been found to result in an α-helical secondary structure at air-water interfaces and on both polar and non-polar solid polymer surfaces. In this paper the dynamics of LKα14 peptides, selectively deuterated at a single leucine and adsorbed onto polystyrene and carboxylated polystyrene beads, are studied using $^2$H Magic Angle Spinning (MAS) solid state NMR over a 100 degree temperature range. We first demonstrate the sensitivity enhancement possible with $^2$H MAS techniques, which in turn enables us to obtain high quality $^2$H NMR spectra for selectively deuterated peptides adsorbed onto solid polymer surfaces. An extensive literature shows that the dynamics of leucine side chains are sensitive to the local structural environment of the protein. Therefore the degree to which the dynamics of leucine side chains and the backbone of the peptide LKα14 are influenced by surface proximity and surface chemistry is studied as a function of temperature with $^2$H MAS NMR. It is found that the dynamics of the leucine side chains in LKα14 depend strongly upon the orientation of the polymer on the surface, which in turn depends on whether the LKα14 peptide adsorbs onto a polar or non-polar surface. $^2$H MAS line shapes therefore permit probes of surface orientation over a wide temperature range.

## 4.1 Introduction

Deuterium solid state nuclear magnetic resonance ($^{2}$H NMR) is a versatile, non-perturbing, quantitative probe of biopolymer dynamics over a broad range of motional rates. The solid state $^{2}$H NMR spectrum is dominated by the interaction of the electric quadrupole moment of the deuterium nucleus with surrounding electric field gradients. The magnitude of this interaction is quantified by the deuterium quadrupolar coupling constant (i.e. QCC=$\frac{3e^{2}qQ}{4\hbar}$), which is on the order of 170 kHz for deuterons in sp$^{3}$ hybridized carbon-deuterium bonds.[59] Given the magnitude of the anisotropy of the deuterium quadrupolar interaction, the dynamic regimes probed by $^{2}$H NMR are by convention divided into: 1) very fast motions (correlation time $\tau_{c} < 100\,\mathrm{ns}$) which induce relaxation; 2) fast motions ($\tau_{c} < 10\,\mu\mathrm{s}$) which partially average the anisotropy of the quadrupolar interaction; 3) intermediate motions with rates on the order of the anisotropy of the quadrupolar interaction ($10\,\mu\mathrm{s} < \tau_{c} < 1\,\mathrm{ms}$) which dynamically perturb $^{2}$H NMR line shapes; 4) slow motions ($1\,ms < \tau_{c}$) which are probed by studies of the rate of decay of $^{2}$H spin alignment.[60]

$^{2}$H NMR line shapes obtained with a quadrupolar echo pulse sequence are extremely sensitive to dynamic amplitudes and dynamic rates in the $10^{4}$–$10^{7}$ Hz range,[61-64] whereas spin-lattice relaxation studies can probe very fast motions. Although quadrupolar echo line shapes and partially relaxed line shapes have been used to quantify molecular samples with high deuterium enrichment levels, $^{2}$H NMR has practical limitations. For example, the relatively large anisotropy of the quadrupolar interaction results in very broad, heterogeneous line shapes for polycrystalline samples, which together with the small magnetic moment of the deuterium nucleus results in low sensitivity. For this reason, application of $^{2}$H NMR to magnetically dilute samples, including selectively deuterated proteins and nucleic acids, is challenging. In composite systems consisting, for example, of selectively deuterated proteins associated with lipid bilayers[65] or adsorbed onto material surfaces,[66] further dilution of the deuterated sample content occurs and the application of $^2$H NMR spectroscopy becomes even more challenging.

Deuterium Magic Angle Spinning ($^2$H MAS) NMR has emerged in recent years as a viable alternative to static quadrupolar echo spectroscopy.[22,67-69] Spinning a deuterated sample rapidly around an axis that is oriented at 54.74° (i.e., the magic angle) relative to the direction of the static external magnetic field, averages the $^2$H NMR solid state line shape into an isotropic resonance and side bands separated by intervals of the spinning frequency $\nu_R$, where typically $1\,\text{kHz} < \nu_R < 20\,\text{kHz}$. Because the integrated intensity of the $^2$H NMR spectrum is concentrated into a small number of resonances in a MAS experiment, sensitivity enhancements of 20-30 are easily achievable. This feature makes $^2$H MAS NMR a potentially powerful approach for studying the dynamics of very small quantities of selectively deuterated biopolymers adsorbed onto biomaterial surfaces.

This paper has two purposes. First, we describe the application of $^2$H MAS NMR to the study of the dynamics of a selectively deuterated peptide adsorbed onto a nonpolar polystyrene surface and a polar surface obtained by carboxylating polystyrene. Second, using an in-house program KLDMAS to simulate dynamically averaged $^2$H NMR line shapes, we present a quantitative analysis of these side chain motions. The degree to which peptide dynamics reflect the orientation of the surface-adsorbed peptide on differently functionalized polymer surfaces is investigated over a 100 degree temperature range.

We chose for study the 14-amino acid "LK" peptide composed of alternating periods of leucine (L) and lysine (K) residues,[45] the so-called LKα14 peptide: Ac-LKKLLKL$\underline{\text{L}}$KKLLKL-OH where L-leucine- isopropyl-$^2H_7$ ($d_7$Leu) was incorporated at the L8 position. See Figure 4.1a. Degrado and Lear first demonstrated that short peptides possessing "hydrophobic periodicity" (i.e., matching that of amphiphilic α-helices) adopt a structure and orientation at hydrophobic surfaces, to sequester hydrophobic residues in a favorable environment rather than remaining in an unfolded state, as observed in aqueous solution. Previously, we have used $^{13}$C dipolar recoupling solid state NMR to quantify the local α-helical structure of selectively $^{13}$C labeled LKα14 peptide adsorbed onto polystyrene (PS) bead surfaces.[46] Structured as an α helix on PS bead surfaces, LKα14 is amphipathic, with one half of the cylinder surface dominated by non-polar leucine side chains and the other half dominated by positively-charged lysine side chains. See Figure 4.1b. The interactions of LKα14 with PS and silica surfaces have been studied also by Somorjai and coworkers,[47,48] who used sum frequency generation (SFG) vibrational spectroscopy to show that LKα14 adsorbs onto PS with the leucine side chains alongside and lysine side chains opposite the surface, while the opposite orientation occurs on negatively charged silica surfaces. In both cases SFG spectroscopy found, as did solid state NMR, that surface-adsorbed LKα14 is structured as an α- helix.

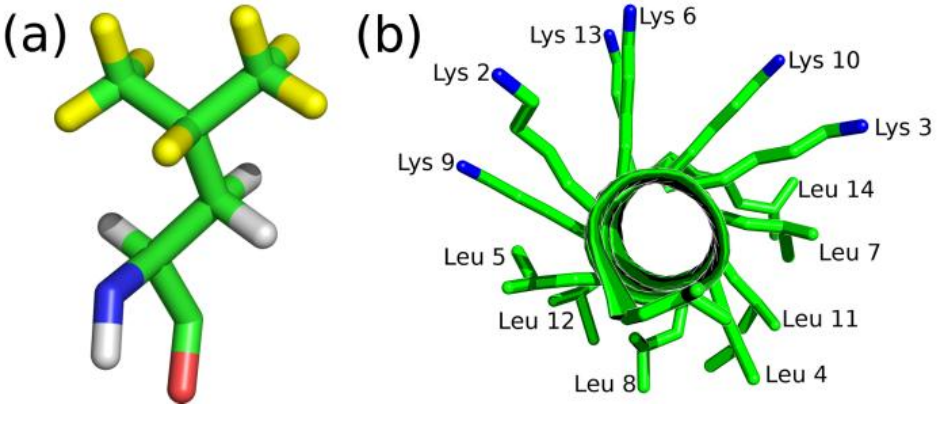

Figure 4.1. Structure of leucine and labeled LKα14
(a) Structure of leucine, with deuterated sites identified in yellow.
(b) Side chain orientations of the residues in LKα14.

We have also used SFG and $^2$H NMR conjointly to study both the leucine side chain dynamics and the surface orientation for LKα14 adsorbed onto PS surfaces and onto colloidal gold particles coated with a self assembled monolayer of carboxylated alkane thiolates.[66,70] In those works, trends in $^2$H NMR static line shapes were shown to be correlated with the orientation of the leucine side chain relative to the PS surface, as determined by SFG. For L8 in particular, SFG studies of LKα14 selectively deuterated at individual leucines and adsorbed onto PS and showed that the $C_\alpha$-$C_\beta$ bond of L8 is nearly parallel to the PS surface normal [48]. The isopropyl group of L8 is therefore very likely in close proximity to the PS surface but more remote from the PSCOOH surface.

Here we apply $^2$H MAS spectroscopic techniques to the study the side chain dynamics of leucyl-peptides adsorbed onto functionalized polymer surfaces as a function of temperature and surface chemistry. Because of its varying proximity to PS and PSCOOH surfaces, we investigate the degree to which $^2$H MAS line shapes isopropyl-deuterated L8 in LKα14 vary in response to a changes in temperature and surface chemistry. In particular the detailed nature of the peptide side chain motions on PS and PSCOOH surfaces, is extracted from an analysis of the $^2$H MAS line shape and spin-lattice relaxation rates over a 100 degree temperature range. The overall intent is to determine the degree to which amino acid side chain dynamics as elucidated by $^2$H MAS NMR are diagnostic of surface orientation and surface proximity. In addition, the degree to which peptide side chain dynamics at a material interface resembles side chain dynamics in other contexts, i.e. in the hydrophobic interior of folded proteins or inserted into lipid bilayers, is discussed. We also briefly describe in-house software LKDMAS, developed for the purpose of simulating dynamically modulated $^2$H MAS line shapes.

## 4.2 Materials and Methods

**Peptide Synthesis and Characterization**. L-leucine, isopropyl-$^{2}H_{7}$ (99% atom $^{2}H$) was purchased from Cambridge Isotope Laboratories (Andover, MA) and Fmoc-protected using standard protocols.[71] Natural abundance amino acids were purchased in protected form from Novabiochem and used directly. Peptides were synthesized on a Rainin PS3 automated synthesizer using Wang resin and NMP solvent. After resin cleavage and lyophilization, sample purity was confirmed with mass spectroscopy. The peptide did not require further purification.

**Peptide Adsorption to polystyrene and NMR sample preparation**. Peptides were adsorbed to polystyrene by adding 1.55 mg of peptide (in aqueous solution at 5.0 mg/ml) to 3 ml of an aqueous suspension of 1.0 μm diameter polystyrene beads (Polysciences) and 40 ml of 0.13× PBS buffer at pH 7.0. The mixture was stirred gently at room temperature for 4 hours, then centrifuged for 2 hours at 3000×*g*. The supernatant was decanted off, and the pellet was again suspended in ca. 1 ml of deuterium-depleted water, and centrifuged at 10,000×*g* for 10 minutes. This washing step was repeated twice more, following which the final resuspension was flash-frozen and lyophilized for 5 days. UV analysis of the supernatant indicated 85-90% peptide binding.

**$^{2}$H NMR Experiments**. All static quadrupolar echo experiments were performed at 17.6 Tesla field (115.14 MHz deuterium Larmor frequency), using a homebuilt single-channel static deuterium probe with a Bruker Avance II spectrometer and a 90° pulse time of 2.65 μs. Samples consisted of 40 mg of bead/peptide powder contained in a Kel-F sample holder. All measurements were made at room temperature (~23°C). A quadrupole echo pulse sequence,[72] where the second half of the echo signal was acquired and Fourier-transformed following left-shift of all time-domain datasets to their respective echo maxima, was used to obtain line shapes.

Quadrupole echo experiments used eight-step phase cycling, with an echo delay of 40 μs. Typical spectra resulted from acquisition of 360,000–400,000 transients at a recycle delay of 0.35 s. Lineshapes were minimally processed with 1 kHz line broadening and phase correction only.

MAS line shapes were acquired at a deuterium Larmor frequency of 61.38 MHz, using a Varian T3 MAS probe, 4mm sample rotors packed with 30 mg of sample, and a homebuilt spectrometer. These experiments employed a single $^2$H 90° pulse width of 3.2 μs. Spectra were acquired at spinning speeds of 4000 Hz. LK$\alpha$14 samples adsorbed onto polystyrene (PS) or carboxylated polystyrene (PSCOOH) surfaces were signal-averaged for 530,000 scans. Inversion recovery spectra were acquired from the same sample rotors at a frequency of 76.75 MHz, using a 6.0 μs 180° inversion pulse followed by a variable delay and a 3.0 μs 90° quadrupolar echo pulse. Samples were spun at 5000 Hz and signal-averaged with 120,000 scans per time point. After left-shifting to the peak of the first echo, FIDs were Fourier transformed and phase corrected without further processing.

## 4.3 Calculations

**$^2$H Static and MAS Line Shape Simulations.** Quadrupolar echo spectra were simulated numerically with MXET1.[46] $^2$H NMR MAS spectra and inversion-recovery experiments were simulated with an in-house program, KLDMAS. The theoretical approach used by KLDMAS has been described in Chapter II.

## 4.4 Results and Analysis

**Static and MAS Line Shapes*:*** As a basis for comparison to surface-bound peptide data, and to determine the degree to which both static and MAS spectra can be fit to the same dynamic model, we first performed a comparative study of the $^2$H quadrupolar echo and $^2$H MAS spectra of unbound LK$\alpha$14. In Figure 4.2a,b is shown the experimental $^2$H quadrupolar echo spectrum of unbound LK$\alpha$14 with Leu-d$_7$ incorporated at position L8, and acquired at T=20°C. The static line shape in Figure 4.2a,b is narrowed as a result of the rapid rotation of the CD$_3$ groups. Because of its fast rate, this physical motion can be accurately treated in line shape simulations as a "pre-averaged" EFG tensor, where the "effective" quadrupolar coupling constant is reduced from about 170 kHz to 50 kHz or less. There is also a contribution to the line shape arising from the $\gamma$-methine deuteron ($^2$H$_\gamma$) of the isopropyl group, which retains a QCC of 170 kHz. The larger anisotropy of the $\gamma$-methine deuteron together with the fact that the methyl to methine deuteron ratio is 6:1 means the $^2$H static spectrum will be largely dominated by the methyl deuterons. The central portion of the $\gamma$-methine deuteron spectrum appears as a rise in the base line in Figure 4.2a,b.

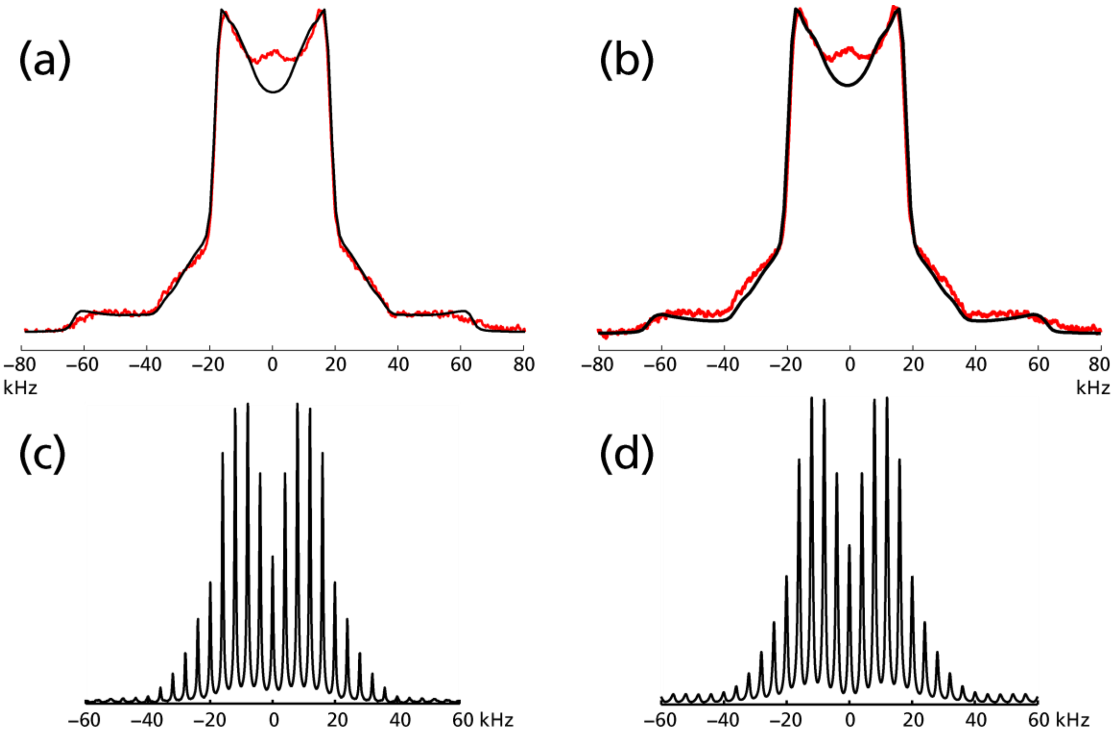

Figure 4.2. Experimental $^2$H line shapes and simulations for LK$\alpha$14
(a, b): Red lines: Experimental $^2$H static NMR line shapes (identical in both); black lines: simulation fits using (a) parameter set 1 and (b) set 2. (c): MAS line shape of unbound LK$\alpha$14, deuterated at Leu8. (d): Simulation of data in (c) using parameter set 1.

If the only dynamics present in the isopropyl group of L8 were the fast $CD_3$ rotational motion, the $^2H$ spectrum of the $CD_3$ groups of LK$\alpha$14 would have the appearance of a narrowed Pake doublet.[4] The deviation of the LK$\alpha$14 $^2H$ NMR spectrum from the Pake doublet line shape indicates presence of additional motions of the leucine side chain as well as possible motions of the peptide backbone at intermediate time scales. To account for the other features in Figure 4.2a we must consider explicit models for leucine side chain motions.

$^2H$ NMR has been used to study leucine side chain dynamics in protein fibrils,[49] hydrated solid proteins,[18,73,74] and peptides and proteins embedded in lipid bilayers.[75] Combining the three rotational isomers for each of the $C_\alpha$-$C_\beta$ and $C_\beta$-$C_\gamma$ bonds, there are nine side chain conformers. Discounting other side chain motions, bond rotational motions conspire to direct the $C_\gamma$-$C_\delta$ bond in four directions defined by the corners of a tetrahedron.[18] Previous models for the side chain motion typically include exchanges between some or all of these conformers. For example, Batchelder et al's early $^2H$ NMR study of uniformly leucine-deuterated helical collagen fibrils[49] used a two-conformer model selecting the orientations observed to be dominant in leucyl-peptide crystal structures: $tg^+$ and $g^-t$, where $g^+$, $g^-$, and $t$ indicate the gauche +, gauche –, and trans rotational isomers of the $C_\alpha$–$C_\beta$ and $C_\beta$–$C_\gamma$ bonds, respectively.[50,51] Using this model and assuming equal a priori populations Batchelder et al interpreted changes in the $^2H$ line shape with sample temperature as resulting from changes in the rate of exchange. Separate motion of the peptide backbone was treated by Lorigan in a study of selectively methyl-deuterated phospholamban,[75] a 52-residue transmembrane protein, by incorporating an additional two-site motion around the $C_\beta$-$C_\gamma$ bond axis, tilting the methyl groups at a 75° and jumping in increments of 109.5°. A recent study of the chicken villin headpiece domain HP-36 with a single methyl-deuterated leucine conducted by Vugmeyster et al.[18] successfully extended both approaches:

including all four unique conformers with exchange rates in an adjustable ratio x:1:1:1, and generalizing the backbone motion as a diffusion along an arc at a fixed 70.5° tilt.

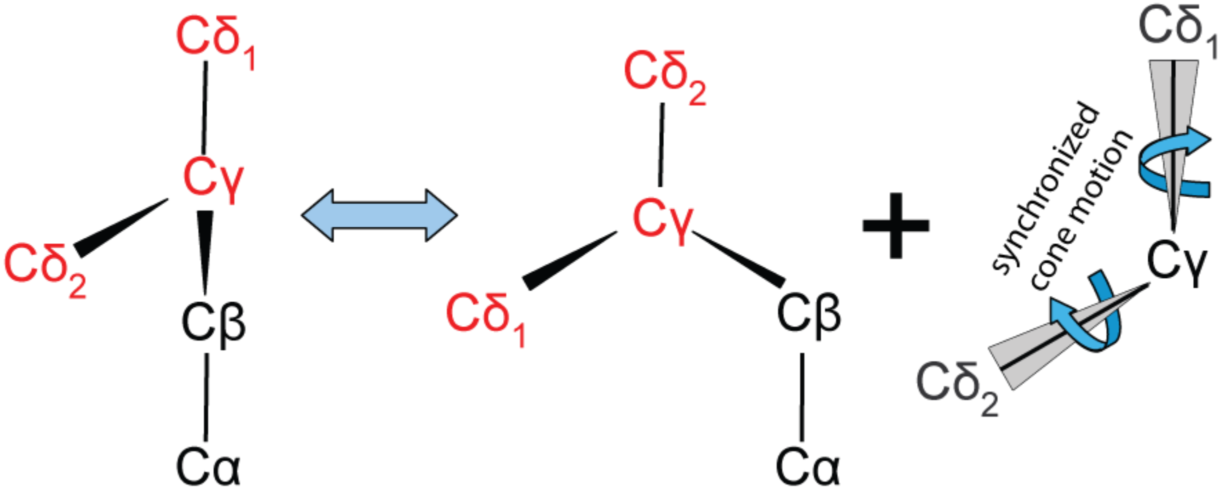

Figure 4. 3. Dynamic model used for $^{2}$H NMR simulations.

To fit the static $^{2}$H quadrupolar echo and the $^{2}$H MAS spectra for free (i.e. unbound) LKα14 deuterated at L8 shown in Figure 2, we constructed a hybrid model, which incorporates elements derived from several models of leucine side chain motion, discussed above. As shown in Figure 4.3, for the purpose of calculating the MAS line shape, the rapid rotational motions of the $CD_3$ groups are treated simply with an effective QCC. Rotation of the methyl group is explicitly included as a three site jump in later calculations of inversion-recovery MAS line shapes. Following Batchelder et al, we use a two site exchange between the $tg^{+}$ and $g^{-}t$ side chain conformers, corresponding to an angular change of about 109.5° for the $C_{\gamma}$–$C_{\delta}$ bond axis. But as in Vugmeyster et al. we assumed exchange occurs between side chain conformers with unequal a priori populations, i.e. essentially a x:y:0:0 model, where y=1−x. Therefore the equilibrium site population ratio and thus the ratio of the forward and reverse exchange rate constants $k_{12}$ and $k_{21}$, is an adjustable parameter. These parameters are related by the equilibrium condition:

$$k_{12}\mathrm{p}_2^{\mathrm{eq}} = k_{21}\mathrm{p}_1^{\mathrm{eq}} \tag{4.1}$$

Also as in Vugmeyster et al. we rendered the effect of peptide backbone motions as a diffusive motion of the $C_\gamma$–$C_\delta$ bonds along the arc of a cone. Adjustable parameters for this aspect of the model include the cone half angle, and the correlation time associated with the diffusive motion of the $C_\gamma$–$C_\delta$ bonds on the cone arc.

Given that the $CD_3$ rotation is treated in line shape calculations with an effective or pre-averaged QCC, the motional model used in line shape calculations is explicitly described with two dynamic axes, one of which accounts for the exchange motions of the leucine side chain and the other accounts for backbone motions of the protein which move the entire amino acid residue. The matrix elements $\omega_\pm(t)$ assume the form:

$$\begin{aligned}\omega_\pm^{jk}(t) &= \pm\left\langle\frac{3e^2qQ}{4\hbar}\right\rangle \sum_{a,b,c=-2}^{2} D_{0a}^{(2)}(\Omega_{LM}(t))*D_{ab}^{(2)}(\Omega_{MC})*D_{bc}^{(2)}(\Omega_{CI}^{k})*D_{c0}^{(2)}(\Omega_{IP}^{j})\\ &= \pm\left\langle\frac{3e^2qQ}{4\hbar}\right\rangle \sum_{a,b,c=-2}^{2} D_{0a}^{(2)}(0,\theta_{magic},\omega_r t)D_{ab}^{(2)}(\alpha,\beta,\gamma)D_{bc}^{(2)}(\phi_1^k,\theta_1,\psi_1)D_{c0}^{(2)}(\phi_2^j,\theta_2,\psi_2=0)\end{aligned} \tag{4.2}$$

The brackets < > in equation (4.2) indicate pre-averaging of the quadrupolar coupling constant as a result of the fast methyl group rotation, which as mentioned above effectively reduces the QCC from 170 kHz to about 50 kHz. The solid angle $\Omega_{IP}^{j} = (\phi_2^j, \theta_2, \psi_2)$ relates the principal axis system of the EFG tensor (P) to the I frame, which is associated with the two-fold motion of the $C_\gamma - C_\delta$ bonds, with $\theta_1$ in turn describing the $C_\gamma - C_\delta - D$ angle. The angles

$\phi_1^j = 2\pi/3*(j-1)$ and $\psi_1^j = 2\pi/3*(j-1)$ represent the side chain conformer site being occupied, where $j$={1,2} indicates the site. The solid angle $\Omega_{CI}^k = (\phi_1^k, \theta_1, \psi_1)$ relates frame I to the crystal frame C, which is fixed to the amino acid framework and within which the local molecular motion is defined. This motion is simulated as a four site jump of the $C_\gamma - C_\delta$ bonds on the surface of a cone of half angle $\theta_2$ where the site on the cone is specified by $\phi_2^k = \frac{\pi}{2}(k-1)$, $k$={1,2,3,4}. The $z$ axis of the P frame is assumed to be co-linear with the $C_\delta - D$ bond axis and the EFG tensor is assumed to be axial, which means $\psi_2$ may be set to zero.

Table 4.1 summarizes two model parameter sets used to obtain static quadrupolar echo line shape simulations with MXET1 and MAS line shape simulations with KLDMAS, based on the dynamic model shown in Figure 4.3. Parameter set 1 was used to obtain the simulation of the static quadrupolar echo spectrum shown in Figure 4.2a superimposed on the experimental spectrum, and the MAS spectral simulation shown in Figure 4.2c. In this parameter set, the population ratio between the two side chain rotational isomers is 0.2/0.8=1/4. The kinetic rate constant $k_{12}$ associated with this site exchange is $3\times10^6$ s$^{-1}$. The constant $k_{21}$ can be computed given $k_{12}$ and the population ratio using equation (4.1). As mentioned above, the isopropyl group also undergoes a slow gyration, with the $C_\gamma$–$C_{\delta1,2}$ bonds moving over the surface of a cone of half angle 35 degrees, modeled as a four site jump, with equal *a priori* probabilities and a site-to-site jump rate constant $k_{\text{cone}}$ of 800 Hz , which is inversely related to the correlation time for diffusion on the cone. The ratio of the γ-methine spectral intensity to the total methyl intensity is about 0.04. The actual molar ratio is about 0.16 and the disparity is attributed to a longer γ-methine $T_1$ which attenuates the methine signal relative to the $CD_3$ signal upon extensive signal averaging.

Table 4.1: Parameter sets 1 and 2 used to fit the static $^2H$ NMR spectra of unbound LK$\alpha$14 deuterated on the isopropyl group of L8, shown in Figures 4.3a and 4.3b, respectively. Parameter set 1 was used to fit the experimental $^2H$ MAS experimental spectrum in Figure 4.2c. Figure 4.2d is the MAS simulation using parameter set 1. See text for description of model.

| Parameter | Static Parameter Set 1 | Static Parameter Set 2 |
|---|---|---|
| Population ratio $p_1/p_2$ | 0.2/0.8 | 0.2/0.8 |
| $k_{12}$ (s$^{-1}$) | $3\times10^6$ | $8\times10^5$ |
| $k_{\text{cone}}$ (s$^{-1}$) | 800 | 800 |
| Cone Half Angle (°) | 35 | 25 |
| $<QCC>_{\text{eff}}$ (kHz) | 49.5 | 50.5 |
| % $^2H_\gamma$ | 4 | 6 |

Agreement between the MAS simulation in Figure 4.2d and MAS data shown in Figure 4.2c is excellent using parameter set 1, but the simulated $^2H$ static quadrupolar echo spectrum obtained with this parameter set and shown in Figure 4.2a, does not fit well to the central portion of the experimental spectrum. This is an especially difficult region of the $^2H$ NMR spectrum to fit because residual HDO adsorbed onto the peptide will contribute to the experimental spectrum in this region. If the small peak in the center of the spectrum in Figure 4.2a has a contribution from HDO, the simulation would not represent its presence at all. If the parameter set is adjusted to better match the central intensity of the quadrupolar echo spectrum, a best fit is obtained with parameter set 2. The resulting simulation appears in Figure 4.2b superimposed on the experimental spectrum. The two parameter sets have identical population ratios ($p_1^{eq}/p_2^{eq}=1/4$) and rate constants for cone motion $k_{\text{cone}}$. The sets show small differences in the effective quadrupolar coupling constants and the cone half angles, and a moderate difference in the side chain exchange rate $k_{12}$. Although the simulation in Figure 4.2b shows improved agreement in the central portion of the spectrum, the agreement with data is still not perfect and the fit to the outer portions of the spectrum is compromised. Because we have far more confidence in the data in outer portions of the spectrum where there is less interference from residual HDO, parameter set 1 is a better fit to the quadrupolar echo data and it is a best fit to the MAS data.

Next a $^2$H MAS study was performed on the L8-deuterated LKα14 peptide adsorbed onto polystyrene (PS) and carboxylated polystyrene (PSCOOH) beads. $^2$H MAS line shapes were obtained at temperatures of −40, −20, 0, 20, 40, and 60°C, enabling a study of leucine side chain dynamics on PS and PSCOOH surfaces over a 100 degree temperature range. Representative experimental results, superimposed simulations, and the difference between simulation and experimental results are shown in Figure 4.4 for LKα14 on: PS at T=20°C (4a), PSCOOH at T=20°C (4b), PS at T=−20°C (4c), and PSCOOH at T=−20°C (4d). Data and simulation sets for all other temperatures are provided as supplementary information. All MAS line shape simulations were obtained using the model shown in Figure 4.2.

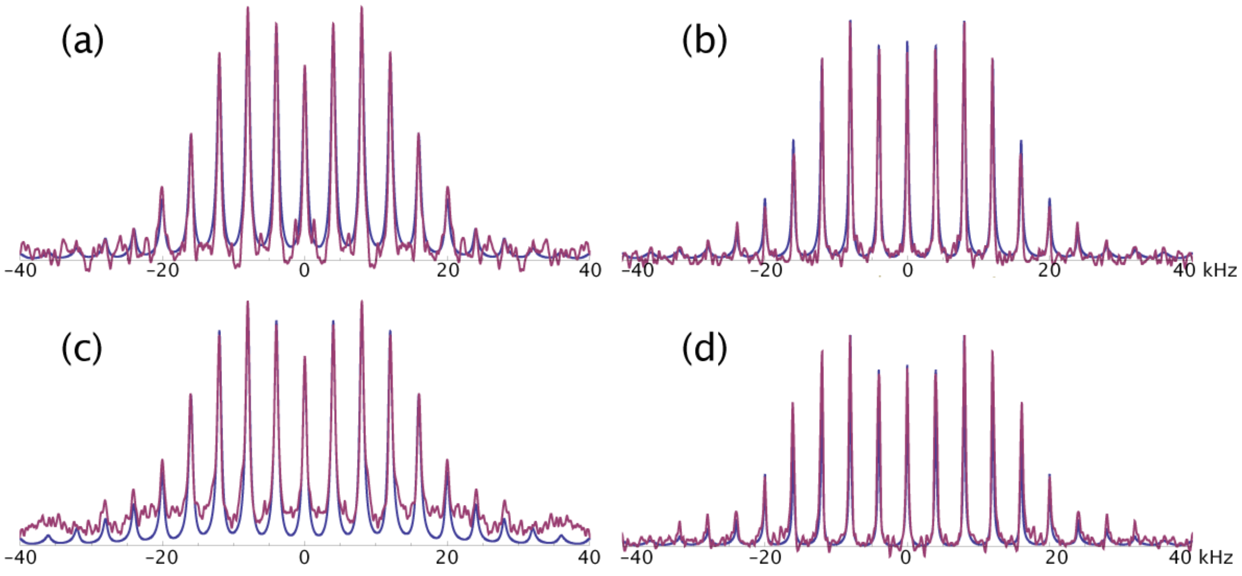

Figure 4.4. MAS spinning line shapes (purple) and simulation fits (blue) for the L8 peptide at different temperatures and on different surfaces.
(a) 20°C on PS (b) 20°C on PSCOOH (c) –20°C on PS (d) –20°C on PSCOOH

Table 4.2. Simulation parameters for all LK NMR experiments.

| Surface | Temperature(°C) | $QCC_{eff}$ (kHz) | $k_{cone}$ (Hz) | $p_1 : p_2$ |
|---|---|---|---|---|
| PS | −40 | 49 | 500 | 0.38 : 0.62 |
| PS | −20 | 48 | 500 | 0.38 : 0.62 |
| PS | 0 | 48 | 500 | 0.36 : 0.64 |
| PS | 20 | 46 | 600 | 0.36 : 0.64 |
| PS | 40 | 44 | 600 | 0.32 : 0.68 |
| PS | 60 | 45 | 1200 | 0.32 : 0.68 |
| PSCOOH | −40 | 49 | 500 | 0.23 : 0.77 |
| PSCOOH | −20 | 49 | 500 | 0.24 : 0.76 |
| PSCOOH | 0 | 48 | 500 | 0.26 : 0.74 |
| PSCOOH | 20 | 47 | 500 | 0.27 : 0.73 |
| PSCOOH | 40 | 44 | 500 | 0.32 : 0.68 |
| PSCOOH | 60 | 45 | 800 | 0.38 : 0.62 |
| Unbound | 20 | 49 | 800 | 0.20 : 0.80 |

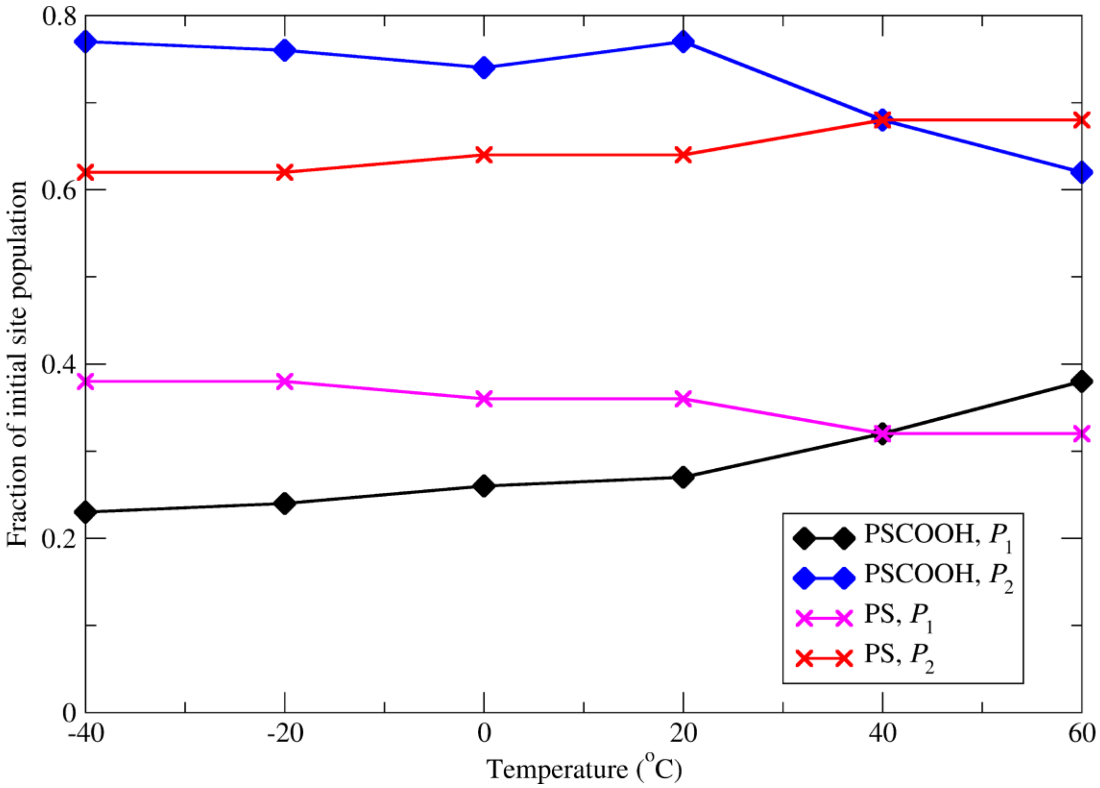

Figure 4.5. Initial site populations $p_1$ and $p_2$ as a function of temperature.

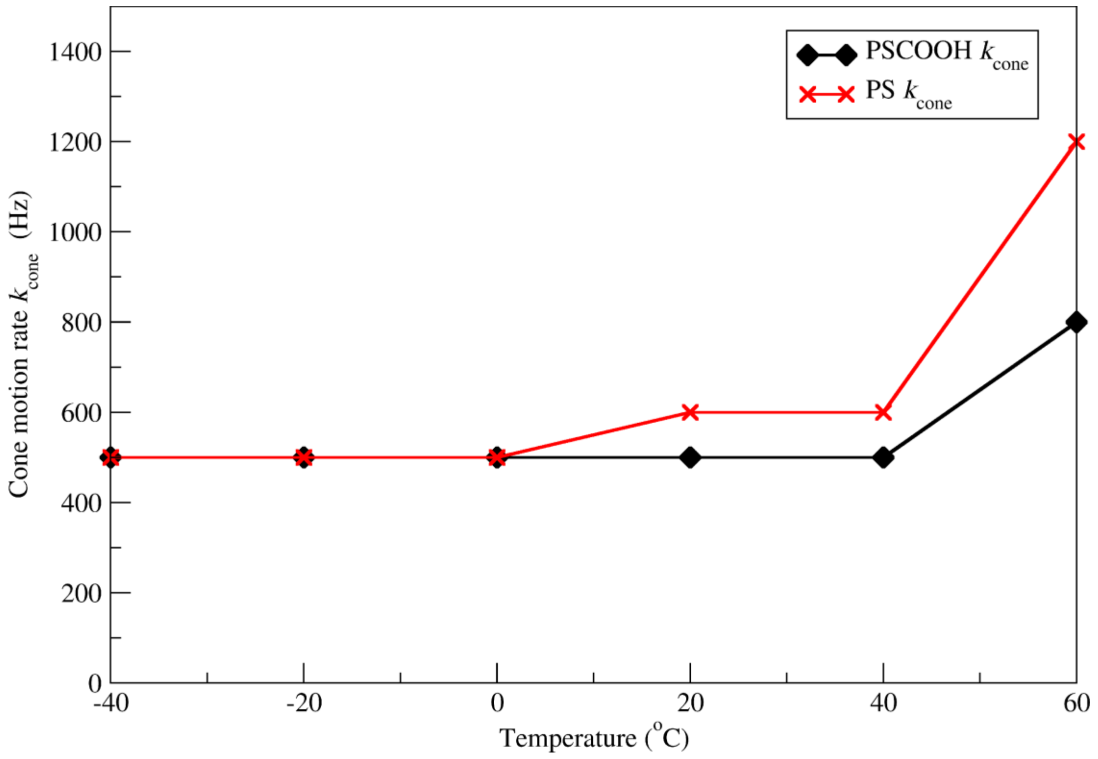

Figure 4.6. Cone motion rate $k_{cone}$ as a function of temperature.

Trends in simulation parameters with temperature are shown in Figures 4.5 and 4.6 and Table 4.2. As shown in Figure 4.5, the site populations $p_1$ and $p_2$ which are associated with the exchange between the two dominant leucine side chain conformers, changed significantly throughout the temperature range studied on both PS and PSCOOH surfaces. Although the simulated line shapes were sensitive to the population ratio, they were substantially insensitive to the value of $k_{12}$ over at least three orders of magnitude, which was therefore maintained at $3\times10^6$ $s^{-1}$ for all fits. On PSCOOH surfaces at the lowest available temperature, T=−40°C, the a priori population ratio is $\frac{p_1^{eq}}{p_2^{eq}} \approx 3$. At ambient temperature (i.e. T=20°C), $\frac{p_1^{eq}}{p_2^{eq}}$ has decreased to ~2.5 on PSCOOH. This indicates the a priori populations of the dominant side chain conformers are somewhat less disparate in LKα14 bound to PSCOOH than in free LKα14 at ambient temperature, where according to Table 1, $\frac{p_1^{eq}}{p_2^{eq}} \approx 4$. As temperature increases, the difference between the site populations further decreases; $\frac{p_1^{eq}}{p_2^{eq}}$ is about 1.6 at T=60°C.

On PS surfaces the *a priori* populations are far less disparate than on PSCOOH for most of the temperature range of the study. For example, at T=−40°C, the population ratio on PS is $\frac{p_1^{eq}}{p_2^{eq}} \approx 1.6$ compared to PSCOOH where it is about 3. But the most significant difference between side chain dynamics on PSCOOH versus PS is that whereas the population ratio decreases with temperature between −40°C and 60°C for PSCOOH, for PS it remains largely unchanged from −40°C and 20°C, but then increases to about 2.0 at T=60°C, which is slightly larger than the ratio of 1.6 on PSCOOH at the same temperature. The divergence of a priori population with increasing temperature indicates that the dynamics cannot be interpreted in terms of a conformational exchange in a constant potential where the site populations are governed by $\frac{p_1^{eq}}{p_2^{eq}} = e^{-\Delta E/kT}$, where $\Delta E = E_2 - E_1$ is the difference between the site energies. This issue will be discussed further below.

Trends in other dynamic parameters are similar for the two surfaces over most of the temperature range of the study. Table 4.2 shows that on both surfaces, the effective quadrupolar coupling constants diminishes slightly from around 49 kHz at T=−40°C to 45 kHz at T=60°C. This trend possibly indicates the onset of additional fast, small amplitude motions as the temperature increases. The rate of diffusive motion of the peptide backbone on PS and PSCOOH is only about 500 Hz at temperatures below 0°C and thus makes only a minor contribution to the line shape at lower temperatures. Starting at T=0°C the peptide motion on PS increases rapidly to over 1 kHz at T=60°C, whereas the rate of peptide motion remains constant on PSCOOH until T=60°C where it increases slightly to 800 Hz.

MAS inversion recovery experiments were conducted on both surfaces at temperatures of −40, 20, and 50°C. The results for the recovery time $T_1$ are presented in Table 4.3.

Table 4.3: Inversion recovery times as a function of temperature for L8-deuterated LKα14 on PS and PSCOOH surfaces.

| Temperature (°C) | $T_1$ on PS (ms) | $T_1$ on PSCOOH (ms) |
|---|---|---|
| −40 | 24.8 ± 4.7 | 29.9 ± 3.3 |
| 20 | 54.7 ± 11.8 | 51.6 ± 8.0 |
| 50 | 77.6 ± 7.8 | 70.3 ± 4.6 |

The recovery time reaches a minimum when the rate constant for the correlation time, $R=1/\tau_c$, is equal to the Larmor frequency $\omega_R$. In this case, $T_1$ is increasing with temperature, putting this system well above the minimum $T_1$ at the measured temperatures, i.e. $R>> \omega_R$. In turn, this indicates that the fast motion of the methyl group rotation ($R_{CH3}$~$10^9$-$10^{10}$ Hz) dominates the relaxation mechanism. Relaxation times on both surfaces are equivalent to within error, which is consistent with the above line shape analysis that identifies surface effects primarily from the slower conformational changes that are not observed in the $T_1$.

## 4.5 Discussion

Sum frequency generation (SFG) vibrational spectroscopic studies of the LKα14 peptide system adsorbed onto planar PS indicates LKα14 adsorbs with the leucine face close to the PS surface.[47,48] Similar SFG studies of LKα14 adsorbed onto carboxylated SAMs on planar gold surfaces indicate the leucine face is oriented away from the carboxylated surface.[76] Static $^2$H NMR line shape studies conducted at ambient temperature indicated that the primary impact of surface orientation is perturbation of the motion of the peptide main chain, which is rendered in our analysis as a diffusive cone motion of the entire leucine side chain. Specific motions internal to the leucine side chain itself (i.e. exchange between side chain conformers) vary at ambient temperature to a much lesser extent with surface orientation[48]; by contrast, static and MAS $^2$H NMR studies reveal site-specific heterogenenity in both peptides[66,70,] and porous bulk surfaces[77]. The present study seeks to further explore the fundamental origins of the surface dependence of the $^2$H NMR line shape by specifically focusing upon the dependence of the $^2$H MAS line shape of the $CD_3$ groups of L8 in LK$\alpha$14 as a function of temperature and surface chemistry.

Ambient and physiological temperature (i.e. 30-40°C) studies of LK$\alpha$14 on PS and PSCOOH do not show a great variation in the $p_1/p_2$ ratio as a function of surface orientation. This fact is evident in Figure 4.5, which shows that the $p_1$ and $p_2$ curves for LK$\alpha$14 on PS and PSCOOH intersect near 40°C. What is clear in Figure 4.5 is the opposing trends for $p_1$ or $p_2$ versus temperature for the two surfaces. For LK$\alpha$14 on PSCOOH, where the L8 side chain is directly opposite the surface, the a priori site populations converge as the temperature increases, whereas the same parameters diverge apparently for LK$\alpha$14 on PS. The general dynamic trends with temperature for L8 on PSCOOH are observed in other leucyl peptides, in particular the $^2$H NMR study of the villin headpiece protein,[18] with increasing temperature correlated to a convergence in the initial site populations consistent with a straightforward Boltzmann population distribution, $\frac{p_1}{p_2} = \exp\left(-\frac{E_1 - E_2}{kT}\right)$. This suggests a typical dynamic environment without unusual hindrances, as expected if the side chains are pointed away from the surface. The population ratio trend on the PS surface, however, remains fairly stable until diverging markedly at higher temperatures, 40-60°C. This indicates an additional physical effect influencing the side chain dynamics at higher temperatures, such as a reorientation of the LK peptide as a whole. It is expected that the van der Waals interaction between the nonpolar leucine side chains and PS surface is weaker than the electrostatic interaction between polar lysine side chain termini and surface-accessible carboxyl groups in the PSCOOH surface. At higher temperatures, the thermal energy of the LK peptide may be sufficient to overcome this binding interaction strength, while remaining more constrained than the completely unbound peptide.

The sensitivity of leucine side chain dynamics to molecular environment is supported by an extensive literature. In particular very sophisticated exploitations of the sensitivity of leucine side chain dynamics to local environment is found in membrane protein studies where subtle aspects of the interaction between the protein and the lipid bilayer environment can be discerned from $^2$H NMR line shapes of methyl-deuterated leucine side chains. For example, the transmembrane segment of phospholamban, which is believed to anchor the protein to the membrane, is rich in leucines. Analysis of $^2$H NMR line shapes acquired for selectively leucine- and alanine-deuterated phospholambam in lipid bilayers, have discerned the degree of insertion into the membrane,[65] helix packing interactions,[78] the mobility of a protein backbone hinge[75] and the impact of single amino acid mutation on protein backbone motions.[79] A recent study of the lung surfactant peptide $KL_4$ by Long et al.[80] inferred from $^2$H NMR spectra of selectively deuterated leucines the partitioning and orientation of $KL_4$ in DPPC/POPG and POPC/POPG phospholipid bilayers. From analysis of deuterated leucine side chain spectra it was shown that $KL_4$ lies in the plane of the bilayers and adopts an unusual helical structure which confers amphipathicity and allows partitioning into the lipid bilayer interior. One of the most quantitative of the $^2$H NMR leucine studies is by Vugmeyster (discussed above), in which relaxation behavior is described by a phenomenological distribution of activation energies for $CD_3$ motions at high temperature, which collapses to a single distinctly smaller value at lower temperatures. Slower dynamics extracted by analysis of the line shape were attributed to diffusive motion of the peptide backbone and to exchange between the four unique side chain rotamers.

## 4.6 Conclusion:

Surface-adsorbed proteins are perhaps the most challenging systems to be studied by solid state NMR. In contrast to crystalline proteins that are up to 50% protein by weight, NMR samples of surface-adsorbed proteins are less than 5% protein, assuming monolayer coverage is achieved. In practice coverages lower than monolayer are encountered. As a result, for the study of macromolecular surface dynamics with $^2$H NMR, it is both desireable and necessary to use deuterium MAS methods. Here we have not only acquired high quality deuterium MAS spectra from samples of selectively deuterated surface-adsorbed proteins, but we have also shown that these MAS line shapes can be quantified in terms of specific models of amino acid side chain motions, and that these dynamics are indicative of surface proximity. The present study demonstrates these $^2$H MAS approach applied to samples of surface-adsorbed deuterated leucyl peptides, which have high deuterium content and relatively narrow lines, and thus can also be studied using static $^2$H NMR line shape analysis. In the future we will show how $^2$H MAS makes possible the detection of line shape that are much broader than shown here, namely phenylalanine side chains attached to surface-adsorbed proteins.

# Appendix IV. Line Shape and Relaxation Simulations at different Temperatures and on different Surfaces

## 1. 2H MAS NMR lineshapes and simulations

Data sets on PS and PSCOOH at all temperatures are given as experimental line shapes (purple), simulation fits (blue), and the subtraction difference between the two. It is usually not possible to match the experimental and simulated linewidths exactly, due to experimental sources of broadening that are not reproduced by simulation (e.g. magnet drift, imperfect pulses). Instead, matching of the peak heights has been used to determine quality of fit.

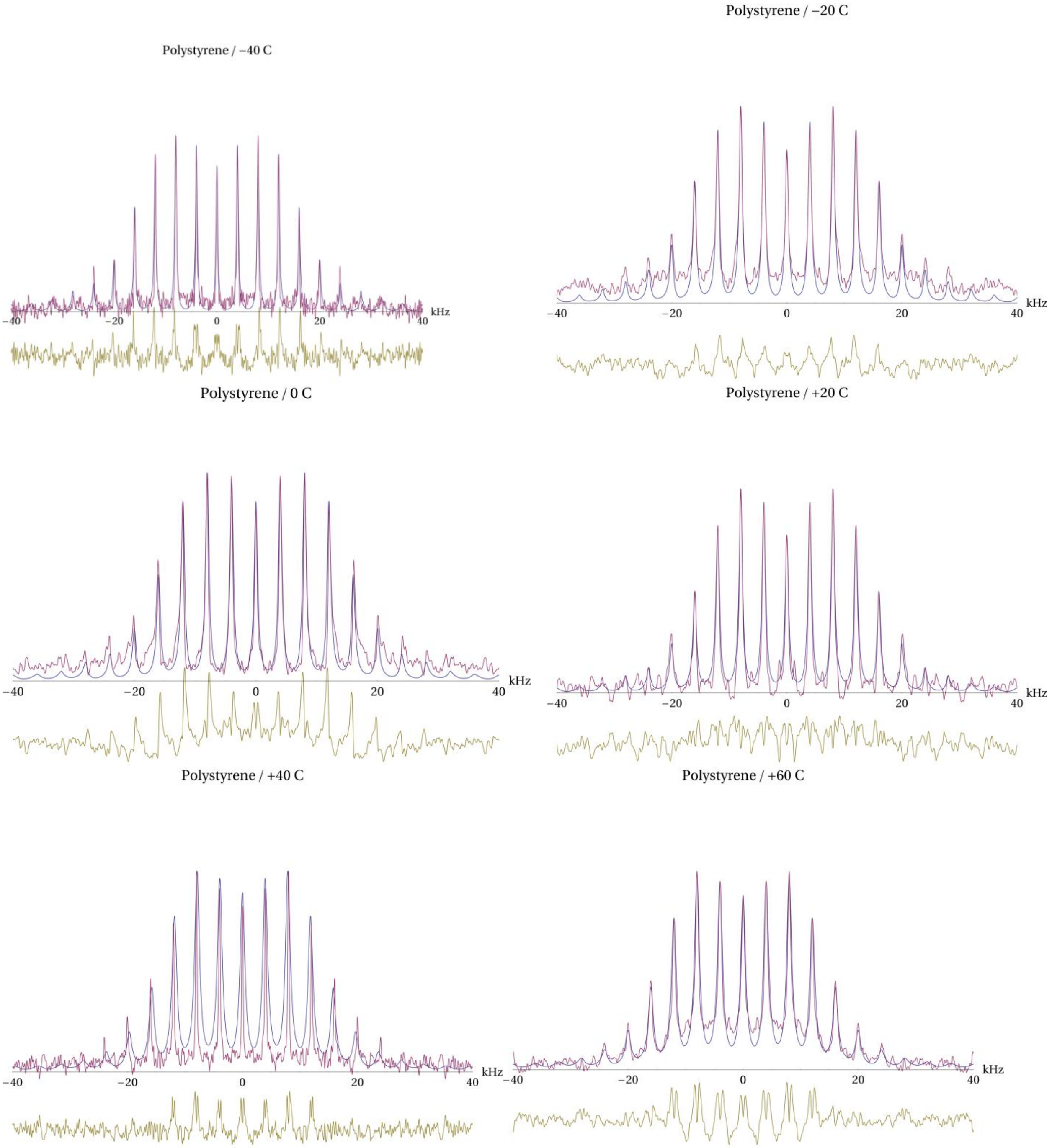
Polystyrene / −40 C

Polystyrene / −20 C

Polystyrene / 0 C

Polystyrene / +20 C

Polystyrene / +40 C

Polystyrene / +60 C

Figure A.IV.1. MAS spinning line shapes (purple) and simulation fits (blue) for the L8 peptide at different temperatures on PS

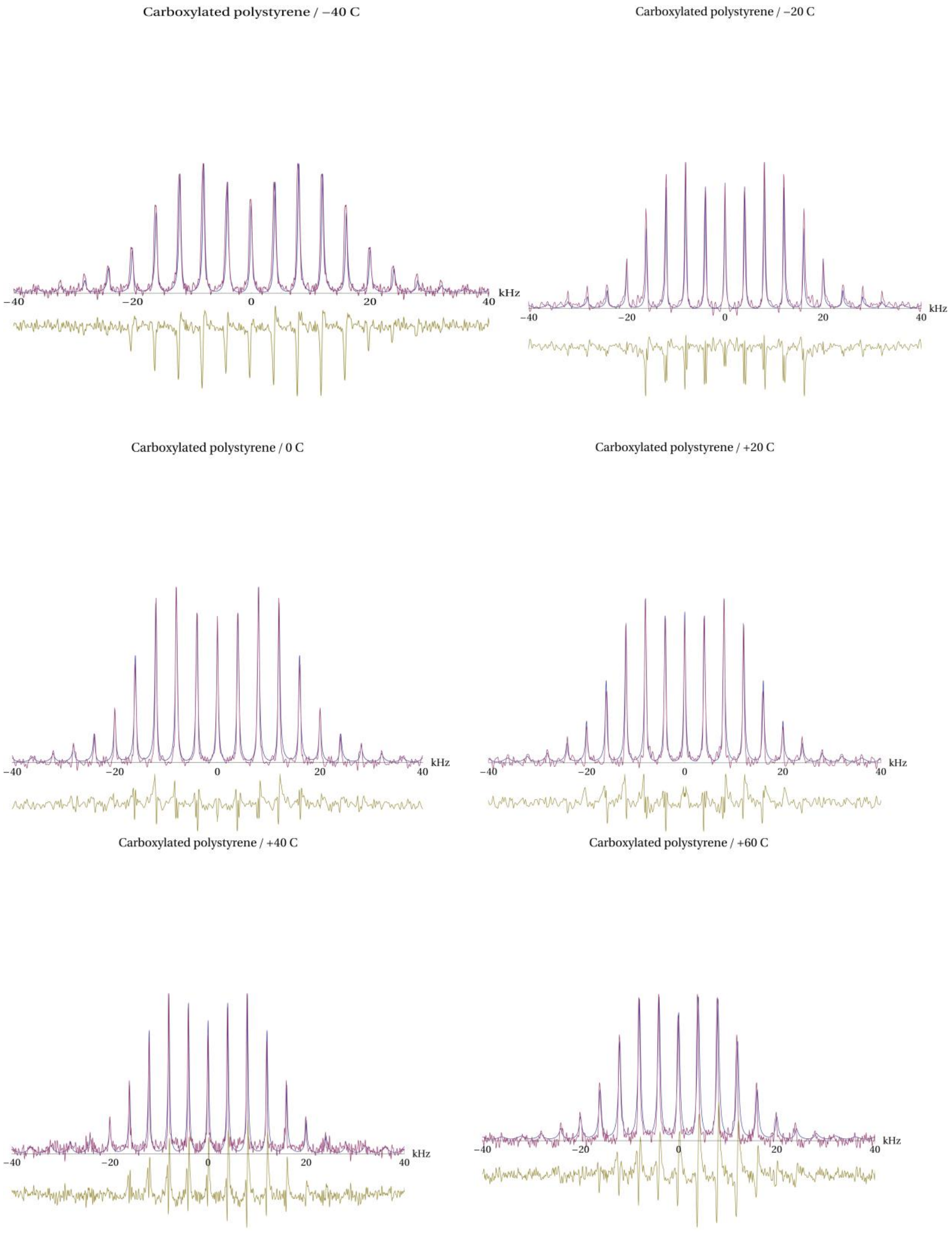

Figure A.IV.2 MAS spinning line shapes (purple) and simulation fits (blue) for the L8 peptide at different temperatures on PSCOOH

## 2. Details of sidebands

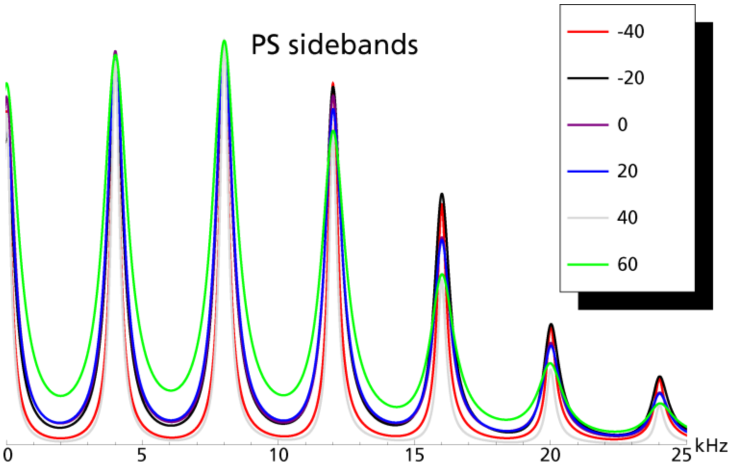

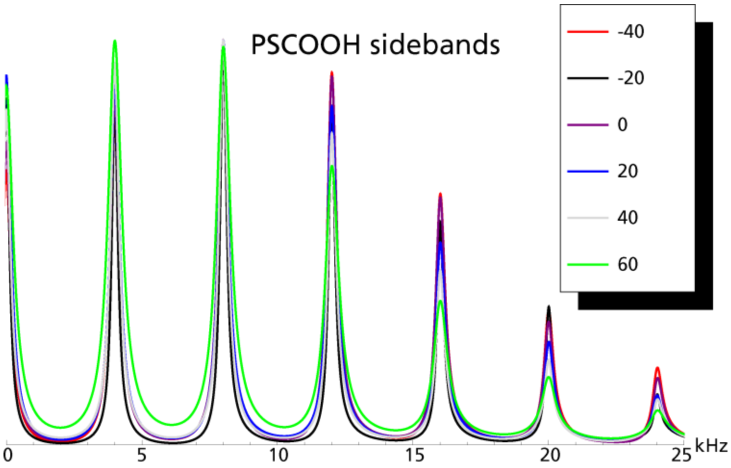

Figure A.IV.3 Details of Side Bands. The central transition and first six spinning sidebands are shown in detail to clarify the differences as a function of temperature, particularly in the outer sidebands. Spectra are symmetric around zero.

## 3. 2H NMR Inversion Recovery

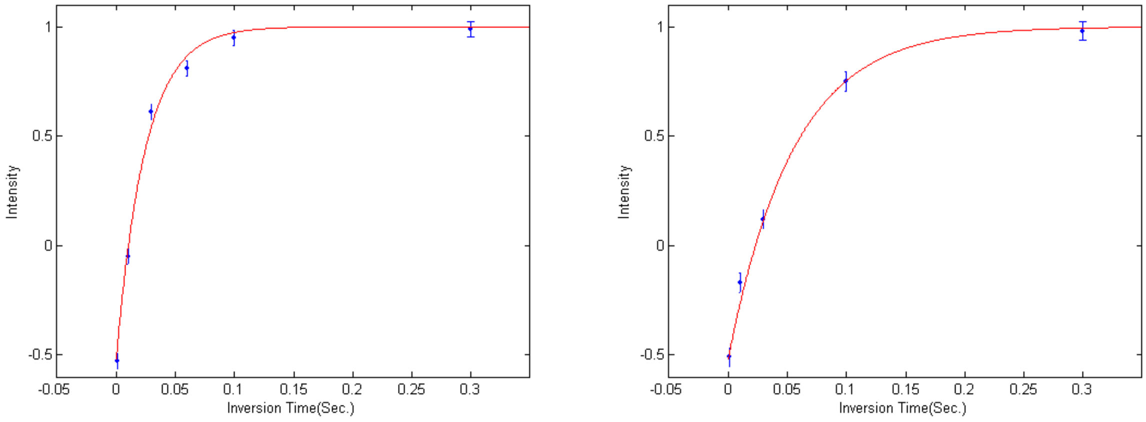

(a) −40 °C

(b) 20 °C

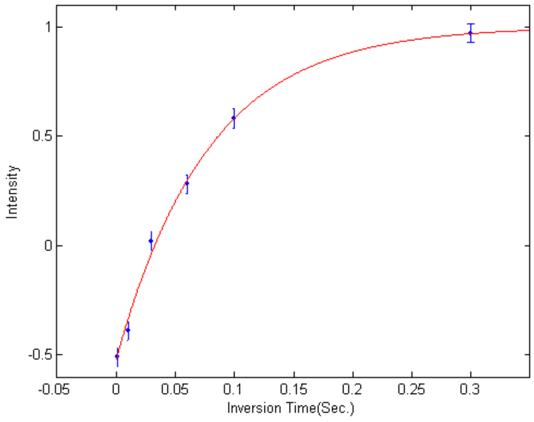

(c) 50 °C

Figure A.IV.4 2H NMR Inversion Recovery($T_1$) Fits on PS surface at different Temperatures. Fits and error bars are given for all inversion recovery ($T_1$) experiments. Intensity is given as a fraction of the fully relaxed line intensity.

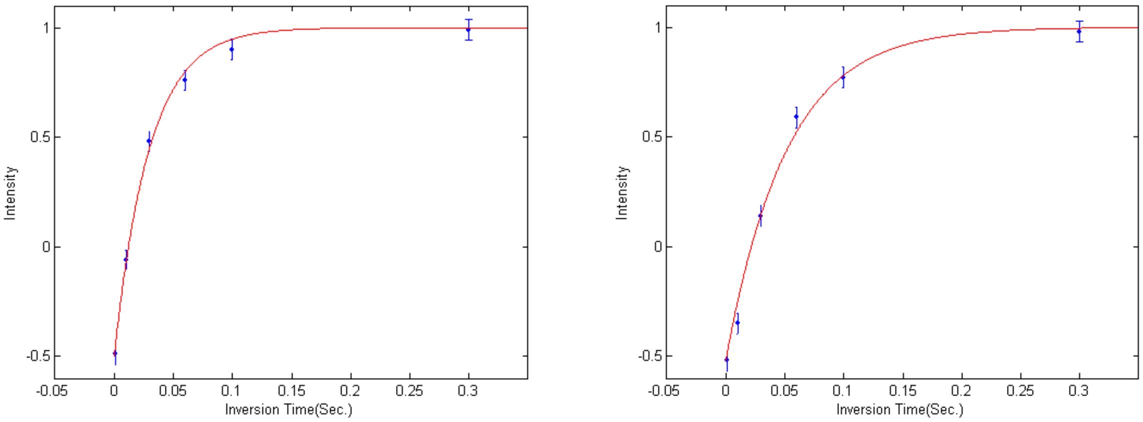

(a) −40 °C

(b) 20 °C

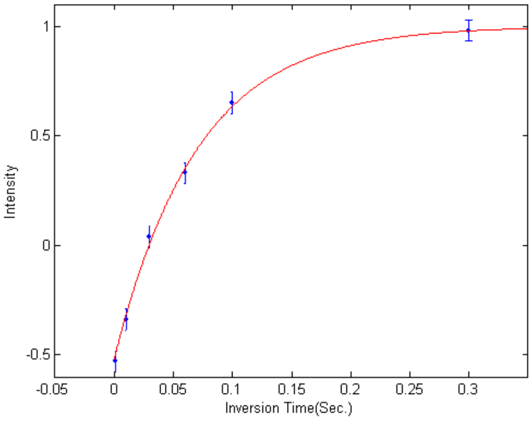

(c) 50 °C

Figure A.IV.5 2H NMR Inversion Recovery($T_1$) Fits on PSCOOH surface at different Temperatures. Fits and error bars are given for all inversion recovery ($T_1$) experiments. Intensity is given as a fraction of the fully relaxed line intensity.

# Chapter V.

# A Study of Phenylalanine Side Chain Dynamics in Surface-adsorbed Peptides Using Solid State Deuterium NMR and Rotamer Library Statistics

## Abstract

A number of interesting extracellular matrix proteins act as nature's crystal engineers, where they regulate the primary and secondary nucleation of hydroxyapatite (HAP) in bone and teeth. Extracellular matrix proteins adsorbed onto mineral surfaces experience a unique environment where the structure and dynamics of the protein can be altered profoundly. Here we study the dynamics of non-polar side chains within the mineral -recognition domain of the biomineralization protein salivary statherin which has been adsorbed onto its native HAP mineral surface. The dynamics of phenylalanine side chains located in the surface-adsorbed fifteen amino acid HAP-recognition fragment (i.e. SN-15) are studied using deuterium magic angle spinning ($^2$H MAS) line shape and relaxation measurements. $^2$H NMR MAS spectra and relaxation times of deuterated phenylalanine side chains within the adsorbed and free HAP recognition peptide domain are interpreted using an iterative approach where $^2$H MAS line shapes are fitted to a model where the phenylalanine side chain exchanges between rotameric states. In condensed proteins and in solution, phenylalanine rings are commonly observed to flip by 180 degrees, i.e. the "$\pi$ flip". The number of exchanging rotameric states in phenylalanine side chains increases upon adsorption to a HAP surface indicating that increased dynamic freedom accompanies transition of the protein from the hydrated solid state to the hydrated, biofilm state. In particular, rotameric exchange is observed to occur about the $C_\alpha - C_\beta$ bond in phenylalanine side chains for SN-15 molecules adsorbed onto HAP surfaces. Motion around the $C_\beta - C_\gamma$ bond is described as

an exchange between non-rotomeric states together with a $\pi$ flip. Although rotameric exchange motions of the $C_\alpha - C_\beta$ bond of phenylalanine have been observed by Ernst and coworkers for small peptides in aqueous solutions, this is the first time such exchange has been observed in solid state samples. Moreover, when the dynamics of two different phenylalanine side chains within the SN-15 peptide are compared, it is found that both rotameric populations and exchange rates differ as functions of orientation and surface proximity. These results indicate that the side chain dynamics of surface-adsorbed peptides differ markedly from the dynamics of the same peptides in bulk, condensed phases, and actually resemble to a greater degree the dynamics of side chains in small peptides in solution.

## 5.1 Introduction

Proteins do not exist as static forms but rather undergo internal motions that modulate both their secondary and tertiary structures. In many cases these internal motions result in structural rearrangements that are necessary for function[81-88]. Therefore the motions of the atomic components of the polypeptide backbone have been studied intensely by a number of techniques including solution NMR, solid state NMR, EPR, Raman, fluorescence, to name a few. In addition, the amino acid side chains attached to the protein main chain possess numerous degrees of angular freedom and thus are assumed to also be mobile to varying extents[89-91]. Magnetic resonance spectroscopies use a number of approaches for quantifying the time scales and amplitudes of protein side chain motions. Side chain motions occurring at correlations times less than 0.1 ns can be quantified by solution NMR using spin-lattice (i.e. )$T_1$ relaxation measurements, usually interpreted in terms of generalized order parameters and correlation times using a Model-Free theoretical framework[92]. Protein motions occurring with correlation times longer than 1 microsecond can be described by studying the power dependence of $T_{1r}$ and by relaxation dispersion measurements[93]. Amplitudes of protein motions can also be determined from residual $^{13}C$-$^{1}H$ and $^{15}N$-$^{1}H$ residual dipolar couplings (RDC), obtained from solutions of partially oriented proteins. Because of the small values of these static dipolar coupling constants, the RDC measurements themselves do not quantify the exact time scales of protein motions, although occurrence of motions in the ns-us time scale regimes may be inferred from RDC measurements after comparison to amplitude information obtain by relaxation measurements[94].

Solid state NMR is now widely used to study the dynamics of proteins in various physical states including hydrated amorphous powders [77], microcrystals[95], and fibrils[49]. Solid state NMR studies of membrane-associated proteins and peptides are extremely common[96]. Although by using the relaxation rates of $^{13}C$ and $^{15}N$ spins in solid, hydrated proteins may also be measured and evaluated as in solution NMR to obtain order parameters and correlation times using a Model-Free theoretical approach, quantifying dynamic rates and amplitudes is only possible using deuterium solid state NMR ($^{2}H$ ssNMR). To a very good approximation, the solid state $^{2}H$ ssNMR spectrum is dominated by a single interaction: that of the electric quadrupole moment of the $^{2}H$ nucleus with surrounding electric field gradients. The magnitude of this interaction is quantified by the deuterium quadrupolar coupling constant (i.e. QCC= $\frac{3e^2qQ}{4\hbar}$), which is on the order of 170 kHz for deuterons in $sp^3$ hybridized carbon-deuterium bonds[97]. The deuterium QCC greatly exceeds even the largest dipole-dipole interactions that deuterons are expected to experience within proteins. For example the dipolar coupling constant between a deuteron and a proton separated by 1 Angstrom is roughly 20 kHz. with realistic $^{2}H$-$^{1}H$ distances within a protein being greater. Given the magnitude of the anisotropy of the deuterium quadrupolar interaction, very fast motions (correlation times $\tau_c < 100\,\mathrm{ns}$) can be probed by Zeeman spin-lattice (i.e. $T_{1Z}$) and quadrupolar ($T_{1Q}$) relaxation measurements. Motions with correlation times $\tau_c < 10\,\mu\mathrm{s}$ partially average the anisotropy of the quadrupolar interaction. Motions with rates on the order of the anisotropy of the quadrupolar interaction ($10\,\mu\mathrm{s} < \tau_c < 1\,\mathrm{ms}$) dynamically perturb $^2$H NMR line shapes.

In spite of its usefulness as a probe of molecular dynamics, $^2$H ssNMR has practical limitations. The large anisotropy of the quadrupolar interaction and the small size of the deuterium spin magnetic dipole moment result in low sensitivity which makes difficult the extension of $^2$H ssNMR to large macromolecular system with high deuterium dilution, e.g. selectively deuterated proteins oriented in lipid vesicles or adsorbed onto biomaterial surfaces. Deuterium Magic Angle Spinning ($^2$H MAS) NMR has emerged in recent years as a viable alternative to static quadrupolar echo spectroscopy. Spinning a deuterated sample rapidly around a goniometer whose axis is oriented at 54.74° (i.e., the magic angle) relative to the direction of the static external magnetic field, breaks the $^2$H NMR solid state line shape into side bands separated by intervals of the spinning frequency $n_R$, where typically $1\,\mathrm{kHz} < \nu_R < 20\,\mathrm{kHz}$. Because the integrated intensity of the $^2$H NMR spectrum is concentrated into a small number of side bands in a MAS experiment, sensitivity enhancements of 20-30 are easily achievable. This feature makes $^2$H MAS NMR a potentially powerful approach for studying the dynamics of very small quantities of selectively deuterated biopolymers.

Recently, we have shown how $^2$H MAS NMR can yield high-quality (i.e. high signal-to-noise) spectra of a so-called LK peptide adsorbed at monolayer coverage on polystyrene and carboxylated polystyrene surfaces[98]. Both solid state NMR[66] and Sum Frequency Generation (SFG) vibrational spectroscopies[70] have shown that LK peptides with hydrophobic periodicity assume helical secondary structures on polar and non-polar surfaces. Analysis of the $^2$H MAS line shape of a 14 amino acid LK peptide (i.e. LKa14: Ac-LKKLLKLLKKLLKL-OH) with a single leucine side chain isopropyl-deuterated (L8, underlined), showed that the mobility of the side chain is dependent upon the orientation of the side chain relative to the surface which in turn is dependent on the surface functionalization. Therefore the MAS line shape is indicative of the orientation of LK peptides adsorbed onto functionalized polymer surfaces.

In this manuscript we extend $^2$H MAS NMR to the study of amino acid side chain dynamics in a biomineralization protein adsorbed onto its native mineral surface. Salivary statherin is a 43 amino acid proline and tyrosine-rich phosphopeptide found in the sub-mandibullar saliva. Statherin has the dual function of inhibiting both nucleation and crystal growth of hydroxyapatite [$Ca_{10}(PO_4)_6(OH)_2$, (HAP)] in the oral environment[99]. Statherin also acts as a boundary lubricant and has been found to have bacterial binding domains for *Porphyromonas gingivalis*[100] and *Actinomyces* v*iscosus*[101]. The N-terminal fifteen amino acids of statherin (i.e. SN-15: DpSpSEEKFLRRIGRFG, pS=phosphoserine) constitute the HAP recognition domain of the protein[102-104]. If SN-15 is deleted from statherin, the HAP binding affinity is markedly decreased. The HAP binding affinity of SN-15 itself is almost as large as that of statherin[105].

The structures of both SN-15 and statherin adsorbed onto HAP crystals have been studied by solid state NMR dipolar recoupling techniques[105,106]. SN-15 and the segment of statherin containing the N-terminal fifteen amino acids when bound to HAP are both helically structured, although in both cases the secondary structure is distorted from a classical a-helix. The distorted helical secondary structure of statherin's HAP binding domain appears to optimize exposure of several polar amino acid side chains to the HAP surface including E4, K6, R9, and R10[107,108]. Molecular modeling constrained by ssNMR dipolar recoupling data show that the majority of the nonpolar side chains in statherin's HAP recognition domain: F7, L8, I11, F14, are more remote from the HAP surface. In SN-15 however, distortion of the helical structure near the C-terminus allows the phenyl ring of F14 to orient close enough to the HAP surface to produce a $^{13}C\{^{31}P\}$ REDOR response[105]. Analysis of the REDOR data showed that the phenyl ring of F14 is around 4 Angstroms from HAP surface phosphate groups. No REDOR signal is observed for the phenyl ring of F7 in SN-15 so the $^{13}C$ spins in this phenyl ring are >7 Angstroms from the nearest HAP surface phosphate groups.

The differential surface exposure of two phenylalanine side chains in SN-15 presents the opportunity to study the effect of the mineral surface environment and specifically surface proximity on side chain dynamics. In this manuscript, we obtain $^2H$ MAS line shapes for SN-15 molecules selectively deuterated on the phenyl rings of F7 and F14 unbound and bound to HAP crystal surfaces. By analysis of these dynamically averaged line shapes and $T_1$ data, we show the degree to which surface adsorption perturbs side chain mobility in proteins, and the more subtle effects exerted in HAP-adsorbed proteins when phenylalanine side chains are exposed to the HAP surface to differing degrees. This study gives a high resolution view of how the unique environment of the mineral surface impacts protein side chain motions, and how these motions differ very strikingly from motions of phenylalanine side chains in solid proteins.

## 5.2 Materials and Methods.

## Peptide Synthesis

***Materials.*** Protected amino acids and Fmoc-Gly-Wang resin were purchased from Calbiochem Novabiochem Corp. (San Diego, CA). [Ring-$^2H_5$] L-phenylalanine was purchased from Cambridge Isotope Laboratories, Inc. (Andover, MA). HAP (55 $m^2/g$) was synthesized by Allison Campbell at Pacific Northwest National Lab as published previously[102].

***Peptide Synthesis and Characterization.*** Both [ring-$^2H5$]-labeled phenylalanine SN 15 samples were prepared as follows. [Ring-$^2H5$] L-phenylalanine was FMOC protected using standard procedures[109]. From a preloaded Fmoc-Gly-Wang resin (substitution 0.60 mmol/g), the SN-15 peptide was synthesized on a Rainin PS3 automated solidphase peptide synthesizer (Protein Technologies, Inc.), where the solvent was *N*,*N*-dimethylformamide (DMF), the activator was 0.4 M *N*-methylmorpholine in DMF, and the deprotector was 20% (v/v) piperidine in DMF. The acidic portion of SN-15 (D1 to K6) was double coupled, while the rest of the peptide was built through single couplings. The peptide was cleaved from the resin using a 9.5 TFA:0.25 $H_2O$:0.25 TIS (triisopropylsilane) solution following Method 3-18 described in the Novabiochem 2002/3 catalog.52 Using a Waters HPLC C-18 reverse phase column, the peptide was purified with an acetonitrile/water solvent system with 0.1% TFA, eluting at 35.4% acetonitrile, lyophilized, and then analyzed by MALDI mass spectrometry to establish composition and purity.

***Peptide Adsorption to HAP.*** SN-15 was physisorbed to HAP by mixing a solution composed of 0.05 mM of peptide in a phosphate buffer with about 100 mg of HAP (55 m2/g). The pH of the mixture was adjusted to 7.4 with NaOH and HCl. The phosphate buffer was 100 mM NaCl, 40 mM KCl, 1.4 mM $KH_2PO_4$, and 4.3 mM $Na_2HPO_4$. After 4 h of mixing, the unbound peptide was separated from the peptide-HAP complex though centrifugation. The peptide-HAP sample was washed several times with buffer, then it was lyophilized and packed in the rotor for solid-state NMR studies.

## NMR Experiments

All MAS line shapes were taken on a Solid State NMR spectrometer equipped with a 9.4T magnet (61.5 MHz. deuterium Larmor frequency) using a Varian T3 MAS probe and 4mm sample rotors. In these MAS experiments, samples were spun at 8 kHz (regulated to within ± 5 Hz by a spin-rate controller). A single $\frac{\pi}{2}$ pulse (2.5 $\mu s$ in length) was applied followed by acquisition of the rotary echo train. After left-shifting to the peak of the first echo, FIDs were Fourier transformed and phase corrected. All line shapes have a Lorentzian broadening of 1 kHz. All measurements were made at 3 different temperatures, -30°C, 20°C, 60°C. For the $T_1$ experiments, we used a simple inversion-recovery pulse sequence with a π pulse length of 5.5 $\mu s$. The π pulse was followed by a delay which is used to recover the magnetization. Then the single $\frac{\pi}{2}$ pulse was applied followed by acquisition. For the free peptide, the delay time was set to 9 different time points, and the relaxation time between acquisitions was carefully chosen to be 4 second; while for the bound peptide, the delay time was set to 8 different time points, but the relaxation time between acquisitions was set to 0.4 second.

## Simulation Methods

***Deuterium MAS Line Shape Simulation Algorithm:*** $^2$H NMR MAS spectra and inversion-recovery experiments were simulated with an in-house program, KLDMAS. The theory of KLDMAS has been described in detail elsewhere[110] and in Chapter II. Here we give a brief overview. In a MAS experiment, a powdered sample is spun at a frequency $n_R$ around a goniometer whose axis is tilted at 54.74 degrees relative to the direction of the static magnetic field. The evolution of magnetization is given by:

$$\frac{dM_\pm}{dt} = \Gamma(t) M_\pm(t) = \left(i\omega_\pm(t) + \pi\right) M_\pm(t) \tag{5.1}$$

where the time displacement of the transverse magnetization M(t) is described by the operator Γ(t), the subscript ± refers to the m=1 to m=0 or the m=0 to m=−1 transition, and π is the matrix that describes the process of exchange between n discrete conformational sites. The term $\omega_{\pm}$ is a diagonal matrix with non-zero elements corresponding to the resonance frequencies of the deuterium spin at the various sites. The MAS rotation imparts a time dependence to the elements of the matrix $\omega_{\pm}$, and because of this time dependence, equation (5.1) cannot be integrated analytically as is the case with static samples[14]. Instead we use an approach developed by Duer and Levitt[23], which numerically integrates equation (5.1) by dividing the rotor period into N intervals each of length $\Delta t = \tau_R / N$, where N is sufficiently large that during Δt, $\omega_{\pm}$ and thus Γ are approximately constant. Therefore, at any time mDt (i.e. $1 \le m \le N$), the MAS propagator can be obtained iteratively:

$$\exp\left(\Gamma\left(m\Delta t\right)\right) \approx \exp\left(\left(i\omega_{\pm}\left(t_m\right)+\pi\right)\Delta t\right) \times \exp\left(\Gamma\left(\left(m-1\right)\Delta t\right)\right) \tag{5.2}$$

where $t_m=(m-1)\,\Delta t/2$ and we assume G(0)=1. The propagator for any time $t+Mt_R$ is then given by:

$$\exp\left(\Gamma\left(t+M\tau_R\right)\right) \approx \left(\exp\left(\Gamma\left(\tau_R\right)\right)\right)^M \times \exp\left(\Gamma\left(t\right)\right) \tag{5.3}$$

Equations (5.2) and (5.3) are the basis for our $^2$H MAS line shape simulation program KLDMAS, which was used to generate all MAS line shape simulations shown in this paper. The process of MAS line shape simulation was automated, and involves comparison of experimental spinning side bands' intensities to simulated intensities. The number of spinning side bands is predefined before the simulation, and it usually does not contain the center peak which is assumed in most cases to contain a contribution from residual HDO in the sample. The parameter set for a specific dynamic model includes: the deuteron QCC, site populations, side chain bond dihedral angles $\chi1$ and $\chi2$, and site exchange rates. The dihedral angles are varied within the range of a standard deviation.

To optimize the speed of the MAS line shape fitting, a threshold accepting (TA) algorithm was used[111]. The TA algorithm proceeds as follows. A positive value called the threshold T is initially set. An initial parameter set is used to calculate a MAS line shape .which is compared to the experimental MAS line shape and used as a basis for a $\chi^2$ calculation. The parameter set is then stochastically perturbed and the procedure is repeated to obtain a new $\chi^2$. The two $\chi^2$ are compared. If $\chi^2$(old)- $\chi^2$(new)<T, then the new variable set is accepted, otherwise it is rejected. As simulations proceed , the threshold value T is manually decreased until it goes to zero. The primary difference between the TA method and simulated annealing (SA) is that, instead of using a constant threshold value , the SA method uses a probability which depends on a time-dependent temperature. We found that both methods can give satisfactory result but the TA method is faster. A specific example of selected steps in the TA-based simulation of the MAS line shape of the ring deuterons of F7 in HAP-bound SN-15 (see Figure 5.4c) is provided as supplementary information.

***Deuteron NMR Relaxation:*** KLDMAS is also used in this paper to simulate inversion-recovery $^2$H MAS experiments. The response of the deuterium spin system to an inversion-recovery pulse sequence is obtained by multiplying the iterated propagator by $(1-2e^{-\tau/\langle T_1\rangle})$ where $\tau$ is the variable time delay between the inversion pulse and the $\frac{\pi}{2}$ pulse, and the spin lattice relaxation rate $R_1 = 1/T_1$ is given by

$$R_1 = 1/T_1 = \frac{3}{16}(\frac{e^2 qQ}{\hbar})^2 \cdot [J_1(\omega) + 4J_2(2\omega)] \qquad (5.4)$$

In the limit that the rate of spinning exceeds the static spin lattice relaxation rate, and for the case of exchange between N discrete sites, the spectral density has the form[24]:

$$
\begin{aligned}
J_m(\omega) = 2\int_0^{\infty} \bar{\mathrm{C}}_m(t) Cos(\omega t) dt = \sum_{b=-2}^{2} [d_{mb}^{(2)}(\theta_{lm})]^2 \sum_{a,a'=-2}^{2} D_{ba}^{(2)*}(0,\theta_{mc},\psi_{mc}) D_{ba'}^{(2)}(0,\theta_{mc},\psi_{mc}) \\
\sum_{nlj=0}^{N-1} X_l^{(0)} X_l^{(n)} X_j^{(0)} X_j^{(n)} D_{a0}^{(2)*}(\phi_l,\theta_l,0) D_{a'0}^{(2)}(\phi_j,\theta_j,0) \frac{-2\lambda_n}{\lambda_n^{\ 2} + \omega_0^{\ 2}}
\end{aligned}
\qquad (5.5)
$$

In equation 5.5 the solid angle $\Omega_{LM} = \left(0, \theta_{lm}, \psi_{lm}\left(t\right)\right)$ relates the goniometer frame M to the laboratory frame L. The angle between the magnetic field direction and the goniometer axis is $\theta_{lm}$ and the angle $\psi_{lm}(t) = \mathrm{w}_r t$ is time dependent as a result of the sample rotation at a frequency $\mathrm{w}_r$. The spectral density in equation (5.5) is therefore the cosine Fourier transform of a correlation function $\bar{\mathrm{C}}_m(t)$ that has been averaged over the motion of the spinner. Also in equation (5.5), $X$ and $\lambda$ indicate the eigenvector and (diagonal) eigenvalue matrices, respectively of the symmetrized jump matrix.

## 5.3 Results

***Model for Phenylalanine Side Chain Dynamics in Unbound SN-15:*** As shown in Figure 5.1a, the conformational state of the phenylalanine side chain is quantified by two bond dihedral angles: $\chi_1$ and $\chi_2$. $\chi_1$ is defined as the angle between $N - C_\alpha - C_\beta$ and $C_\alpha - C_\beta - C_\gamma$ planes, and thus quantifies the rotational state of $C_\alpha - C_\beta$ bond. The rotational state of $C_\beta - C_\gamma$ bond is described by $\chi_2$, which is defined as the angle between $C_\alpha - C_\beta - C_\gamma$ and $C_\beta - C_\gamma - C_\delta$ planes. Motions of the phenylalanine side chain are quantified by ascribing time dependence to one or both of these angles. Opella and coworkers[112] used the quadrupole echo (QE) $^2$H NMR spectra of [$^2$H5]-phenylalanine in polycrystalline form and incorporated into the coat protein of the filamentous bacteriophage fd to demonstrate that the aromatic rings in phenylalanine side chains undergo rapid 180° flips (i.e. $\pi$ flips) about their $C_\beta - C_\gamma$ bond axes, corresponding to a situation where $\chi_1$ is static but $\chi_2$ exchanges between two values that differ by 180°. The two states of $\chi_2$ related by the $\pi$ flip were determined also to have equal a priori populations. The $^2$H NMR powder patterns from the $\delta$ and ε C-D bonds of [$^2$H5]-phenylalanine indicate the aromatic ring motions are in the fast exchange limit. The authors concluded from their analysis that the rate of phenyl ring flipping is faster than 0.2 MHz. and that the results are incompatible with diffusional rotation occurring on this time scale. Similar "$\pi$ flips" of phenylalanine rings have been observed in bacteriorhodopsin[113] and in polyphenylalanine[114]. The deuterium MAS line shape of crystalline phenylalanine has also been analyzed using a "π flip" dynamic model by Huang[115].

In this manuscript we use the "π flip" dynamic model of phenylalanine side chain motion to simulate the motions of the aromatic rings of F7 and F14 in unbound SN-15. Accordingly, the phenylalanine rings in F7 and F14 in unbound SN-15 are simulated as undergoing fast π flips around $C_\beta - C_\gamma$ bond, which changes drastically the orientation of the $\delta$ and ε C-D bonds but leaves invariant the ζ C-D bond orientation.

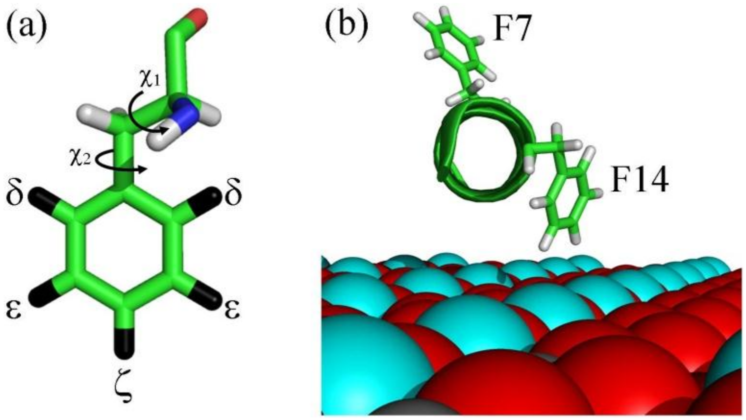

Figure 5.1 A model of phenylalanine and SN15 on HAP surface.
(a). A model of phenylalanine is presented. The deuteration sites are denoted in black, along with the two rotational axes.
(b) A model of SN15 is depicted indicating the close proximity of the phenylalanine residue at position 14 to the HAP surface.

**Deuterium MAS Line Shape Simulations for Unbound SN-15-** $^2$H MAS line shapes obtained for unbound SN-15 with [Ring-$^2H_5$] L-phenylalanine incorporated at F7 and F14 are shown in Figure 5.2 for a temperature of T=293K. Additional $^2$H MAS line shapes at temperatures 243K, and 333K and simulations are provided as supplementary information. The MAS line shapes for unbound SN-15 contain features observed in earlier QE studies of phenylalanine dynamics. Because the ζ deuteron is invariant to the π flip, the phenylalanine MAS line shapes are superpositions of two line shapes: a motionally averaged line shape arising from the $\delta$ and ε deuterons, and a static line shape arising from the ζ deuteron.

Because the $T_1$ of the relatively immobile ζ deuteron is much longer than $T_1$ for the dynamic $\delta$ and ε deuterons, if experimental delays are much shorter than the ζ deuteron $T_1$, the intensity ratio of the line shapes will deviate from the expected 4:1 ratio. In SN-15, fully relaxed $^2$H MAS spectra for ζ deuterons in both F7 and F14 can be obtained using recycle delays of less than 10s. In these fully relaxed $^2$H MAS spectra the intensity of the ζ deuteron line shape exceeds the intensity of the $\delta$ and ε line shape, an effect ascribed by Gall et al and others to a population of immobile phenylalanine rings[112]. In SN-15 we ascribe this observation to two factors: 1) a population of immobile rings and 2) attenuation of the $^2$H MAS echo train by slow motions.

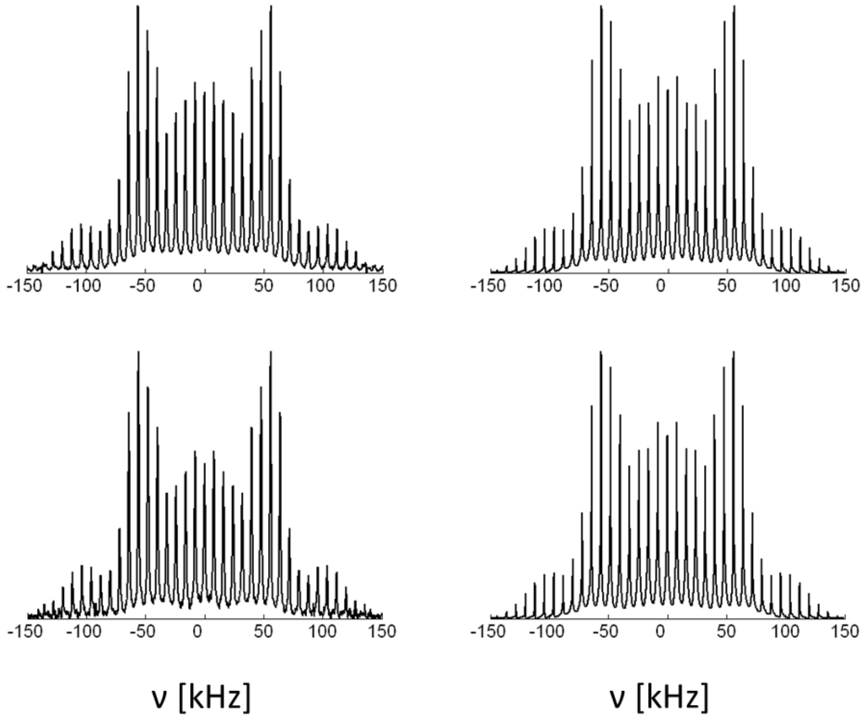

Figure 5.2. Experimental spectra of F7 and F14 in free peptide vs simulations
Left: Experimental spectra of F7 (top) and F14 (bottom) in free SN15 peptides at room temperature;
Right: Corresponding simulations

In unbound SN-15, $T_1$s for the *δ*/ε deuterons of F7 and F14 decrease as the temperature increases, see Table 1, indicating that the motion of the F7 and F14 rings in unbound SN-15 are on the so-called slow side of the $T_1$ curve.

Table 5.1: $T_1$ for the *δ*/ε and ζ deuterons of F7 and F14 in unbound SN-15 as a function of temperature.
All $T_1$ values are in units of seconds.

| | T=-243K | T=293K | T=333K |
|---|---|---|---|
| F7 (*δ*/ε) | 0.106±44 | 0.054±18 | 0.016±7 |
| F7 (ζ) | 1.238±157 | 1.111±240 | 0.738±120 |
| F14(*δ*/ε) | 0.070±13 | 0.025±8 | 0.012±11 |
| F14(ζ) | 1.664±150 | 1.305±130 | 0.693±168 |

This means the dynamic rate (i.e. inverse of the correlation time $\tau_c$) of base flipping in unbound SN-15 is less than the deuterium Larmor frequency $\omega_0$ (i.e. $\nu_0$ =61.5x$10^6$ $s^{-1}$). Accordingly, the correlation times for the ring motions in Tables 5.2a and 5.2b satisfy the condition $w_0$ $\tau_c$>1.

.

It is also well known that in the QE line shape experiment, exchange-induced dephasing can interrupt the refocusing of the second pulse[17,18], and produce an absolute intensity loss of the spectrum[14]. This effect is especially pronounced when the correlation time of the motion is on the order of the time interval between the 90 degree pulses of the QE sequence. In a $^2$H MAS experiment, reorientation-induced frequency jumps during a rotor period interfere with the formation of the echo at the end of the rotor period causing it to have lower amplitude than the echo that commenced the rotor period[116]. Figure 5.3a shows how the intensity of the $^2$H MAS line shape for $\delta$/ε deuterons in a phenylalanine ring varies with the π flipping rate, assuming the experimental MAS spinning rate of 8 kHz. Figure 5.3b shows $^2$H MAS line shapes obtained for selected jump rates. Note the low amplitude of a jump rate of $10^5$ Hz. This figure implies that if a model system has several motions, usually the component that has a rate within the $10^4$-$10^6$ $s^{-1}$ motion regime has least contribution to the spectrum. In the case of a 8 kHz. spinning rate this attenuation is most severe for the range k=5x$10^4$-$10^6$ Hz. for $\delta$/ε deuterons in a π-flipping phenylalanine ring.

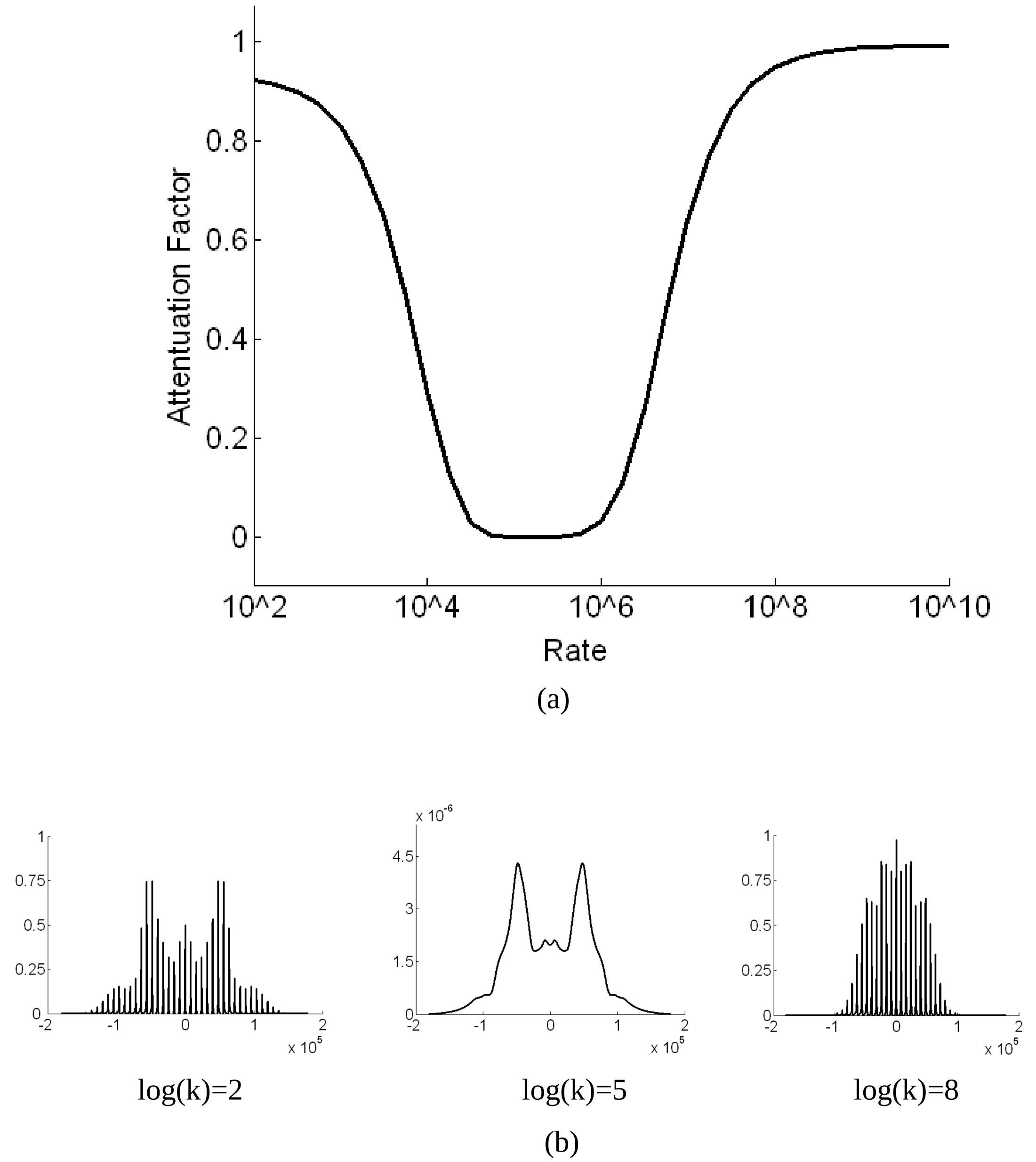

Figure 5.3. Theoretical $^2$H MAS NMR spectra and its intensity as function of the rate
(a) Theoretical $^2$H MAS NMR spectra intensity as function of the rate constant $k=k_{12}=k_{21}$ for a quadrupole coupling tensor whose principal axis system can assume two equally probable orientations relative to the crystallite fixed axis system. The orientations were given by $\Omega(\alpha,\beta,\gamma)=\{0,\pi/3,0\}$ and $\{0,\pi/3,\pi\}$. The calculations employed QCC=170 kHz, asymmetry parameter $\eta=0$, spin frequency $\upsilon_r=8$ kHz, and Lorentzian line broadening of 1 kHz.
(b) Theoretical $^2$H MAS NMR spectra at 3 jump rate constants. The intensity of each spectrum is normalized by dividing the spectrum intensity at fast limit rate.

Figure 5.3a predicts that the $\delta/\varepsilon$ deuteron MAS signal is severely attenuated for $\pi$ flipping rates in the range $10^5$-$10^6$Hz, but the signal intensity recovers as the flipping rate increases to greater than $10^6$ Hz or decreases to less than $10^5$ Hz in the present case. For F7, the rate of the π flip is around $1.4 \times 10^7$ Hz at room temperature, where attenuation of the δ/ε from slow motions should be moderate. The fact that the ζ deuteron signal still apparently exceeds the δ/ε signal even at high π flipping rates indicates that as in other studies of phenylalanine ring motion in peptides and proteins there exists a population of immobile rings for which the δ/ε is unattenuated (Note from tables 2a and b that when the temperature is decreased to 243K or increased to 333K, the immobile (i.e. ζ) deuteron signal increases or decreases relative to the mobile (δ/ε) deuteron signal. Both cases support a change in the rate of ring flipping with temperature: i.e. decreasing at lower temperature or increasing at high temperature relative to the ambient temperature rate.).

Table 5.2a. Simulation parameters for $^2$H line shape of deuterons of F7 in unbound SN-15

| F7 Simulation Parameters F7 | Static (ζ) Parameter Set | Flipping (δ/ε) Parameter Set |
|---|---|---|
| QCC(kHz) | 175.0 | 175.0 |
| Asymmetry Parameter | 0.06 | 0.06 |
| Flipping Rate(-30C) | 0 | $7.5 \times 10^6$ |
| Intensity Percentage(-30C) | 79% | 21% |
| Flipping Rate(20C) | 0 | $1.4 \times 10^7$ |
| Intensity Percentage(20C) | 75% | 25% |
| Flipping Rate(60C) | 0 | $5.0 \times 10^7$ |
| Intensity Percentage(60C) | 70% | 30% |

Table 5.2b. Simulation parameters for $^2$H line shape of deuterons of F14 in unbound SN-15

| Simulation Parameters for F14 | Static (ζ) Parameter Set 1 | Flipping ($\delta$/ε) Parameter Set |
|---|---|---|
| QCC(kHz) | 175.0 | 175.0 |
| Asymmetry Parameter | 0.06 | 0.06 |
| Flipping Rate(-30C) | 0 | $1.1\times10^7$ |
| Intensity Percentage(-30C) | 82% | 18% |
| Flipping Rate(20C) | 0 | $3.0\times10^7$ |
| Intensity Percentage(20C) | 79% | 21% |
| Flipping Rate(60C) | 0 | $6.7\times10^7$ |
| Intensity Percentage(60C) | 76% | 24% |

## Models for Phenylalanine Side Chain Dynamics in HAP-Bound SN-15:

$^2$H MAS line shape data acquired for F7 and F14 side chain deuterons in HAP-adsorbed SN-15 at T=293K are shown in Figure 5.4a and 5.4b, respectively. Additional $^2$H MAS line shapes at T=243K and 333K for the deuterons of F7 and F14 in HAP-bound SN-15 are provided in supplementary information. The line shapes in Figure 5.4 differ markedly from data acquired from the same sites in unbound SN-15 at T=293K shown in Figure 5.2a and 5.2b, indicating phenylalanine side chain dynamics in the protein in the unbound solid state differ significantly from the dynamics at the same sites in the surface-adsorbed protein. In particular, the Figure 5.4 line shapes display absence of an immobile component, which in the unbound SN-15 phenylalanine side chain deuteron line shapes in Figure 5.2 arose in part from the invariance of the ζ deuteron to the $\pi$ flip. The data in figure 5.4 indicate presence of additional motions of the phenylalanine side chain that average and/or attenuate the both the $\delta$/ε and $\zeta$ deuteron signal.

To simulate the line shapes for deuterated F7 and F14 in HAP-bound SN-15, a model was designed that includes rotational motions of both $C_\alpha - C_\beta$ and $C_\beta - C_\gamma$ bonds in addition to the $\pi$

flip of the $C_\beta - C_\gamma$ bond. We assume that the rotational motions of the $C_\alpha - C_\beta$ bond consist of rotameric exchanges. Dynamic models based on rotameric exchange have been used widely to simulate solid state $^2$H NMR line shape and relaxation data acquired from amino acid side chains in proteins, notably deuterons within the side chains of leucines and valines. In some cases exchange is restricted to side chain rotamers that are observed to be dominant in crystal structures. For example, in a series of studies of leucine side chain dynamics within the hydrophobic core of the villin head piece, Vugmeyster et al. assumed the side chain motions consist of exchanges between four structurally unique side chain rotamers with a priori populations x:1:1:1, where x is varied to achieve optimal line shapes fits[18].

In the models for phenylalanine side chain dynamics in HAP bound SN-15, the initial geometries and populations of exchanging conformers of $C_\alpha - C_\beta$ bonds were obtained from protein side chain rotamer libraries[90,91,117]. Side chain rotamer libraries show that for bonds between sp$^3$ hybridized carbons, dihedral angles occur in tight clusters typically around angles of 60, 180, and 300 degrees (i.e. gauch+, trans, gauche-). Depending upon the amino acid side chain in question, the exact location and shape of maxima in the side chain bond dihedral distributions vary by at most 20° with standard deviations usually less than 10° in high-resolution structures[91]. In the case of phenylalanine, the most recent backbone-dependent rotamer library of Shapovalov and Dunbrack shows that for a-helical secondary structures (i.e. f=-50$^o$, y=-40$^o$) the $C_\alpha - C_\beta$ bond dihedral angles are clustered near ideal rotameric values, i.e. $\chi_1$=179.8±9.1$^o$ with a probability of 0.721, $\chi_1$=286±10.8$^o$ with a probability of 0.254, and $\chi_1$=75.4±8.1$^o$ with a probability of 0.025. In contrast, bonds between sp$^3$ and sp$^2$ hybridized carbons in protein side chains exhibit broad and often asymmetric probability density distributions. Accordingly, the rotamer library of Shapovalov and Dunbrack shows that the dihedral angle $\chi_2$ for the $C_\beta - C_\gamma$

bond in phenylalanine is broadly distributed among non-rotameric values within the interval -30°<$\chi_2$<150°.

In the model designed to simulate the $^2$H MAS line shapes in Figure 5.4 a and b, we initially assumed that the dynamics of the $C_\alpha - C_\beta$ bonds consist of exchanges between the two dominant conformers i.e. $\chi_1$=179.8 (i.e. trans) and $\chi_1$=286 (gauche-). Because of its low probability of occurrence in the rotamer library, the gauche+ conformer was neglected. Because the $\chi_2$ angle in phenylalanine is not confined to specific rotameric values, this angle was freely varied. With regard to the $\delta$/ε deuterons the resulting model consists of a four site exchange, which combines a conjoint rotameric exchange motion of $C_\alpha - C_\beta$ and $C_\beta - C_\gamma$ bonds between two sites together with a π flip of the $C_\beta - C_\gamma$ bond, i.e. ($\chi_1 = trans, \chi_2 \pm \pi$)↔($\chi_1 = gauche-, \chi_2{}' \pm \pi$). Although the orientation of the C-D bond containing the ζ deuteron is invariant to rotations around the $C_\beta - C_\gamma$ bond axis, the orientation of this bond is changed by exchange of the $C_\alpha - C_\beta$ bond between the trans and gauche- states.

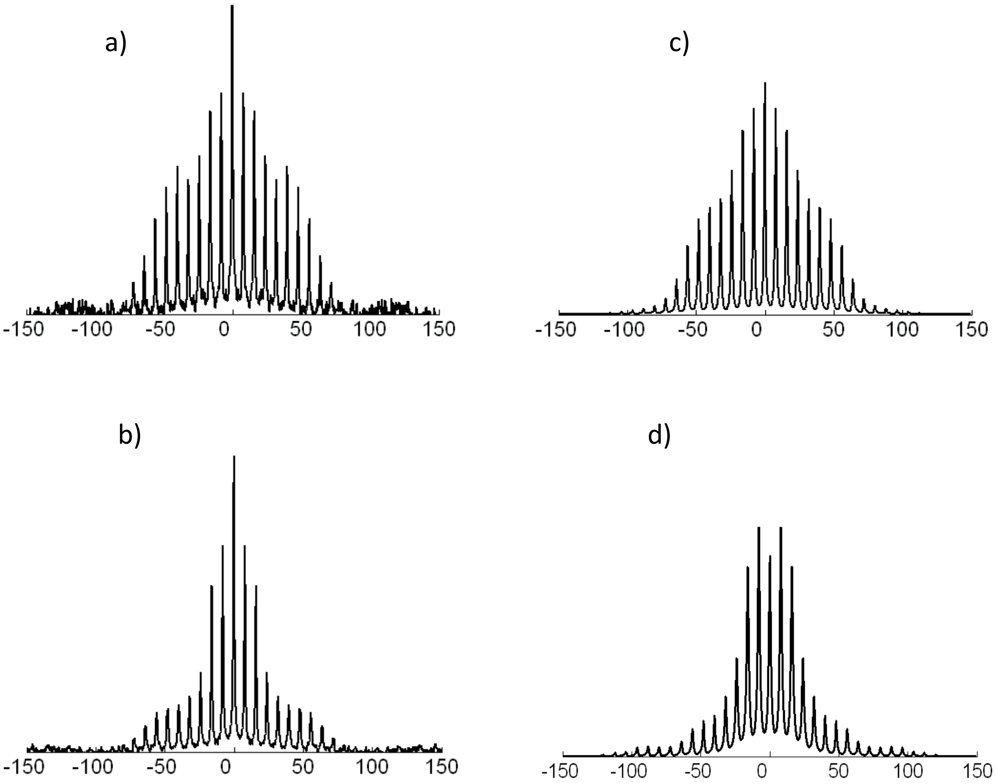

Figure 5.4 Experimental spectra of F7/F14 in SN15 peptides binding on HAP at room temperature vs simulations. (a) is MAS spectrum of bound F7; (b) is MAS spectrum of bound F14; (c) is MAS simulation of bound F7; (d) is MAS simulation of bound F14 . The intense peak in the center of the experimental spectra arises in part from surface-adsorbed HDO.

**Deuterium MAS Line Shape Simulations for HAP-bound SN-15-** Here we present simulations of the $^2$H ssNMR MAS line shapes for the ring deuterons of F7 and F14 in HAP-adsorbed SN-15, using the model of side chain dynamics described in the prior section. In each line shape simulation for the deuterons of each side chain, adjustable parameters include the side chain conformation populations and the exchange rate constant. These parameters are related by $R_{ij} = k\sqrt{\frac{P_i}{P_j}}$ where $P_i$ and $P_j$ are the populations of rotamers i and j, respectively, and k is the exchange rate constant. Initial values for $\chi_1$ and $\chi_2$ torsion angles were derived from the rotamer libraries. In the case of $\chi_2$, which is broadly distributed among non-rotameric values, initial values were obtained from an average of the library values. Both $\chi_1, \chi_2$ angles were subject to change within the single standard deviations listed in the library.

In addition to parameters for rotameric exchange motions of $C_\alpha - C_\beta$ and $C_\beta - C_\gamma$ bonds, the rate of the π flip motion was specified as follows. Table 5.3 shows $T_1$ measurements acquired for the $\delta$/ε ring deuterons of F7 and F14 as a function of temperature. Because of the small amount of peptide present on the surface, accurate $T_1$ values were not acquired for the $\zeta$ deuterons. In contrast to the F7 and F14 ring deuterons in unbound SN-15, whose spin-lattice relaxation times decrease with an increase in temperature, indicating presence of motions with rates less than the $^2$H Larmor frequency, the relaxation times for the same deuterons in HAP-bound SN-15 increase with temperature, indicating the motion of the F7 and F14 side chain have shifted to rates greater than the $^2$H Larmor frequency. $^2$H MAS line shape data in Figure 5.4 and the relaxation data in Table 5.3 indicate motions of the side chains of F7 and F14 occur with rates slow enough in partially average the line shape while other motions occur with rate greater than the deuterium Larmor frequency $\nu_0$=61.5x10$^6$ s$^{-1}$

Table 5.3 Spin lattice Relaxation ties $T_1$ for the $\delta$/ε Deuterons in Bound Peptide as a Function of Temperature

| Side Chain | Temperature(K) | Average $T_1$(ms) |
|---|---|---|
| F7 | 243 | 18.6±4.2 |
| | 293 | 21.6±3.5 |
| | 333 | 40.0±14.3 |
| F14 | 243 | 32.5±5.8 |
| | 293 | 46.4±6.8 |
| | 333 | 50.5±8.3 |

To account for this range of rates we assume the $\pi$ flips of the F7 and F14 rings occur at rates faster than the rotameric exchange motions of the $C_\alpha - C_\beta$ and $C_\beta - C_\gamma$ bonds. We justify this assumption on the grounds that while the $\pi$ flip exchanges the ring between essentially equivalent physical orientations, rotameric exchange moves the entire bulk of the side chain between discrete and distinguishable sites. Fitting the T=293K data for the F7 and F14 $\delta$/ε deuterons to a two site jump model results in a $\pi$ flip of the F7 and F14 rings in the rate range $10^9$-$10^{10}$ $s^{-1}$. The $\pi$ flip rates determined from the $T_1$ measurements were not adjusted further during the line shape simulations.

Given an initial parameter set, the KLDMAS program automatically varied the parameters within the specified ranges, and compared the resulting line shape simulation with data quantitatively by calculating the $\chi^2$ parameter, the sum of squared differences between experimental and simulated side band intensities. The process of searching for parameter sets that minimize the squared difference between the side bands intensities of the experimental and computed $^2$H MAS spectra was automated using a threshold accepting algorithm[27] as described above. Four iterations selected from a 1000 step simulation run for the $^2$H MAS line shape of HAP- bound F7 deuterons are presented as supplementary information. Final parameter sets corresponding to minimized $\chi^2$ are in Tables 5.4 and 5.5.

.

Table 5.4. Exchange rates, quadrupolar coupling constants and asymmetry parameters used to simulate the $^2$H MAS line shapes of the ring deuterons of F7 and F14 in HAP-bound SN-15.

| Parameters for F7 Bound | ζ deuteron | $\delta$/ε deuterons |
|---|---|---|
| QCC(kHz) | 183.0 | 183.0 |
| Asymmetry Parameter | 0.06 | 0.06 |
| Conjoint Flipping Rate Constant ($s^{-1}$) | $5\times10^6$ | $5\times10^6$ |
| Ring Flipping Rate Constant ($s^{-1}$) | None | $5.6\times10^9$ |

| Parameters for F14 Bound | ζ deuteron | $\delta$/ε deuterons |
|---|---|---|
| QCC(kHz) | 182.3 | 182.3 |
| Asymmetry Parameter | 0.06 | 0.06 |
| Conjoint Flipping Rate Constant ($s^{-1}$) | $6\times10^6$ | $6\times10^6$ |
| Ring Flipping Rate constant ($s^{-1}$) | None | $2.6\times10^9$ |

Table 5.4 shows that motions of the F7 and F14 side chains occur at essentially identical rates with the conjoint motions of the $C_\alpha - C_\beta$ and $C_\beta - C_\gamma$bonds occurring at rates of 5-6x$10^6$ $s^{-1}$. These are rates expected to produce the observed partial averaging of the $^2$H MAS line shapes. The difference between the line shapes of F7 and F14 derive from two effects: differences in the structures of the exchanging conformers in F7 versus F14 and differences in the a priori populations, see Table 5.5. For F7, the value of $\chi_1$, $\chi_2$ and the a priori populations corresponding to the best fit to the experimental MAS line shape, lie within a standard deviation of the values listed in the Shapovalov and Dunbrack rotameric library. This means that for F7, which is known to be oriented away from the HAP surface, the side chain conformations are involved in exchange and their a priori populations are typical of phenylalanine side chain conformations

encountered in protein α-helical secondary structures. In contrast, the $\chi_1$ value for conformer 2 in F14 is non-rotameric in the sense that it lies outside the rotameric values associated with $C_\alpha - C_\beta$ bonds in phenylalanine side chain attached to a-helical secondary structures. In addition, the a priori populations of the exchanging conformers in F14 are nearly equal, and lie outside the distributions typical of phenylalanine side chains in a helical secondary structures.

Table 5.5 Rotameric Angles used to simulate the $^2$H MAS line shapes of the ring deuterons of F7 and F14 in HAP-bound SN-15.

| F7 Conformers | $\chi_1$ (Degree) | $\chi_2$ (Degree) | Population(%) |
|---|---|---|---|
| Conformer1 | 186.2 | 88.6 | 76.1 |
| Conformer2 | 274.7 | 54.8 | 23.9 |

| F14 Conformers | $\chi_1$ (Degree) | $\chi_2$ (Degree) | Population(%) |
|---|---|---|---|
| Conformer1 | 93.1 | 208.8 | 40.9 |
| Conformer2 | 273.6 | 56.8 | 58.1 |

## 5.4 Discussion

**Dynamics of the Phenyl Rings.** Compared with unbound sample, the dynamics of the phenyl rings are greatly changed by HAP binding. In unbound protein/peptide, because of the strong hydrophobic environment, the phenyl rings are very rigid and may take the preferential conformation. The hindrance lies in two aspects: first, the interior side chain may sample multiple rotameric states, however, a jump to another rotameric state for a packed side chain can introduce a large strain on the system, which need to move the side chain atoms into volumes occupied by other residues[15]. This rotameric transition has been found for some methyl-bearing side chains, but for aromatic side chains which have relatively bigger size and strong hydrophonic interactions, it is highly unlikely. In the solid state, except some small angle fast liberation motion, the only allowed dynamics is the pi flip at intermediate rate, which involves the rotation around $\chi 2$ axis. The rotameric transition which involves large amplitude motion around $C_\alpha - C_\beta$ axis is never found. Second, for the allowed motion in the unbound protein, only part of the rings can flip, and the flip rate is limited by the hydrophonic environment, e.x, hydrogen bonding, hydration effect, etc, which can cause partial attenuation of the signal. Removal of the limitation can greatly increase the pi flip rate, as reported by Saito and coworkers[95]. In their work, after removing of the hydration water, the flexibility of the phenyl ring is greatly increased.

Although the rotameric transition for phenyl rings is never found in solid state protein/peptide, it was first found in our solid state surface-bound peptide. The previous work has shown that the bound peptide is a monolayer covered on the HAP surface, and the side chain of Phenylalanine is sticking out from the alpha helix of the backbone, instead of in the hydrophobic core. Thus, the freedom of the side chain is greatly increased, which makes the large amplitude motion around $C_\alpha - C_\beta$ axis highly possible. Interestingly, it was also found in some small peptide in solution NMR experiment, as reported by Ernst and coworkers[92]. Although our surface binding sample is purely in solid state, it is interesting to compare our work with theirs. In their solution work, a small peptide, cyclic decapeptide antamanide was used and 4 positions were deuteron labeled−F5, F6, F9, F10. Among these phenylalanine, F5, F9 and F10 only stay in the gauche- rotamer(χ1=300°), while the dynamics of F6 shows many similarities with our bound model: the side chain of F6 is having frequent interconversion between gauche- rotamer(χ1=300°) and trans rotamer(χ1=180°), and rarely visits the gauche+ rotamer(χ1=60°). Besides the rotameric transition, the pi flip around kai2 axis is also at fast limit. The two qualitatively similar works show that the side chain dynamics of surface-adsorbed peptides differ greatly from the dynamics of pure peptides in solid state, but actually resemble to the dynamics of side chains in peptides in solution.

**Surface Interactions.** 13C REDOR measurements have shown that the F7 side chain is further and oriented away from the surface and not involved in any interaction between the peptide and the HAP surface. Therefore, the dynamics of F7 is not affected by the HAP surface. So the site populations and rotameric angles are well adapted to the Shapovalov and Dunbrack rotameric library. While for F14 side chain, its phenyl ring is approximately 4.3-4.8 *Ȧ* away from the HAP surface. The distance is further than what is likely a hydrogen bond between the K6 side chain and a surface phosphate group reported in a prior publication[118], suggesting that the interaction between the F14 side chain and the HAP surface is weaker than hydrogen bonding. So the surface proximity doesn't stop the pi flip, or the rotameric transition around χ1 axis, however, the interaction between the phenyl ring of F14 and the surface has changed the site populations, as well as the rotameric angles, which is no longer in the range of typical rotamer library. The 2 site populations are more even than F7, and the difference between the two rotameric angles are around 180°. These together may have an effect that the ring maximizes the electronic overlapping with the surface, and thus intensifies the surface proximity thanks to the rotameric rotation flexibility[119].

## 5.5 Conclusion

In this manuscript we studied the dynamics of non-polar aromatic side chains within the mineral -recognition domain of the salivary protein statherin, which has been adsorbed onto its native HAP mineral surface. $^2$H NMR MAS spectra and relaxation times of deuterated phenylalanine side chains in both the adsorbed and free HAP recognition peptide domain are compared and interpreted by using $^2$H MAS simulations. In condensed free proteins and in solution, phenylalanine rings are commonly observed to have $\pi$ flip, while rotameric exchange is observed to occur about the $C_\alpha - C_\beta$ bond in phenylalanine side chains for SN-15 molecules adsorbed onto HAP surfaces. This is the first time that big amplitude motion around rotameric axis is seen in solid state, which is very close to the aqueous solution work done by Ernst and coworkers. Moreover, when the dynamics of F7 and F14 are compared, it is found that both rotameric populations and rotameric angles differ as functions of orientation and surface proximity. These results indicate that the side chain dynamics of surface-adsorbed peptides is quite different with the dynamics of the same pure peptides in solid state, but resemble to the dynamics of side chains in small peptides in solution.

# Appendix V Line Shape and Simulations for free and bound Peptide at different Temperatures

## 1. Deuterium MAS Line Shape and Simulations for Unbound SN-15 at Different Temperatures:

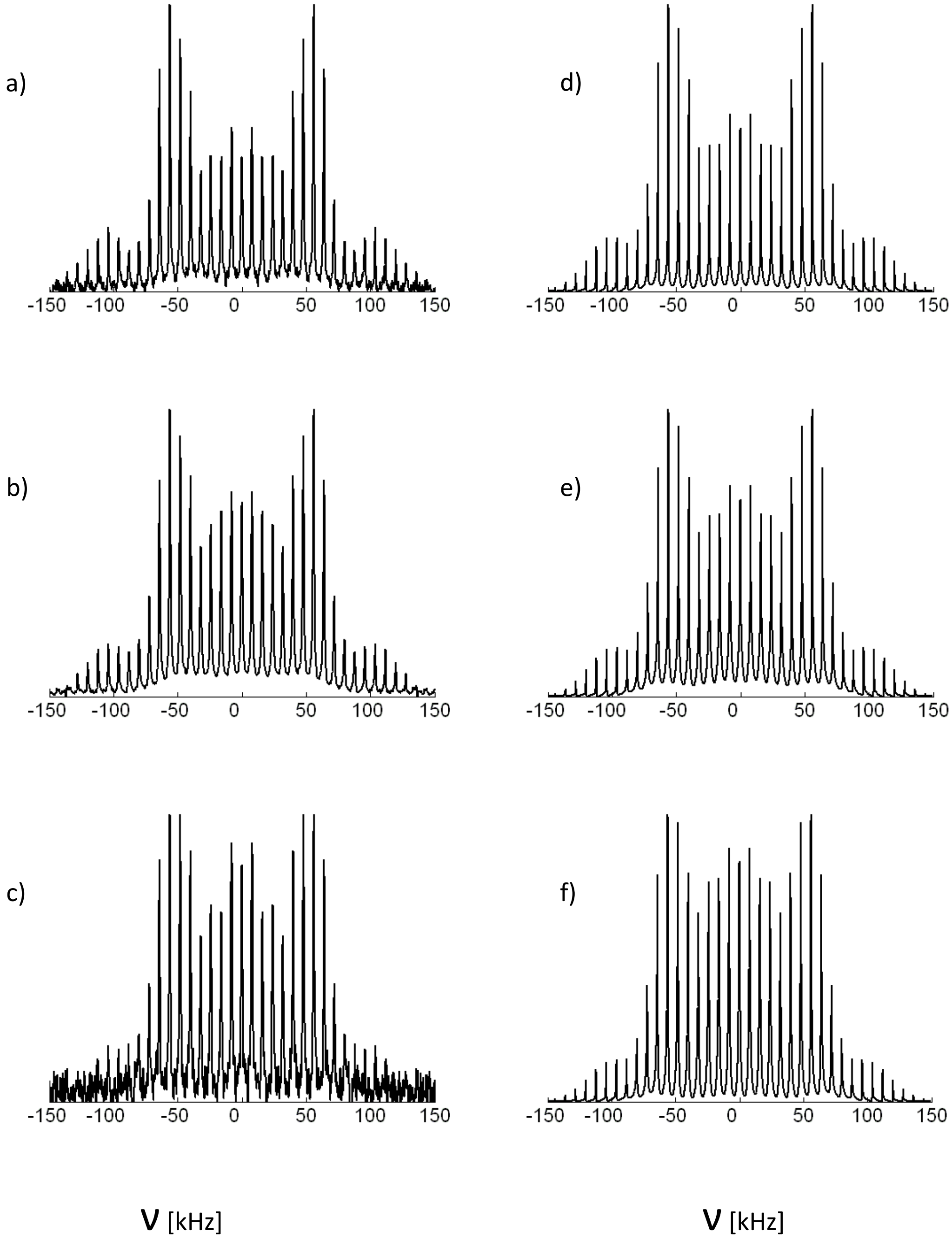

Figure A.V.1 Experimental spectra of F7 in free SN15 peptides at different temperatures vs simulations. (a),(b),(c) are MAS spectra recorded respectively at 243, 293, 333 K. (d), (e), (f) are corresponding simulations.

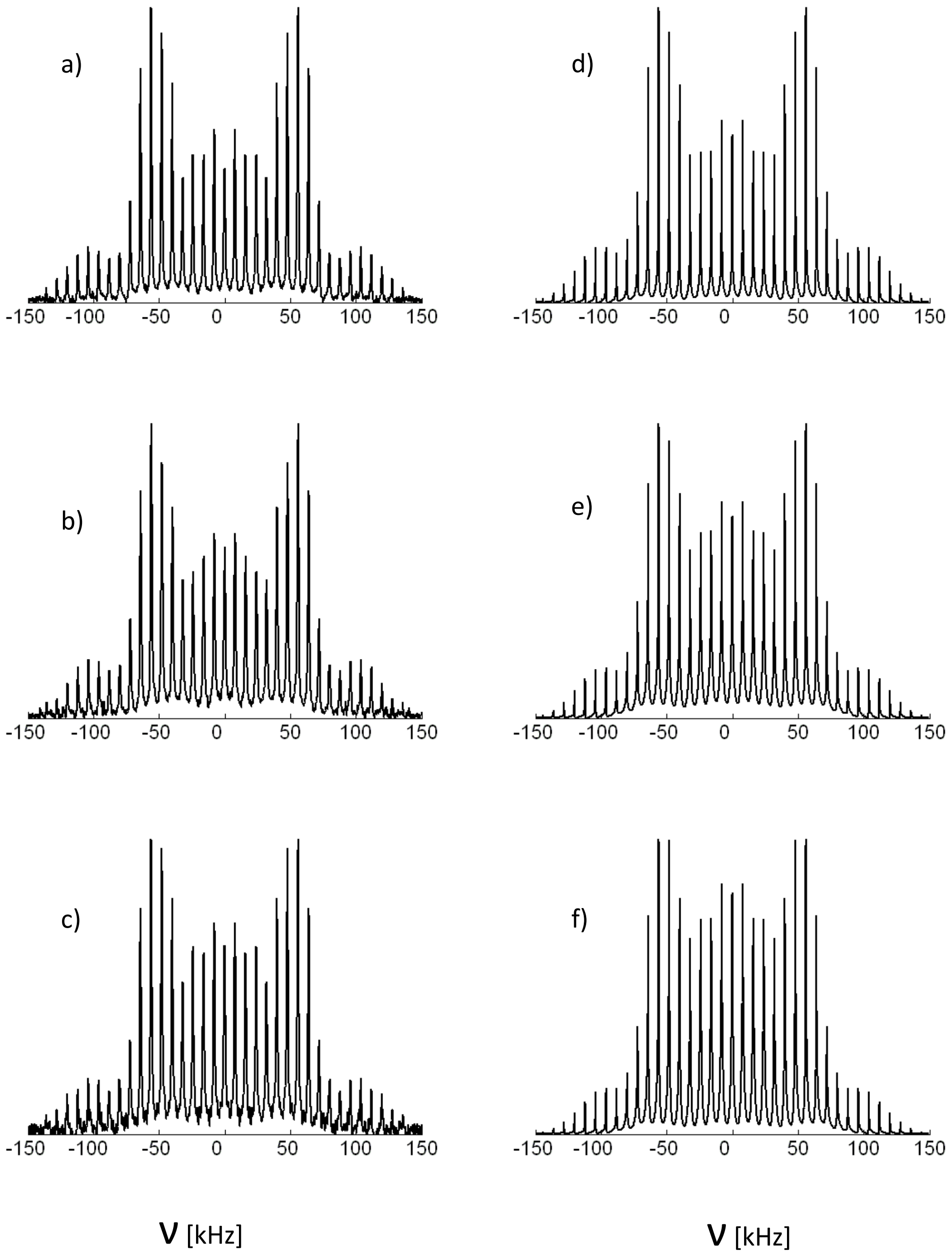

Figure A.V.2. Experimental spectra of F14 in free SN15 peptides at different temperatures vs simulations. (a’),(b’),(c’) are MAS spectra recorded respectively at 243, 293, 333 K. (d’), (e’), (f’) are corresponding simulations.

## 2. Deuterium MAS Line Shape for Bound SN-15 at Different Temperatures:

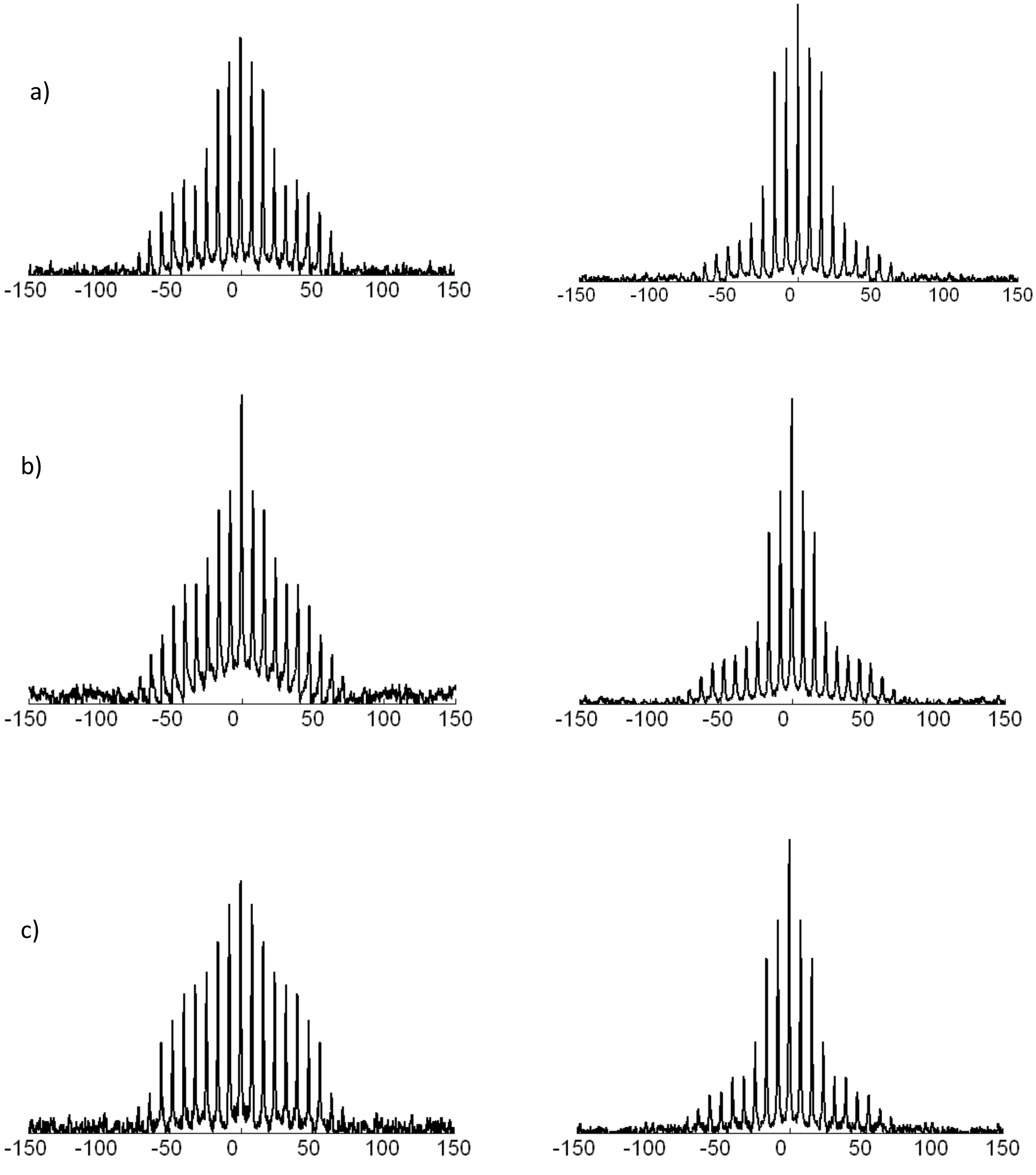

Figure A.V.3 Experimental Spectra of bound F7(left cloumn) and bound F14(right column) at different temperatures. (a),(b), (c) are MAS spectra recorded respectively at 243, 293 and 333 K.

## 3. Iterations selected from a 1000 step simulation run for the $^2$H MAS line shape of HAP- bound F7 deuterons

Using least square method to simulate the intensity of spinning side bands has been employed before[120] , and here we added threshold accepting(TA) method to automate this process. The calculation of least square involves comparison of spinning side bands' intensities between data and simulated line shapes. The number of spinning side bands is predefined before the simulation, and it usually does not contain the center peak to exclude the water peak effect. The variables for a specific model usually are site populations, angles, qcc, rates, etc. They are allowed to change within a predefined range. The idea of TA method runs as follows: before the simulations we set a positive value called threshold, then we first choose an initial variable set and calculate χ^2, and each following step consists of a slight change of the old variable set into a new one and get a new χ^2. The two χ^2 are compared, if new χ^2-old χ^2<threshold, then the new variable set is accepted, otherwise it is rejected. After some simulations, we'll manually decrease the threshold value until it goes to zero. So the only difference of TA method with simulated annealing method is that, instead of using the constant value threshold, the simulated annealing method uses a probability which depends on a time-dependent parameter called temperature. During our simulations, we found that both methods can give satisfactory result but TA method is faster. A specific example of selected steps of simulation process of F7 bound model is given in table 5, and the simulation figure corresponding to table 5 is in Figure 7. There was more than 1000 steps in the whole simulation, and four simulation steps were selected for shown: the initial state was from Dunbrack's rotamer library, in which the single χ2 angle is selected to be the average of the rotamers at a specific χ1 angle, and the least square shows that the initial selection of the variable set is not too far from the data; two other simulation steps b) and c) shows the gradual decrease of the least square and the approach to the experimental data; and d) is the best simulation result we can get.

Table A.V.1 Selected simulation steps which show change of Variable and decrease of least square during the automated simulation process

| Selected Simulation steps | Variables:qcc( kHz) | Primary Conformer Ratio(%) | Primary Conformer Angles: χ1, χ2 | Minor Conformer Angles: χ1, χ2 | Conjoint Flipping Rate Constant | Least Square χ^2 |
|---|---|---|---|---|---|---|
| a) initial | 180.0 | 87.0 | 176.9, 78.7 | 285.9, 74.9 | 10^7 | 0.108 |
| b) | 181.2 | 73.9 | 178.6, 84.0 | 282.7, 43.5 | 5*10^6 | 0.096 |
| c) | 183.8 | 76.3 | 179.2, 88.4 | 272.7, 52.0 | 5*10^6 | 0.030 |
| d) final | 183.0 | 76.1 | 186.2, 88.6 | 274.7, 54.8 | 5*10^6 | 0.019 |

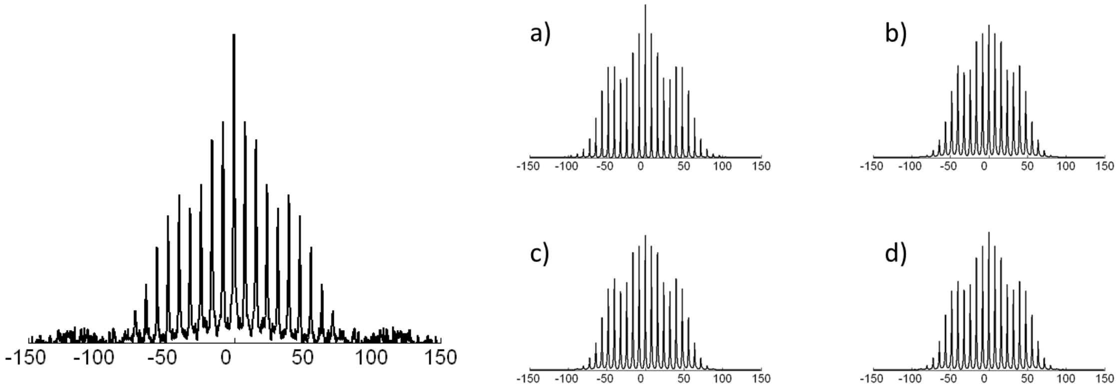

Figure A.V.4 Automated simulation steps.
left: F7 bound data at room temperature; right: F7 simulated line shapes corresponding to Table 5.6

# Bibliography

1. Levitt, M.H. Spin Dynamics: Basics of Nuclear Magnetic Resonance(Wiley, New York, 2007).

2. Slichter, C.P. Principles of Magnetic Resonance(Springer-Verlag Berlin Heidelberg New York, 1978).

3. Duer, M.J. Introduction to Solid-State NMR Spectroscopy(Blackwell Publishing,2004).

4. Abragam, A. the Principles of Nuclear Magnetism(Clarendon Press, Oxford, 1961).

5. G.E.Pake, J.Chem.Phys.16, 327(1948).

6. J.G.Powles, J.H.Strange, Proc.Phys.Soc.82,6(1963).

7. Gurd, F.R.N, Rothgeb, T.M, Adv.Protein Chem. 33, 74-166(1979).

8. Spiess, H.W.Encyclopedia of Nuclear magnetic Resonance(Wiley, Chichester, 1996).

9. Hoatson, G.L.,Tse, T.Y, Vold, R.L. Journal of Magnetic Resonance 98, 342-361(1992).

10. Wittebort, R.J, Olejniczak, E.T, Griffin, R.G, J. Chem. Phys. 86(10),(1987).

11. Kristensen, J.H, Hoatson, G.L, Vold, R.L, Solid State Nuclear magnetic Resonance 13, 1-37(1998).

12. Heaton, N.J, Molecular physics, 92(2), 251-263(1997).

13. Vold, R.R, Vold, R.L, Journal of Chemical Physics 88, 1443-1457(1988).

14. Greenfield, M.S, Ronemus, A.D, Vold, R.L, Vold, R.R, Journal of Magnetic Resonance 72, 89-107(1987).

15. Spiess, H.W, Sillescu, H.J, Journal of Magnetic Resonance 42, 381-389(1981).

16. Lin, T.H, Vold, R.R, Vold, r.L. Journal of Magnetic Resonance 95, 71-79(1991).

17. Allerhand, A, Gutowsky, H.S, J.Chem.Phys.42, 4203(1965).

18. Gutowsky, H.S, Vold, R.L, Wells, E.J, J.Chem. Phys. 43, 4107(1965).

19. Sharon E.A, Sasa,A, Andrew, J.B, Stephen, W, Chemical Physics Letters 364,634-642(2002).

20. Magnus, W, Winkler, S. Floquet's Theorem. In *Hill's Equation*; Dover: New York(1979); pp 3-8.

21. Weintraub, O.; Vega, S. Journal of Magnetic Resonance, Series A, *105*, 245-267(1993).

22. Vold, R. L, Hoatson, G. L. Journal of Magnetic Resonance, *198*, 57-72(2009).

23. Duer, M. J, Levitt, M. H. Solid State Nuclear Magnetic Resonance, 1, 211-215(1992).

24. Torchia, D. A, Szabo, A. Journal of magnetic Resonance, *49*, 107-121(1982).

25. Zaremba, S.K, Ann.mate.Pure Appl. 73, 293(1966).

26. Cheng, V.B, Suzukawa, H.H, Wolfsberg, M, J. Chem.Phys. 59, 3992(1973).

27. Dueck, G, Scheuer, T, Journal of Computational Physics 90,161-175(1990)).

28. Vold, R.L, Hoatson, G.L, Vugmeyster, L, Ostrovsky, D, Castro, P.J.D, Physical Chemistry Chemical Physics, 11, 7008-7012(2009).

29. Healy, K.E, Curr.Opin. Solid State & Mat. Sci. 4, 381-387(1999).

30. Angelova, N, hunkeler, D, Trends Biotech. 17, 409-421(1999).

31. Langer, R, Acc. Chem. Res. 33, 94-101(2000).

32. Ratner, B.D, Bryant, S.J, Annu. Rev. Biomed. Eng, 6, 41-75(2004).

33. Vasita, R, Shanmugam, K, Katti, D.S, Curr. Top. Med. Chem, 8, 341-353(2008).

34. Borkenhagen, M, Clemence, J.F, Sigrist, H, Aebischer, P.J, Biomed Mat. Res. 40, 392-400(1998).

35 Rezania, A, Healy, K.E, Biotech Progress, 15, 19-32(1999).

36 Gilbert, M, Shaw, W.J, Long, J.R, Nelson, K, Drobny, G.P, Giachelli, C.M, Stayton, P.S, J.Biol.Chem, 275, 16213-16218(2000).

37. Venugonal, J, Low, S, Choon, A.T, Ramakrishna, S, J.Biomed.Mater.Res.84B, 34-48(2008).

38. Drumheller, P.D, Elbert, D.L, Hubbell, J,A, Biotech and Bioeng, 43, 772-780(1994).

39. Neff, j.A, Caldwell, K.D, Tresco, P.A, J.Biomed. Mater. Res, 40,511(1998).

40. Tong, Y.W, Shoichet, M.S, J.Biomater. Sci. Polymer Ed, 9,713(1998).

41. Ostuni, E, Grzybowski, b.A, Mrksich, M, Roberts, C.S, Whitesides, G.M, Langmuir, 19, 1861(2003).

42. Palmer, A.G, III, Williams, j, McDermott, A, J.Phys.Chem, 100, 13293(1996).

43. Gardner, K.H, Kay, L.E, Annu. Rev. Biophys. Biomol. Struct, 27, 357(1998).

44. Bechinger, B, Kinder, R, Helmle, M, Vogt, T.C.B, Harzer, U, Schinzel, S, Biopolymers, 51,174(1999).

45. Degrado, W.F, Lear, J.D, J.Am.Chem.Soc, 107, 7684(1985).

46. Long, J.R, Oyler, N, Drobny, G.R, Stayton, P.S, J.Am.Chem.soc, 124, 6297(2002).

47. Mermut, O, Phillips, D.C, York, R.L, McCrea, K.R, Ward, R.S, Somorjai, G,G, J. Am. Chem. Soc, 128, 3598(2006).

48. Phillips, D.C, York, R.L, Mermut, O, McCrea, K.R, Ward, R.S, Somorjai, G.A, J. Phys. Chem. C, 111, 255(2007).

49. Batchelder, L.S, Sullivan, C.E, Jelinski, L.W, Torchia, D. A, Proc. Natl. Acad. Sci. U.S.A, 79, 386(1982).

50. Benedetti, C, In Proceedings of the Fifth American Peptides Symposium, Goodman, M, Meienhofer, J, Eds, Wiley: New York, pp 257-274(1977).

51. Janin, j, Wodak, S, Levitt, m, Maigret, B, J. Mol. Biol, 125,357(1978).

52. Chi, S.C, Coi, S.C, Langmuir, 21, 11765(2005).

53. Du, Q, Freysz, E, Shen, Y.R, Phys.Rev.Lett, 72,238(1994).

54. Watry, M.R, Richmond, G.L, J. Phys. Chem. B, 106, 12517(2002).

55. Ward, R.N, Davies, P.B, Bain, C.D, J. Phys. Chem, 97, 7141(1993).

56. Jelinski, L. W, Torchia, D.A, J. Mol. Biol, 138,255(1980).

57. Jelinski, l. W, Sullivan, C.E, Torchia, D.A, Nature, 284, 531(1980).

58. Jelinski, L.W, Sullivan, C.E, Batchelder, l.S, Torchia, D.A, Biophys. J, 10, 515(1980).

59. Barnes, R. G. Deuteron quadrupole coupling tensors in solids. In *Advances in Nuclear Quadrupole Resonance*; Smith, J. A. S., Ed.; Heyden: London, Vol. 1; pp 335-355(1974).

60. Auger, M.; Smith, I. C.; Jarrell, H. C. *Biophys. J. 59*, 31-38(1991).

61. Lorieau, J. L.; McDermott, A. E. *J. Am. Chem. Soc.*, *128*, 11505-11512(2006).

62. Hansen, A. L.; Al-Hashimi, H. M. *J. Am. Chem. Soc.*,*129*, 16072-16082(2007).

63. Zhang, Q.; Stelzer, A. C.; Fisher, C. K.; Al-Hashimi, H. M. *Nature*, *450*, 1263-1267(2007).

64. Olsen, G. L.; Echodu, D. C.; Shajani, Z.; Bardaro, M. F.; Varani, G.; Drobny, G. P. *J. Am. Chem. Soc.* ,*130*, 2896-2897(2008).

65. Tiburu, E. K.; Karp, E. S.; Dave, P. C.; Damodaran, K.; Lorigan, G. A. *Biochemistry*, *43*, 13899-13909(2004).

66. Breen, N. F.; Weidner, T.; Li, K.; Castner, D. G.; Drobny, G. P. *J. Am. Chem. Soc.*, *131*, 14148-14149(2009).

67. Glaubitz, C.; Burnett, I. J.; Gröbner, G.; Mason, A. J.; Watts, A. *J. Am. Chem. Soc.*, *121*, 5787-5794(1999).

68. Lee, H.; Ortiz de Montellano, P. R.; McDermott, A. E. *Biochemistry*, *38*, 10808-10813(1999).

69. Agarwal, V.; Faelber, K.; Schmieder, P.; Reif, B. *J. Am. Chem. Soc.* , *131*, 2-3(2008).

70. Weidner, T.; Breen, N. F.; Li, K.; Drobny, G. P.; Castner, D. G. *Proc. Natl. Acad. Sci.*, *107*, 13288-13293(2010).

71. Atherton, E.; Sheppard, R. C. *Solid phase peptide synthesis: a practical approach*; Oxford University Press: Oxford(1989).

72. Davis, J. H. *Biophys. J.* , *27*, 339-358(1979).

73. Hologne, M.; Faelber, K.; Diehl, A.; Reif, B. *J. Am. Chem. Soc.*, *127*,11208-11209(2005).

74. Hologne, M.; Chen, Z. J.; Reif, B. *J. Magn. Reson.*, *179*, 20-28(2006).

75. Abu-Baker, S.; Lu, J. X.; Chu, S. D.; Brinn, C. C.; Makaroff, C. A.; Lorigan, G. A. *Biochemistry*, *46*, 11695-11706(2007).

76. Weidner, T.; Apte, J. S.; Gamble, L. J.; Castner, D. G. *Langmuir*, *26*, 3433-3440(2010).

77. Gath, J.; Hoaston, G. L.; Vold, R. L.; Berthoud, R.; Coperet, C.; Grellier, M.; Sabo-Etienne, S.; Lesage, A.; Emsley, L. *Phys. Chem. Chem. Phys. 11*, 6962-6971(2009).

78. Ying, W. W.; Irvine, S. E.; Beekman, R. A.; Siminovitch, D. J.; Smith, S. O. *J. Am. Chem. Soc.*, *122*, 11125-11128(2000).

79. Chu, S.; Coey, A. T.; Lorigan, G. A. *Biochimica et Biophysica Acta (BBA) - Biomembranes*, *1798*, 210-215(2010).

80. Long, J. R.; Mills, F. D.; Ganesh, O. K.; Antharam, V. C.; Farver, R. S. *Biochim. Biophys. Acta, Biomembr, 1798*, 216-222(2010).

81. Debrunner, P.G; Frauenfelder, H. Annu. Rev. Phys. Chem, 33, 283(1982).

82. janin, J; Wodak, S.J, Prog. Biophys. Mol. Biol, 42, 21(1983).

83. Ringe, D.; Petsko, G. Prog. Biophys. Mol. Biol, 45, 197(1985).

84. Frauenfelder,H., Sligar, S.G.&Wolynes, P. G, Science, 254, 1598–1603 (1991).

85. Rasmussen, B. F., Stock, A. M., Ringe, D. & Petsko, G. A, Nature 357, 423–424 (1992).

86. Karplus, M, McCammon, J. A, Nature Struct. Biol. 9, 646–652 (2002).

87. Eisenmesser, E. Z., Bosco, D. A., Akke, M, Kern, D, Science 295, 1520–1523 (2002).

88. Wong, C. F, McCammon, J. A, Annu. Rev. Pharmacol. Toxicol. 43, 31–45 (2003).

89. Hu, H, Hermans, J, Lee, A. L, Journal of Biomolecular NMR32, 151-162(2005).

90. Dunbrack, R. L, Karplus, M, J. Mol. Biol, 230, 543-574(1993).

91. Shapovalov, M. V, Dunbrack, R.L, Structure 19,844-858(2011).

92. Bremi, T, Bruschweiler, R, Ernst, R. R, J. Am. Chem. Soc, 119, 4272-4284(1997).

93. Zeeb, M, Balbach, J, J. Am. Chem. Soc, 127(38), 13207-13212(2005).

94. Lange, O. F, Lakomek, N. A, Fares, C, Schroder, G. F, Walter, K. F. A, Science, 320(5882), 1471-1475(2008).

95. Naito, A, Iizuka, T, Tuzi, S, Price, W.S, Hayamizu, k, Saito, H, Journal of Molecular Structure, 355, 55-60(1995).

96. Smith, R. L, Oldfield, E, Science, 225, 4659, 280-288(1984).

97. Allerhand, A, Gutowsky, H.S, J.Chem.Phys. 42, 4203(1965) .

98. Nicholas, F. B, Li, K, Olsen, G. L, Drobny, G. P, J. Phys. Chem. B, 115(30), 9452-9460(2011).

99. Schlesinger, D. H, Hay, D. I, J. Biol. Chem, 252, 1689-1695(1977).

100. Amano, A, Kataoka, K, Raj, P. A, genco, R. J, Shizukuishi, S, Infect. Immun, 64, 4249-4254(1996).

101. Ramasubbu, N, Thomas, l. M, Bhandary, K. K, Levine, M. J, Crit. Rev. Oral Biol. Med, 4, 363-370(1993).

102. Shaw, W. J, Long, J. R, Campbell, A. A, Stayton, P. S, Drobny, G. P, J. Am. Chem. Soc, 122, 7118-7119(2000).

103. Raj, P. A, Johnsson, M, Levine, M. J, Nancollas, G. H, J. Biol. Chem, 267, 5968(1992).

104. Gururaja, T. L, Levine, M. J, Pept. Res, 9, 283-289(1996).

105. Gibson, J. M, Popham, J. M, Raghunathan, V, Stayton, P. S, Drobny, G. P, J. Am. Chem. Soc, 128, 5364-5370(2006).

106. Shaw, W. J, Long, J. R, Dindot, J. L, Campbell, A. A, Stayton, P. S, Drobny, G. P, J. Am. Chem. Soc, 122, 1709-1716(2000).

107. Goobes, G, Goobes, R, Shaw, W. J, Gibson, j. M, Long, J. R, Raghunathan, V, Furman, O. S, Popham, J. M, Baker, D, Campbell, C. T, Stayton, P, S, Drobny, G. P, Magn. Reson. Chem, 45, S32-S47(2007).

108. Makrodimitris, K, Masica, D. L, Kim, E. T, Gray, J. J, J. Am. Chem. Soc, 129, 13713-13722(2007).

109. Kates, S, Albericio, F, Solid Phase Synthesis: A Practical Guide; Marcel Dekker: New York(2000).

110. Breen, N. F, Li, k, Olsen, G. L, Drobny, G. P, J. Phys. Chem. B, 115, 9452-9460(2011).

111. Dueck, G, Scheuer, T, Journal of Computational Physics, 90, 161-175(1990).

112. Gall, C. M, Cross, T. A, Diverdi, J. A, Opella, S. J, Proc. Natl. Acad. Sci. USA, 79, 101-105(1982).

113. Kinsey, R. A, Kintanar, A, Oldfield, E, The Journal of Biological Chemistry, 256, 17, 9028-9036(1981).

114. Hiraoki, T, Kogame, A, Nishi, N, Tsutsumi, A, Journal of Molecular Structure 441, 243-250(1998).

115. Huang, Y, Dissertation(2007).

116. Ashbrook, S. E, Antonijevic, S, Berry, A. J, Wimperis, S, Chemical Physics Letters, 364, 634-642(2002).

117. Ponder, J. W, Richards, F.M, J. molec. Biol. 193, 775-792(1987).

118. Gibson, J. M, Raghunathan, V, Popham, J. M, Stayton, P. S, Drobny, G. P, J. Am. Chem. Soc, 127, 9350-9351(2005).

119. Ghiringhelli, L. M, Site, L. D, J. Am. Chem. Soc, 130, 2634-2638(2008).

120. Kristensen, J, Bildsoe,H, Jakobsen, H, Nielsen, N, Journal of Magnetic Resonance 100, 437-443(1992).

# VITA

Kun Li

The author was born in Shandong, China on 10/07/1979. In 2003, he finished his undergraduate study with a Bachelor of Science degree in University of Science & Technology of China. In fall 2004, he was admitted to begin his graduate study in Department of Physics in University of Washington. After working as Teaching Assistant for the first two years and got Master degree in Physics in 2006, the author joined Professor Gary Drobny's research group. After 6 years' research in Solid State NMR, he finished his Doctorate in 2012.